DUAL-MODAL AND DUAL-SENSING-MECHANISM (DMDSM) ACOUSTIC

SENSORS FOR ROBOTIC RANGING AND MATERIAL DIFFERENTIATION

A Dissertation

by

CHENG FANG

Submitted to the Office of Graduate and Professional Studies of
Texas A&M University
in partial fulfillment of the requirements for the degree of

DOCTOR OF PHILOSOPHY

Chair of Committee,	Jun Zou
Committee Members,	Pao Tai Lin
	Raffaella Righetti
	Dezhen Song
Head of Department,	Costas Georghiades

May 2023

Major Subject: Electrical Engineering

ABSTRACT

One of the grand challenges in robotics is robust grasping of unknown objects. This is particularly important when robots expand its territory from industry floors to domestic service applications where the object prior knowledge is not often available. As a result, sensor-based grasping is more desirable. Ideally, with the assistance of object sensing, robotic fingers can respond to subtle changes in object pose right before grasping and adjust operations dynamically. Moreover, the object material and structure information can help planners better estimate the force distribution, impact characteristics and friction coefficients for a more robust grasping.

However, current sensors have difficulties in satisfying these requirements. Tactile/force sensors may change object poses or even damage the object, which leads to slow or failed grasping. Non-contact long-distance sensors such as camera, LIDAR, radar, sonar suffer from occlusion or blind zones. Therefore, non-contact near-distance sensing is the optimal solution. Unfortunately, existing near-distance sensors based on optical, electric-field, and acoustic signals still cannot satisfy these grasping requirements. Electric-field sensors have difficulties in targets with low dielectric contrast to air. The optical ones lack lateral resolution and are not effective for optically-transparent or highly-reflective targets. Acoustic-based sensors could work on distance ranging and material/structure sensing, but fail on thin-film, porous, or sound-absorbing targets.

To address these issues, a new finger-mounted non-contact dual-modal and dual-sensing-mechanism (DMDSM) sensor for near-distance ranging and material/structure differentiation is studied and developed, which is based on two modalities and sensing mechanisms: pulse-echo ultrasound (US) and optoacoustics (OA). In both modalities, the object distance is estimated from the Time-of-Flight (ToF) of the US/OA signal, whose frequency spectra are used to extract the distinctive features of the material/structure. The development of the DMDSM sensor is conducted as follows. First, the prototype of the DMDSM sensor is designed, fabricated, and characterized. Testing is conducted on conventional objects and optically and/or acoustically challenging targets (OACTs) to characterize its performance. Second, to simplify the DMDSM sensor design and operation, a single wideband ultrasound transmitter and receiver is investigated where both US and OA collection can be initiated by a single laser pulse. Third, to expand to areal mapping or imaging, a new self-focused US/OA transceiver and a flat scanning mirror are studied to steer laser and ultrasound beams over the target with customized patterns. At last, optically-transparent focused (OTF) ultrasound transducers are explored, which are helpful to miniaturize the DMDSM sensors while enhancing their performances.

DEDICATION

To my parents

Mr. Ming Fang

Mrs. Pingying Lyu

ACKNOWLEDGEMENTS

CONTRIBUTORS AND FUNDING SOURCES

Contributors

This work was supported by a thesis (or) dissertation committee consisting of Professor Jun Zou, Pao Tai Lin and Raffaella Righetti of the Department of Electrical & Computer Engineering and Professor Dezhen Song of the Department of Computer Science & Engineering.

The data analyzed for Chapter 4.6 was conducted by Fengzhi Guo and Di Wang, two students of Professor Dezhen Song, and were published in 2022 in an article listed in the 2022 IEEE 18th International Conference on Automation Science and Engineering (CASE).

All other work conducted for the thesis (or) dissertation was completed by the student independently.

Funding Sources

TABLE OF CONTENTS

LIST OF FIGURES

xiv

LIST OF TABLES

xviii

1. INTRODUCTION

1.1 Robotic Grasping

Robotic grasping dictates how a robot can interact with physical objects and inherently determines the tasks that the robot can perform. Actually, achieving reliable grasping of unknown objects has been a grand challenge for robotics researchers [1] [2]. This is particularly important when robots expand their territory from industry floors to a wide range of domestic service applications where the prior knowledge of targeted objects is often not available. Sensor-less grasping has been well studied [3] [4]. However, it suffers from efficiency issues. Therefore, sensor-based approaches still dominate grasping operations.

A good sensor should be able to detect object relative pose at near distance and recognize its material-type/structure information, which are important for a successful grasping. Ideally, with the assistance of near-distance (e.g. < 0.5 cm) ranging, robotic fingers can respond to subtle changes in object pose right before the planned contact and adjust grasping operations dynamically. Moreover, the object material-type and internal-structure information can help planners better estimate the force distribution, impact characteristics and friction coefficients for a more robust grasping.

1.2 Existing Sensors for Robotic Grasping

Unfortunately, current sensors have difficulties in satisfying all these requirements despite significant progress has been made in recent development. Tactile

[5] [6] and force sensing [7] are the primary approaches, which intrinsically stimulate the perception of human hands. However, these contact sensing approaches require the robotic finger to touch the object for sensing which may change object poses or even damage the object surface, leading to either slow grasping process or complete failure in grasping. Therefore, non-contact sensing is more desirable.

Non-contact long-distance sensors, such as cameras, LIDAR (Light Detection and Ranging), radar, and sonar, have been developed extensively in recent years. Cameras can observe the physical object at a distance but cannot obtain precise relative pose due to the occlusion caused by closing-in fingers themselves [8]. LIDAR has been successfully applied for robotic mapping and navigation [9] [10], which can achieve millimeter-level resolution [11]. However, LIDAR measures distance using time-of-flight and thus has a blind zone when the perceived object is relatively close. Similar as LIDAR, radar and sonar are mainly applied for long-distance detection [12], which also have a blind zone for near-distance ranging. As a result, non-contact near-distance sensors are the optimal solution for perceiving unknown objects for robotic grasping.

Recent development of near-distance (proximity or pretouch) sensors based on optical, electric-field, and acoustic signals have achieved great progress. However, they still cannot satisfy the grasping requirements. Electric-field sensors have limited lateral resolution and difficulties in detecting targets whose dielectric constants are close to that of air, such as fabrics, thin plastics, and thin sheets of paper [13] [14] [15] [16]. The optical sensors lack the lateral resolution and have difficulties in detecting highly-effective or optically-transparent targets [17] [18] [19] [20]. Existing acoustic-based

2

sensors, including seashell effect ones, could primarily work on object distance ranging and material/structure sensing, but have limited lateral resolutions due to the widespread signal dispersion pattern, and fail on perceiving certain types of materials, such as thin-film, porous, or sound absorbing targets [21] [22] [23] [24].

More backgrounds of these existing sensors are reviewed in Chapter 2.

1.3 Dual-Modal and Dual-Sensing-Mechanism (DMDSM) Sensors

To address the remaining issues of existing sensors, we have developed a finger-mounted non-contact near-distance sensor [25] for distance ranging and material/structure differentiation based on two different modalities and sensing mechanisms: pulse-echo ultrasound (US) and optoacoustics (OA) [26] [27]. We name this as a dual-modal and dual-sensing-mechanism (DMDSM) design. Dual modal means US and OA modalities, and dual sensing refers to distance ranging and material/structure sensing. The US utilizes a transducer to transmit ultrasound to the target and then detect the reflected echo to extract the target information. OA illuminates a laser pulse onto the target and the optoacoustic signals directly induced from the target is received by the transducer for target identification. In both modalities, the object distance is estimated based on the Time-of-Flights (ToFs) of the US/OA signals, whose frequency spectra are used to extract the distinctive features about the target materials and structure. A prototype of the new DMDSM sensor is fabricated and characterized. Sensing experiments are conducted on conventional objects as well as optically and/or acoustically challenging targets (OACTs) to characterize its differentiation capability.

The overall 100% accuracy indicates the initial success of our sensor design. The development of the DMDSM sensor will be discussed in Chapter 3.

Although the primary DMDSM sensor works well as a prototype in the initial demonstration, it has a relatively complex configuration, which limits its sensing applications. To address this issue, the second-generation (G2) DMDSM sensor [28] is designed by utilizing a wideband single ultrasound transmitter and receiver for object ranging and material/structure sensing where both US and OA signals collection is triggered by the same laser pulse. A prototype of the G2 DMDSM sensor has been fabricated and characterized, and an object scanning system [29] with the G2 sensor has been built to conduct scanning experiments on common household objects with different shapes and materials. Experimental results show that the G2 DMDSM sensor can achieve satisfying ranging and material/structure sensing capabilities, with simpler construction and operation. The G2 DMDSM sensor will be discussed in Chapter 4.

Although the G2 DMDSM sensor provides a simple and effective configuration, it is limited to single-point detection by the bulky parabolic mirror. This makes it difficult to steer laser and ultrasound beams over the target surface, which otherwise would be very useful for fast mapping or imaging the detailed features for facilitating the grasping. To address this issue, the third-generation (G3) DMDSM sensor has been developed with a self-focused wideband US/OA transceiver and a flat 2D scanning mirror so that the bulky parabolic mirror is not necessary. As a result, the self-focused laser and ultrasound beams can be easily steered by the flat scanning mirror, which expands the single-point detection into (fast) areal mapping or imaging. A prototype of

4

the G3 DMDSM sensor is fabricated and characterized. Together with the scanning mirror, thin wire targets made of the same or different materials are scanned and imaged. The experimental results show that the G3 DMDSM sensor can integrate with a 2D flat scanning mirror for fast areal mapping and imaging to better facilitate the object grasping. The G3 DMDSM sensor will be discussed in Chapter 5.

Although the ring-shaped focused PZT transducer works well in the G3 DMDSM sensor as the initial demonstration, it is difficult to be miniaturized while maintaining the detection sensitivity, which is due to relatively complex structure, large dimension, and low acoustic reception efficiency. To address this issue, new optically-transparent focused (OTF) ultrasound transducers made of PVDF (polyvinylidene fluoride) [30] [31] and its co-polymer materials [32] are investigated, which could be helpful to further miniaturize the DMDSM sensor design. Two OTF transducers will be discussed in Chapter 6.

The conclusions and future work will be summarized in Chapter 7.

2. BACKGROUND AND MOTIVATION

2.1 Robotic Grasping*[1]

Robotic grasping dictates how a robot can interact with physical objects and inherently determines the tasks that the robot can perform (Fig. 2.1(a)). Reliable grasping of unknown objects has been a grand challenge for robotics researchers [1] [2] (Fig. 2.1(b)). This is particularly important when a robot expands its territory from industry floors to a wide range of domestic applications where prior knowledge of the object is not often available. To know the object's distance, shape, material, and even subsurface structures, a variety of sensors have been developed to assist robotic grasping.

(a)   (b)

Fig. 2. 1. (a) A representative robot platform. (b) Robotic grasping execution of representative household objects. Reprinted with permission from [2] © Springer Nature.

2.2 Sensorless Grasping*[2]

Sensor-less grasping exists but suffers from efficiency issues [3] [4], because without the aid of sensing, objects grasping has to rely on the motion strategies of the gripper and repetitive contacts with the objects to reduce the object's pose uncertainty.

Sensor-less grasping is popular in manufacturing, such as injection molding and stamping which often produce a stream of parts that must be reoriented before assembly. The parts feeder (Fig. 2.2(a)) is a mechanical gripper to orient the parts, whose manipulation algorithm can be reprogrammable to adapt to the different geometry of parts. As Fig. 2.2(b), take the ubiquitous parallel-jaw gripper and simple rectangular part as an example. As illustrated in Fig. 2.2(c), the alignment between the rectangular part's major axis and the gripper is ensured by a sequence of two squeeze actions. The grasping and manipulation onto a more complex part is illustrated in Fig. 2.2(d). As a conclusion, sensor-based grasping is more practical to perceive the household objects with different materials and shapes.

(a)

(b)   (c)   (d)
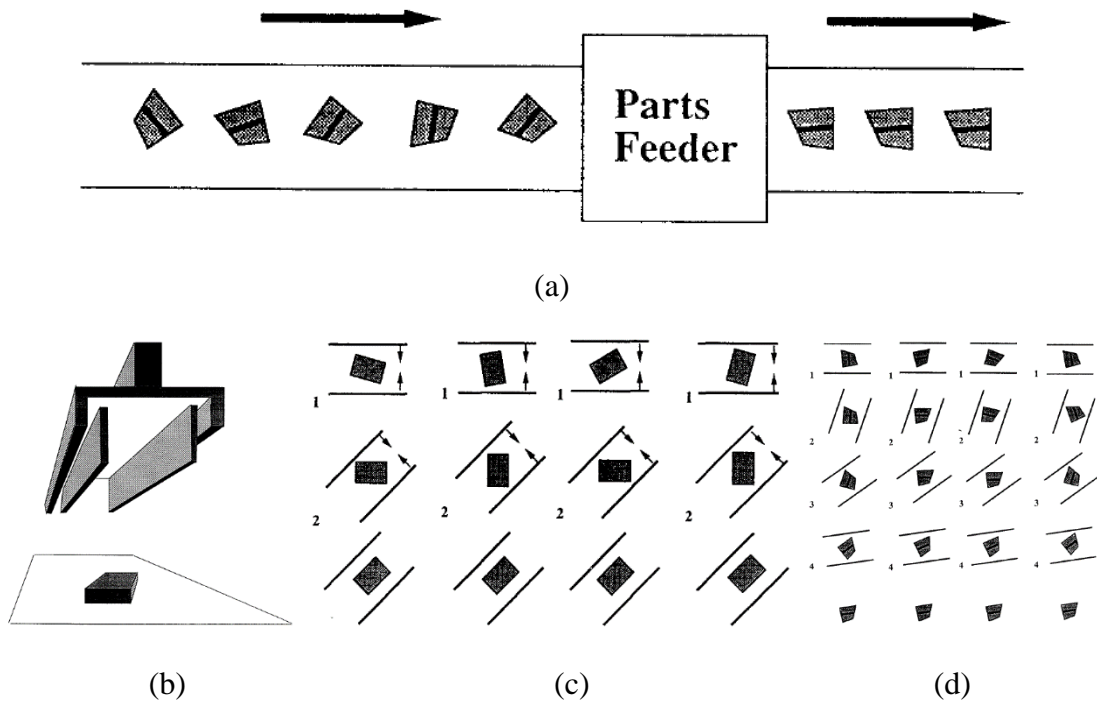
Fig. 2. 2. (a) The parts feeder is a machine that orients the coming parts. (b) A parallel-jaw gripper poised above a rectangular part. (c) Four traces, running from top to bottom,

of a two-stage plan for orienting a rectangular part. (d) Four traces of the resulting squeeze plan for the 4-gon. Reprinted with permission from [3] © Springer Nature.

2.3 Tactile / Force Sensors*3

Sensor-less grasping is based on the real contact between the object and gripper, which intrinsically provides the idea of contact sensors. The perception of existing tactile/force sensors is achieved by directly touching the objects, which has been employed as the initial grasping and manipulating strategy by balancing the contact forces around the object [20]. Unfortunately, tactile/force sensors need actual touch with the object to perceive its information, which may shift the object location. Therefore, with contact sensors, robotic fingers are limited to minor adjustments of contact forces or iterative re-grasping of the object for successful grasping, which could be time-consuming, frequently knocks the objects for repeated grasping attempts [17], and even damages the object surface. The diagram and photo of the representative tactile/forces sensors mounted on robotic fingertips are shown as Fig. 2.3.
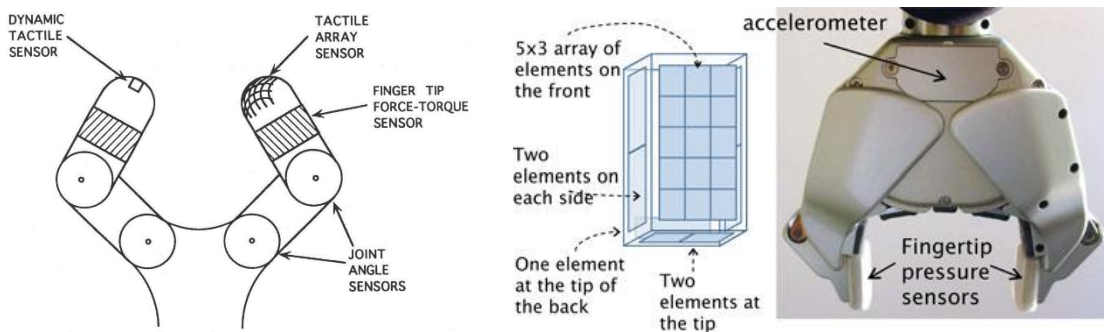
*3Reprinted with permission from "Tactile sensing and control of robotic manipulation" by Howe, Robert D., 1993. *Advanced Robotics*, 8(3), 245-261, Copyright 1993 by Taylor & Francis.

Fig. 2. 3. (a) Schematic drawing of a robot hand equipped with several types of contact sensor. Reprinted with permission from [33] © Taylor & Francis. (b) Photo of a robot gripper with an accelerometer mounted in the palm, and pressure sensors attached to the fingertips. Reprinted with permission from [34] © IEEE.

2.4 Long-Distance Sensors*4

Since the contact sensors are not optimal for robotic grasping, the non-contact sensors have attracted great interests. Conventional non-contact sensors are actually long-distance sensors, including cameras, LIDAR, radar, and sonar. As the most popular one, cameras have been widely used to interrogate the object information, including distance, shape, materials, and even subsurface structures when the object is at a relatively long distance. LIDAR, radar, and sonar are more widely applied as key sensing components to map the unknown surrounding environments for autonomous navigations of the robot. Although these long-distance sensors have led to many successful robot systems, they are not optimal to be applied for robotic grasping, due to the occlusion caused by the closing-in robotic fingers themselves [8] or having a blind zone [9] [35] [36] [12] when the perceived object is relatively close. Because of the induced errors and uncertainties, the reliability of robotic grasping based on the long-distance sensors is limited [17]. The non-contact long-distance sensors are discussed as follows.

*3Reprinted with permission from "Human-inspired robotic grasp control with tactile sensing" by Romano, Joseph M., Hsiao, Kaijen, Niemeyer, Gunter, Chitta, Sachin, Kuchenbecker, J. Katherine, 2011. *IEEE Transactions on Robotics*, 27(6), 1067-1079, Copyright 2011 by IEEE.

Camera-assisted grasping has achieved a great progress in robotics, because the camera has equiped the robot with human-like eyes to visualize the object distance, shape, material and even sub-surface structures. This is very helpful for the robot to arrange the plan for a robust grasping when the object is at a distance without being blocked by the robotic fingers. Moreover, with the developed visual-servo controller, the robot can better navigate to identify the targeted object using computer vision, and then plan the fingers to grasp the object. Visual servoing is normally achieved by position-based visual servoing (PBVS) and image-based visual servoing (IBVS). A representative robotic arm with dual cameras to assist the object sensing and grasping is shown as Fig. 2.4 [37]. Since the stereo camera suffers from the occlusion caused by the closing-in robotic fingers themselves, a second web cam has to be added to monitor the object right above the two-finger grippers. However, for a gripper with three fingers or more, the sight of the web cam would be still blocked by the robotic fingers.
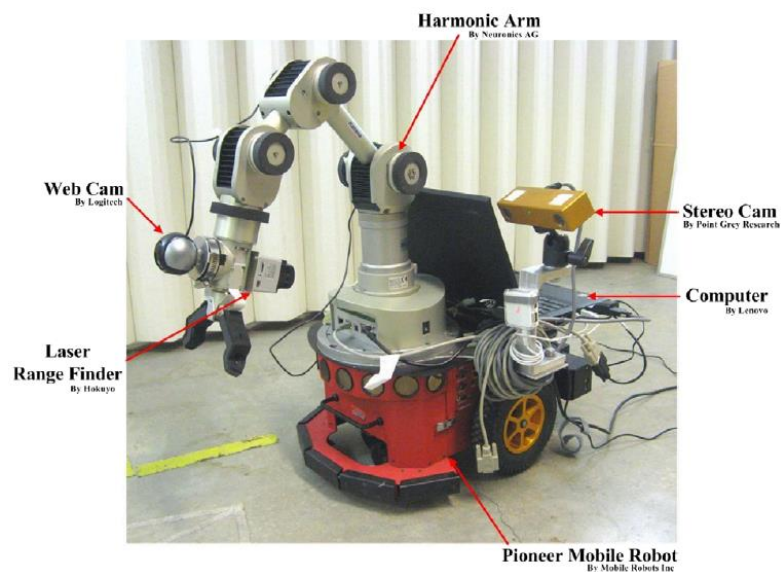
10

Fig. 2. 4. A representative mobile manipulation system with hybrid camera configuration. Reprinted with permission from [37] © Elsevier.

Compared with the cameras, laser-based range finders have a few advantages for distance detection, such as high energy and narrowband wavelength. Based on the laser source and photo detector, the laser ranging can be achieved by the triangulation, Time-of-Flight (ToF) of laser pulses, phase difference of continuous-wave (CW) lasers, and frequency-modulated continuous wave (FMCW). Among them, the laser-pulse ToF and phase-shift CW are more popular, as the simplified diagrams in Figs. 2.5(a)(b). Besides single-point detection, the laser beam can be scanned for target mapping and imaging, which is called laser radar, or LIDAR [9]. A representative robot platform equipped with a LIDAR is as Fig. 2.5(c) and the sampled data (in red) is as Fig. 2.5(d). Although LIDAR performs well for long-distance ranging and localization, it has a relatively large blind zone, which is not suitable for the perception of a near-distance object.
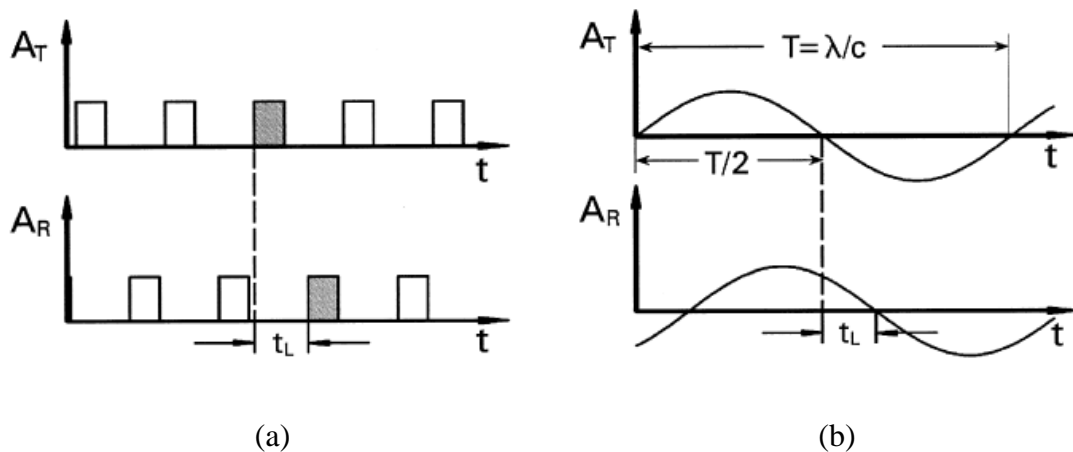
(a)   (b)

<center>(c)   (d)</center>
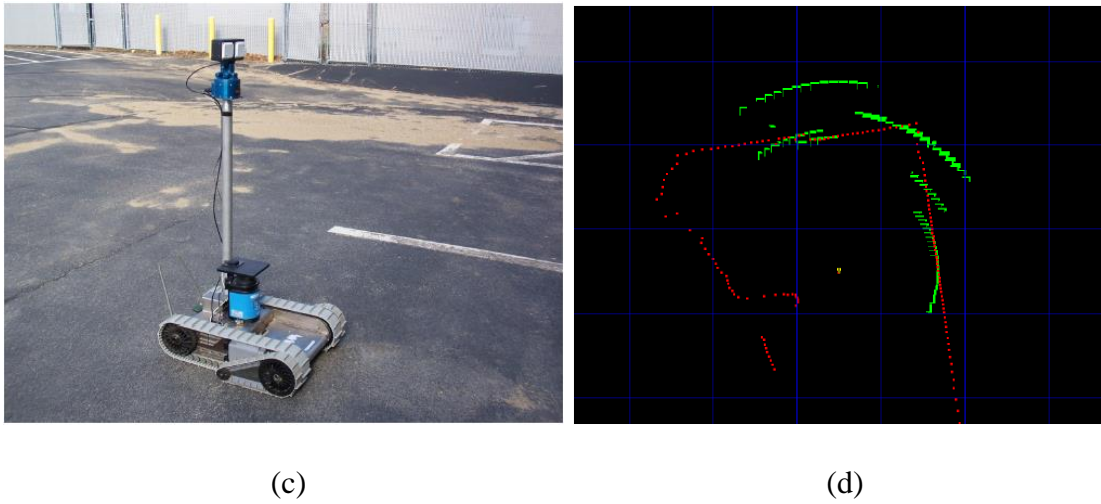
Fig. 2. 5. Simplified diagrams of two principles of LIDAR or laser range finder, based on measuring (a) the ToF of laser pulses, and (b) the phase difference of the CW laser. Reprinted with permission from [9] © Elsevier. (c) A representative robot platform equipped with both a LIDAR and a radar. (d) Collected representative LIDAR (red) and radar (green) data. Reprinted with permission from [38] © IEEE.

Similar as LIDARs, radar ranging can be achieved by the electromagnetic transmitter and receiver with three main principles: angle-of-arrival, received-signal-strength, and propagation-time based systems [39]. Different from LIDAR, radar is capable to detect objects through fuzzy optical visions, such as rain, snow, smoke, and fog. As a result, radar-based Adaptive Cruise Control (ACC) and active brake assist systems have been widely provided as factory options for automobiles. More specifically, ACC systems monitor the range to nearby vehicles and adjust the mobile speed for a safe distance, while active brake assist systems provide additional braking force if a collision is imminent. Shown as Fig. 2.5(c), a radar is equiped on the representative robot

<center>12</center>

platform, and the radar-received data (in green) is shown in Fig. 2.5(d) [38]. Again, radar performs well in long-distance detection, but is not optimal to detect nearby objects for robotic grasping.

Besides cameras, LIDAR, and radar, another long-distance sensor is sonar (sound navigation and ranging), which is more helpful for a navigating robot to detect and map the environment with little prior information. Based on the working principles and mechanisms, sonar can be classified as active and passive ones. Active sonar utilizes a transducer to transmit an acoustic signal/pulse and then detect the bounced back echo for ranging. Passive sonar just hears the coming sound waves, while the object ranging and localization can be achieved by multiple passive sonars. Although sonar has a good performance in water, it has a relatively limited range in air due to the relatively strong acoustic attenuation. In addition, sonar ranging is relatively sensitive to the flatness and orientation of the reflector surface, which may provide either an erroneously long range reading or no reading at all [38]. Again, sonar has a relatively large bind zone, which is not optimal for unknown object perception and then grasping.

2.5 Near-Distance Sensors*5

Although the electromagnetic field, light, and acoustics utilized in the long-distance sensors are not optimal to interrogate the target at a close distance, they have been widely used in near-distance (proximity or pretouch) sensors which are developed in more recent years. The working range of non-contact near-distance sensors is around a few millimeters to centimeters, which is longer than tactile/force sensors, but much

*5Reprinted with permission from "Electric field imaging pretouch for robotic graspers" by J. R. Smith, E. Garcia, R. Wistort, G. Krishnamoorthy, 2007. *In 2007 IEEE/RSJ International Conference on Intelligent Robots and Systems*, 676-683, Copyright 2007 by IEEE.

shorter than camera (or LIDAR, radar, sonar). Ideally, with the assistance of near-distance sensors, robotic fingers can respond to subtle changes in object relative pose right before grasping and adjust operations dynamically. Moreover, the information of object material and (subsurface) structure helps planners better estimate the force distribution, impact characteristics, and friction coefficients. Recent development of near-distance sensors based on electric-field, optical, and acoustic signals has made great progress , but they still suffer from sensing modalities and/or limited types of target materials. The existing non-contact near-distance sensors are discussed as follows.

The principle of the electric-field (capacitive-based) near-distance sensing is illustrated in the simplified diagram [13] in Fig. 2.6(a), where a low-frequency AC voltage is applied to a transmit electrode T, and the induced displacement current is received by the electrode R through C_0. C_0 is modified by the position of object H, which therefore impacts the induced current received by R. Based on the grounded status of the object, the electric-field proximity sensor has two modes. In the shunt mode where the object is well-grounded, the induced current is decreased by the closer distance between sensor and object. In the transmit mode where the object is not coupled to ground, the induced current is increased as the object gets closer. Normally, the human is well-coupled to the ground at the AC operating frequency, which means that conductive objects hold or touched by a person are also well-grounded [15]. The electric-field proximity sensors could handle conductive and nonconductive objects with obvious dielectric contrasts to air [15], such as metals, human body, fruits, vegetables, and water-based liquids. However, thin plastic cases, fabric, thin sheets of paper and thin glass

cannot be well sensed [13] [14] [16]. A representative robotic hand with electric-field pretouch sensors is as Fig. 2.6(b).

<div align="center">(a)</div>

<div align="center">(b)</div>

Fig. 2. 6. Electric-field near-distance sensors for robotic grasping. (a) Lumped circuit model for electric-field sensing of a hand. Reprinted with permission from [13] © IEEE. (b) Photograph of mobile manipulation platform, with electric-field pretouch-enabled hand. Reprinted with permission from [15] © IEEE.

An optical near-distance sensor is normally composed of a light emitter, photoreceiver, and signal processing circuitry. The light from the emitter is reflected by the object surface to be received by the photoreceiver. The time-of-flight (ToF), amplitude, and phase of the reflected light are modulated by the properties of the object surface. More specifically, the detected optical amplitude can be used to estimate the object pose [17], and the ToF of the reflected light can be used to determine the object distance [18]. A representative robotic hand with optical proximity sensors is as Fig.

2.7(a). Unfortunately, the optical proximity sensors lack lateral resolution and cannot handle optically-transparent or highly-reflective targets (Fig. 2.7(b)) [19] [20].

(a)   (b)

Fig. 2. 7. Optical proximity sensors for robotic grasping. (a) Three-fingered Barrett Hand with optical proximity sensors mounted on the fingertips. (b) Failure cases with a shiny can and a transparent cup. Reprinted with permission from [17] © IEEE.

Recently, acoustic-based near-distance sensors have been developed for object sensing. Like a bat, a normal sensor is composed of an acoustic transmitter and a receiver. The transmitter sends an acoustic pulse to the object, and the ToF of the acoustic echo is measured. With the known sound speed, the object distance can be estimated (Fig. 2.8(a)). The acoustic-based near-distance sensor can also localize the object based on the "seashell effect". The seashell-effect sensor is primarily constructed by a miniature metal pipe with a microphone attached to one end (Fig. 2.8(b)), which measures the resonant frequency of the pipe modulated by the object distance [18]. Although the acoustic-based near-distance sensors can primarily range the object distance and even sense the object material/structure, they fail on thin-film, porous, and sound-absorbing objects [21] [22] [40] [24].

(a)　　　　　　　　　　　　　　(b)
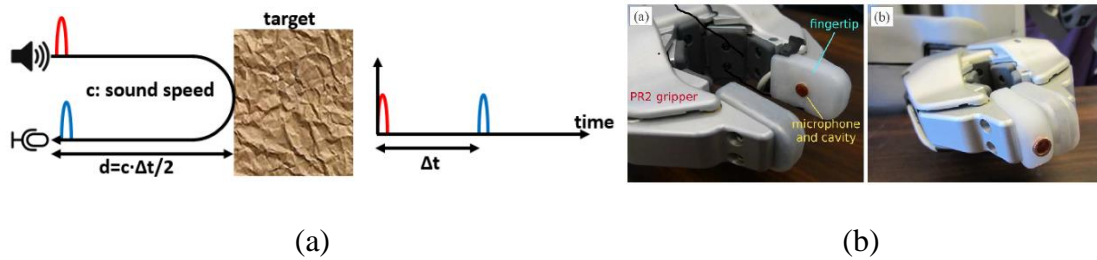
Fig. 2. 8. Acoustic-based proximity sensors for robotic grasping. (a) Simplified diagrams of conventional acoustic ranging. (b) The seashell effect pretouch sensing fingertip on the PR2 robot gripper with finger-surface sensor for extremely compliant objects, and fingertip sensor for adding pretouch point cloud. Reprinted with permission from [40] © IEEE.

2.6 Summary

As a conclusion, the near-distance sensors provide an optimal solution to interrogate the object for robotic grasping, which however still suffer from limited detectable materials due to the sensing modality and mechanism. Here, a dual-modal and dual-sensing-mechanism (DMDSM) near-distance sensor design [25] is proposed by combining pulse-echo ultrasound (US) and optoacoustics (OA) modalities together. The dual modal means the US and OA modalities, and the dual sensing means distance ranging and material/structure differentiation. The ranging is based on the ToFs of the US/OA signals, while the material/structure differentiation is based on the distinctive features extracted from their frequency spectra. As a result, the DMDSM sensor could work on highly-reflective and optically-transparent targets, as well as thin-film, porous, or acoustic-absorbing materials, which cannot be handled by each single modality.

3. DEVELOPMENT OF DMDSM NEAR-DISTANCE SENSOR*

3.1 Introduction

To address the remaining issues of existing non-contact near-distance sensors, a solution is proposed by combining the pulse-echo ultrasound and optoacoustics modalities together, which is named as a dual-modal and dual-sensing-mechanism (DMDSM) design. The dual modal means pulse-echo ultrasound (US) and optoacoustics (OA) modalities [26] [27] (Fig. 3.1), and the dual sensing means distance ranging and material/structure differentiation. The pulse-echo ultrasound (US) utilizes ultrasound signals generated by a transducer to interrogate the distance and material properties of the target. In contrast, the optoacoustics (OA) relies on the direct generation of optoacoustic signals on the target by focused laser pulses. In both modalities, the sensor-object distance is estimated from the ToFs of the US/OA signals, whose frequency spectra are used to extract the distinctive features about the material/structure of the targets. Due to the challenges and limitations in the sensor design, construction, and the performances of the sub-components, such kind of capabilities have not been achieved with a compact sensor package yet. Therefore, a new DMDSM sensor design is developed to accommodate these components together in a compact package, which can work on not only optically-transparent or highly-reflective targets, but also thin-film, porous, or sound-absorbing targets, which are named as optically and/or acoustically challenging targets (OACTs).

18
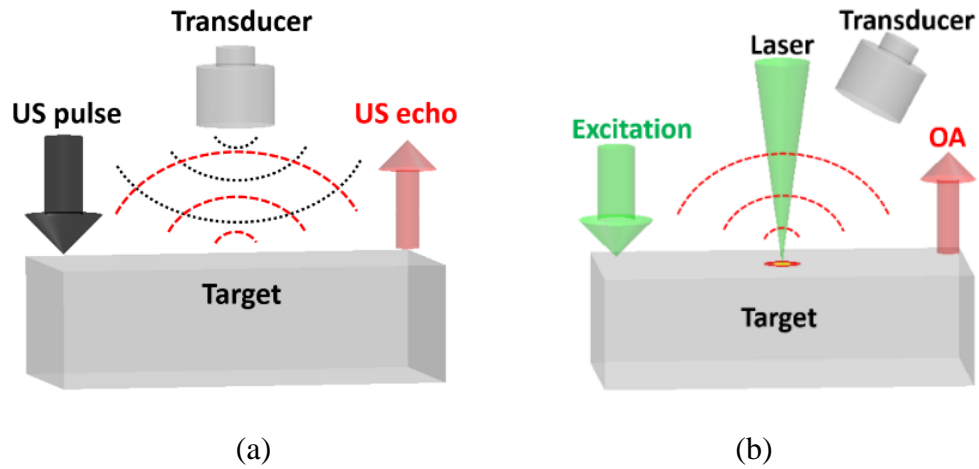
Fig. 3. 1. Conceptual illustrations of the two modalities and sensing mechanisms: (a) pulse-echo ultrasound (US), (b) laser and induced optoacoustics (OA).

To enhance the material/thickness sensing capability by US modality, a novel ultrasound transmitter has been developed to provide wideband acoustic spectra [25]. To verify our design, a prototype DMDSM sensor has been designed, fabricated and tested. The testing results show that the new DMDSM sensor can achieve similar ranging and better material/thickness sensing performance than the previously reported devices [26] [27]. More importantly, they can function well on OACTs, which makes it more practical for real applications in robotic grasping.

3.2 Sensor Design and Operation Principle

The schematic design of the new DMDSM sensor is shown in Fig. 3.2. A planar optically-transparent ring piezoelectric (lead zirconate titanate - PZT) transducer (with a center frequency of 1~2 MHz) is used as both transmitter and receiver. For pulse-echo

ultrasound ranging, the ring transducer sends an ultrasound pulse, which is reflected and focused onto the target surface by a 90-degree parabolic mirror. The reflected or back-scattered echo signal travels along the reverse path and is received by the ring transducer. The ranging is performed based on the time delay between the pulse and echo signals. For optoacoustic ranging, a pulsed laser beam is shot through the center hole of the ring transducer and is reflected and focused onto the target surface to excite wideband optoacoustic signals. Part of the optoacoustic signal travels along the reverse path and is received by the ring transducer. The ranging is performed based on the time delay between the laser triggering and the received optoacoustic signal.
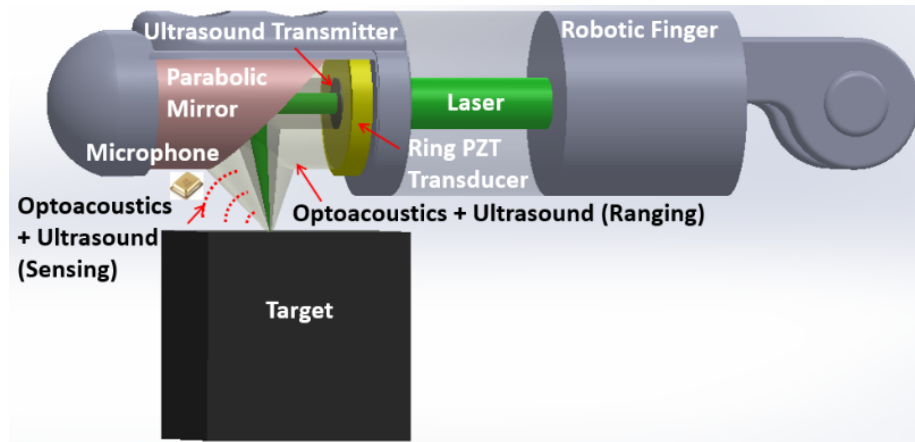
Fig. 3. 2. Schematic of the pulse-echo ultrasound and optoacoustic DMDSM sensor mounted onto a robotic finger. Reprinted with permission from [25] © IEEE.

For targets made of solid or layered materials with thicknesses of mm to cm, the lower-frequency components of the acoustic spectra (up to 10s of kHz) often carry more distinctive features about the material properties and sub-surface structures [41] [42] [43] [44]. Therefore, for optoacoustic material/thickness sensing, a wideband microphone

20

(with an operation range of 0~10s of kHz) is used as the receiver to detect the low-frequency components of the (wideband) optoacoustic signal. However, due to lack of suitable ultrasound transmitters, this creates a challenge in the material/thickness sensing with pulse-echo ultrasound. This is because the microphone can only function as a receiver, while the ring PZT transducer operates at much higher frequencies. Conventional air-coupled transducers are typically narrow-band devices, and such bandwidth cannot be readily obtained with a single transducer. In addition, it is not feasible to accommodate multiple transducers in the (compact) sensor package.

As a key innovative feature in the DMDSM sensor design, a new optoacoustic wideband ultrasound transmitter has been developed to address this issue. The optoacoustic approach is adopted for its capability of wideband transmission. As shown in Fig. 3.3, the optoacoustic wideband ultrasound transmitter consists of a plastic frame with an array of through holes of the same diameter (except the central one), which are covered by a thin layer of laser absorptive polymer material. The other side of the frame is bonded with a shadow mask layer, such that only the free-standing polymer membranes can be effectively illuminated by the pulsed laser for sound generation. The ultrasound from the array of small-diameter polymer membranes merges into a wideband and planar wave, which is reflected and focused onto the target by the parabolic mirror. Laser-absorptive polymer material is selected because of its relatively low Young's modulus and high damping properties, which are more effective for wideband ultrasound transmission. The hole diameter and the distribution of the transmitter array are specially designed to provide a matching bandwidth with that of the

21

microphone. The wideband ultrasound transmitter is located inside the inner hole of the ring PZT transducer, which forms a co-centered and co-axial arrangement (Fig. 3.2). Table 3.1 lists the associated sensor components and their specific functionalities for the DMDSM distance ranging and material sensing.
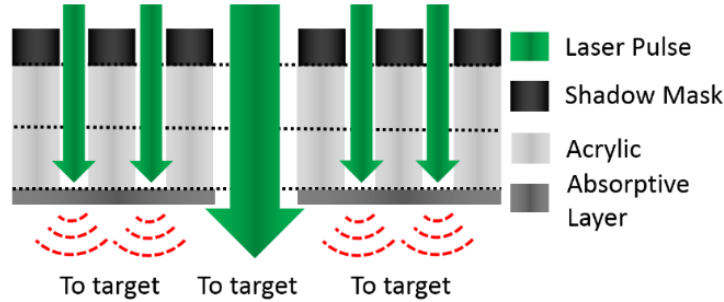
Fig. 3. 3. A diagram of the wideband ultrasound transmitter under pulsed laser illumination. Reprinted with permission from [25] © IEEE.

Table 3. 1. The associated sensor components for DMDSM distance ranging and material sensing. Reprinted with permission from [25] © IEEE.

	Pulse-echo Ultrasound	Optoacoustics
Distance Ranging	Ring transducer (transmitter and receiver)	Pulsed Laser (generator), Ring transducer (receiver)
Material Sensing	Wideband ultrasound (transmitter), Microphone (receiver)	Pulsed Laser (generator), Microphone (receiver)

3.3 Sensor Construction and Testing

Fig. 3.4(a) shows the constructed prototype of the pulse-echo ultrasound and optoacoustic DMDSM sensor. It consists of a 3D-printed housing, a 90-degree parabolic

22

mirror, a microphone with a reception bandwidth of 0~80 kHz, a home-made ring PZT

transducer with 1-MHz resonance frequency, and a custom-made wideband ultrasound

transmitter (Figs. 3.4(b) and 3.4(c)). A window tint film with 5% transmittance is used

as the laser absorptive layer of the wideband ultrasound transmitter. The diameter of the

central hole is 1.5 mm to allow the pulsed laser to pass through for conducting

optoacoustic ranging and material sensing. The window tint film is bonded onto a laser-

cut acrylic frame with an array of 28 through holes with a diameter of 0.5 mm, which

also defines the size of the vibrating membrane for optoacoustic sound generation. The

other side of the frame is covered with a thick layer of black tape as the shadow mask to

prevent the direct illumination of the bonded portion of the window tint film.
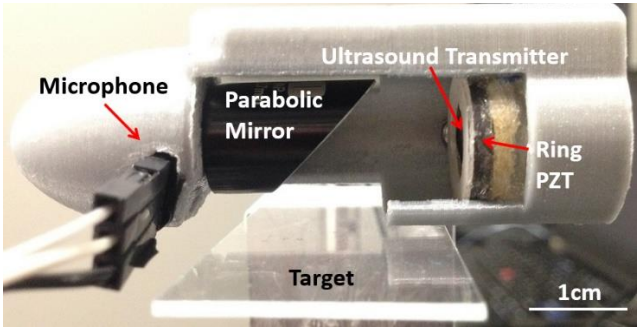
(a)

(b)   (c)

Fig. 3. 4. Photographs of (a) the constructed prototype DMDSM sensor, (b) the

wideband ultrasound transmitter inside the inner hole of the ring PZT transducer (front

view on left and back view on right), and (c) the wideband ultrasound transmitter only (front view on left and back view on right). Reprinted with permission from [25] © IEEE.

To verify the acoustic performance of the wideband ultrasound transmitter, an ultrasound testing is conducted to characterize its transmission bandwidth (Fig. 3.5(a)). A Q-switched 532-nm Nd:YAG pulsed laser is used as the light source with a repetition rate of 10 Hz, a pulse duration of 8 ns, and an average pulse energy of 20 mJ/pulse. The laser beam from the pulsed laser is firstly expanded by two lenses and then filtered by an iris. Based on the area ratio of the vibrating membranes and the whole illuminated region, the laser pulse energy deposition onto each membrane is estimated to be 60 μJ / pulse. To receive the optoacoustic signal, the microphone is fixed at 3 cm in front of the transmitter. A photo detector is used to detect the laser pulse and generate a trigger signal to synchronize the data acquisition. The received signals are amplified by the embedded preamplifier of an ultrasound pulser-receiver and recorded by an oscilloscope. A representative waveform and its frequency spectrum received by the microphone are shown in Figs. 3.5(b) and 3.5(c). The time-domain waveform consists of a series of pulses due to the multiple reflections between the transmitter and the microphone. The frequency spectrum indicates the transmitted bandwidth ranges from 0 to 90 kHz.
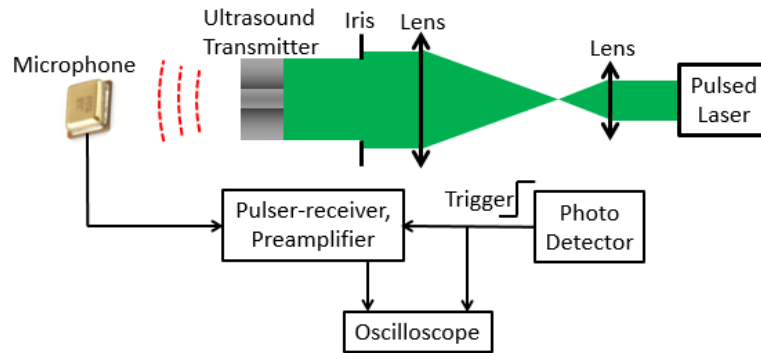
(a)
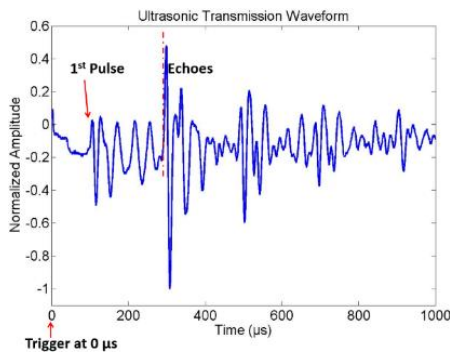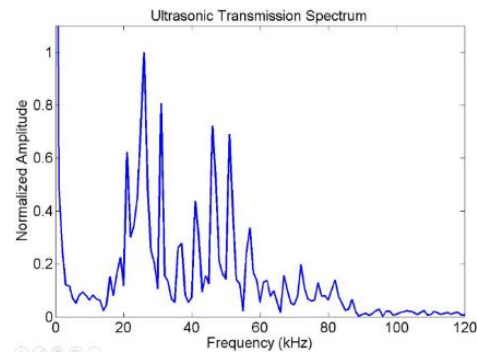
(b)   (c)

Fig. 3. 5. (a) Diagram of the ultrasound testing setup to characterize the wideband ultrasound transmitter. (b) Representative waveform and (c) frequency spectrum of the ultrasound signal received by the microphone. Reprinted with permission from [25] © IEEE.

3.4 Ranging Experiments and Results

A testing setup has been built to characterize the pulse-echo ultrasound and optoacoustic ranging and sensing performance of DMDSM sensor (Fig. 3.6). The same pulsed laser setup is used as the light source for optoacoustic excitation (Fig. 3.5(a)). The central part of the laser beam passes through the wideband ultrasound transmitter and is

incident onto the target for optoacoustic distance ranging and material sensing (Fig. 3.6(b)). The outer part of the laser beam is incident onto the ultrasound transmitter to excite and send a wideband ultrasound pulse onto the target for pulse-echo ultrasound material sensing (Fig. 3.6(c)). Driven by the pulser-receiver, the ring PZT transducer transmits an ultrasound pulse to the target and also receives the echo signal from the target for pulse-echo ultrasound distance ranging (Fig. 3.6(d)). Both the laser and the transmitted ultrasound are reflected and focused by the parabolic mirror to improve the lateral resolution. The higher-frequency components of the excited optoacoustic signals and reflected ultrasound signals are received by the ring PZT transducer for distance ranging, while the lower-frequency ones are detected by the microphone for material sensing. For simultaneous DMDSM distance ranging and material sensing, a photo detector is used to detect the laser pulse and generate a trigger signal to synchronize the operations of the pulsed laser, the pulser-receiver and the oscilloscope. The received signals are amplified by the preamplifier embedded in the pulser-receiver, captured and recorded by the oscilloscope.

(a)

26
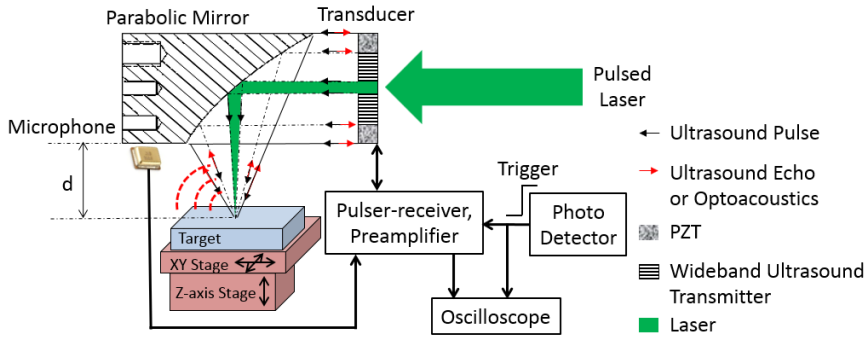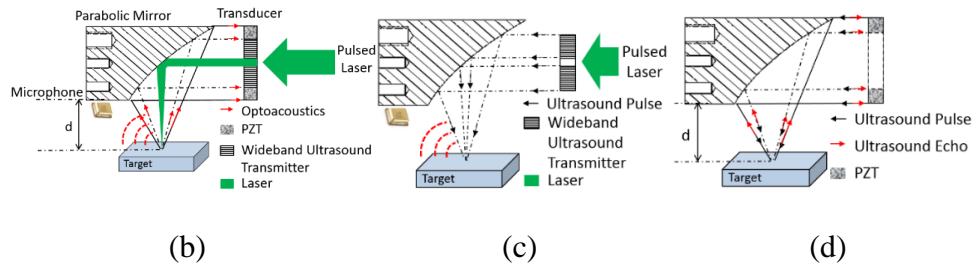
Fig. 3. 6. Diagrams of (a) the general setup to characterize the pulse-echo ultrasound and optoacoustic ranging and sensing performance of the DMDSM sensor, (b) the sub-setup of optoacoustic distance ranging and material sensing, (c) the sub-setup of pulse-echo ultrasound material sensing, (d) the sub-setup of pulse-echo ultrasound distance ranging. Reprinted with permission from [25] © IEEE.

3.4.1 Pulse-Echo Ultrasound Distance Ranging

For pulse-echo ultrasound distance ranging, a piece of 1-mm-thickness glass slide is used as the target [27]. The distance (d) between the parabolic mirror and the glass slide is decreased from 6.5 mm to 0 with a decrement of 0.5 mm. Fig. 3.7(a) shows a representative pulse-echo ultrasound signal from the ring PZT transducer. The measured distance vs. the real distance (d) and their deviations are shown in Figs. 3.7(b) and 3.7(c), respectively. The deviation is smaller than 0.24 mm when the target is within the ultrasound focal zone where d is between 3.5 mm and 5.5 mm. The same setup is used to quantify the lateral resolution of the pulse-echo ultrasound, except that the glass slide target is replaced by a copper wire with a diameter around 0.7 mm. After repeating the linear scan at different distance (d) from 1.5 mm to 6.5 mm, the ultrasound lateral resolution is determined by the minimal acoustic focal diameter (Fig. 3.7(d)), indicating

27

the lateral resolution is around 1.04 mm at the focal length d = 4.5 mm. The measured

depth of focus is around 2.0 mm where d is from 3.5 mm to 5.5 mm.

(a)

(b)

(c)

(d)
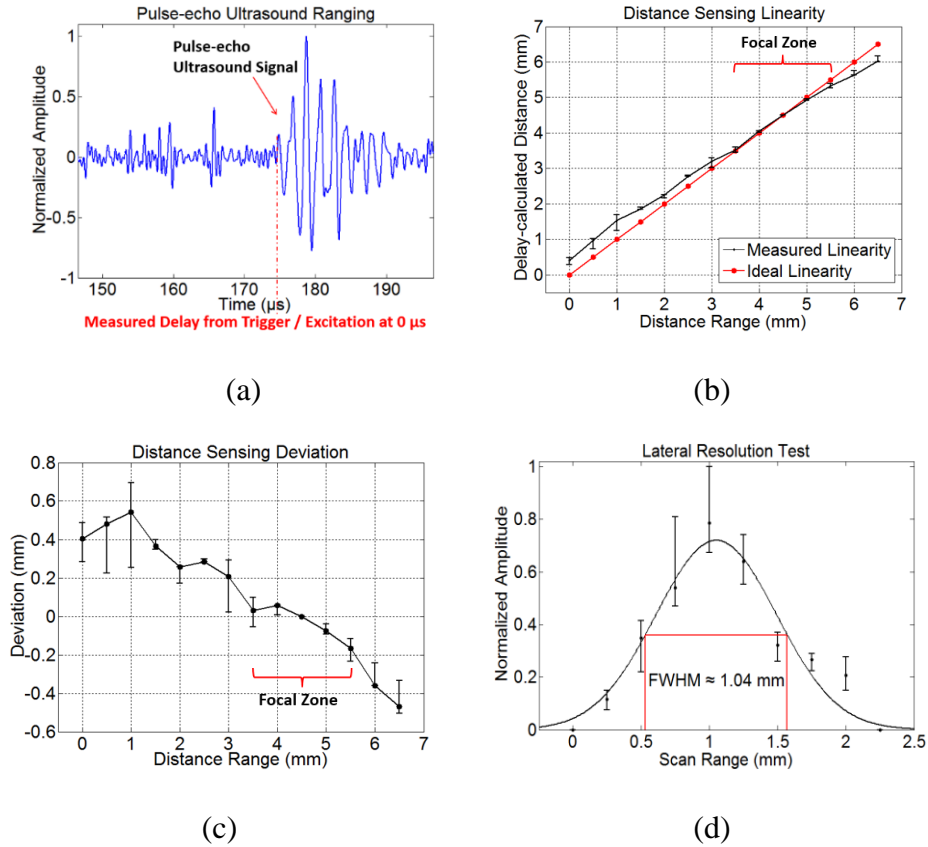
Fig. 3. 7. (a) Representative pulse-echo ultrasound signal, showing the measured delay
from trigger / excitation. (b) Comparison between measured (in black) and real (in red)
distances. (c) Deviation of the measured distance from the real distance. (d) Ultrasound
lateral resolution 1.04 mm determined from the minimal acoustic focal diameter at d=4.5
mm. Reprinted with permission from [25] © IEEE.

3.4.2 Optoacoustic Distance Ranging

The optoacoustic distance ranging is characterized with a thin 0.1-mm copper wire as the target [26]. The distance (d) between the parabolic mirror and the target is decreased from 8 mm to 5 mm with a decrement of 0.5 mm. Fig. 3.8(a) shows a representative optoacoustic signal received by the ring PZT transducer. The measured distance vs. the real distance (d) and their deviations are shown in Figs. 3.8(b) and 3.8(c), respectively. The deviation is smaller than 0.12 mm when the target is within the optoacoustic focal zone where d is between 5.5 mm and 6.5 mm. The same setup (Fig. 3.6) is used to quantify the optoacoustic lateral resolution, where the same copper wire is scanned laterally. After repeating the linear scan at different distance (d) from 5.0 mm to 8.0 mm, the optoacoustic lateral resolution is determined by the minimal optoacoustic focal diameter (Fig. 3.8(d)), indicating the lateral resolution around 95 μm at the focal length d = 6.0 mm. The measured depth of focus is around 1.0 mm where d is from 5.5 mm to 6.5 mm.

(a)   (b)
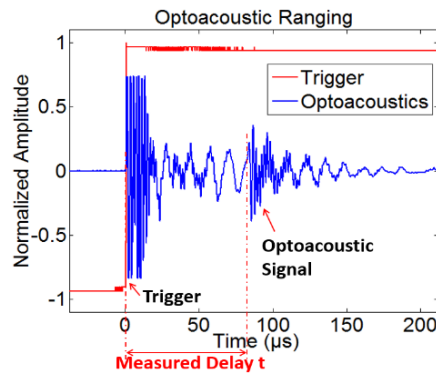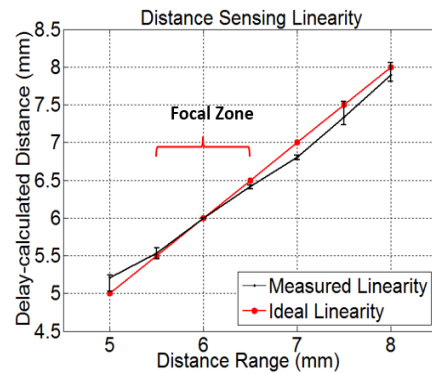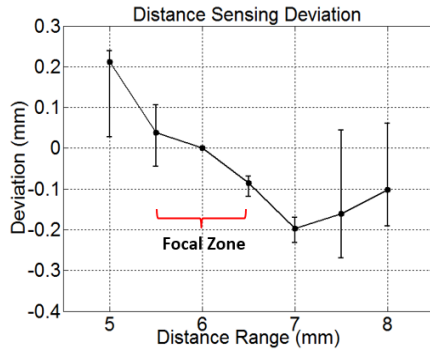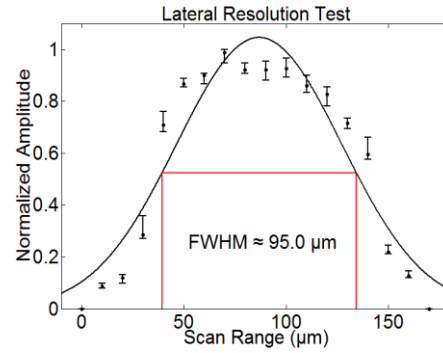
Fig. 3. 8. (a) Representative optoacoustic signal, showing the measured delay between "Trigger" and "Optoacoustic Signal". (b) Comparison between the measured (in black) and the real (in red) distances. (c) Deviation of the measured distance from the real distance. (d) Optoacoustic lateral resolution 95 μm determined from the minimal optoacoustic focal diameter at d = 6.0 mm. Reprinted with permission from [25] © IEEE.

3.5 Material Sensing Experiments and Results

3.5.1   Data Acquisition and Classification

For material sensing, the lower-frequency components of the excited optoacoustic and reflected ultrasound echo signals received by the microphone are used. Theoretically, the optoacoustic signals will arrive at the microphone earlier than the ultrasound echoes because of its shorter travel distance (e.g., from target to microphone vs. from transmitter to target and then microphone) (Fig. 3.6). However, due to their relatively long durations, these lower-frequency components would mix with each other when received by the same microphone. Depending on the optical and mechanical properties of the target, the received signals could mainly consist of either target-induced

30

optoacoustic signal, or target-reflected ultrasound echo signal, or both. This kind of DMDSM signals is expected to provide more distinctive features for the material sensing. The material differentiation is performed with a Bag-of-SFA-Symbols (BOSS) classifier [45] [46]. The classifier is trained to identify the different materials, where the original data set is randomly divided into the training and testing data with 3:1 ratio without overlapping. The experimental data are transformed into BOSS histograms, serving as feature set for classification. After 50 random trials, the BOSS classifier gives the confusion matrix to show the accuracy of classification.

3.5.2   Material / Thickness Differentiation

To compare the performance of the new DMDSM sensor with that of the previous works [26] [27], the same group of targets, including steel, aluminum, acrylic, rubber, paper, and also aluminum sheets with different thickness have been used for material/thickness differentiation. Unlike the previous experiments, no black ink is coated on the targets even with low optical absorption. The collected DMDSM acoustic spectra are shown in Figs. 3.9 and 3.10. The confusion matrices given by BOSS classifier indicate a 100% accuracy of the material differentiation and thickness classification (Fig. 3.11), which is even better than the accuracies of 87% - 97% and 94% - 100% obtained in previous works [26] [27].
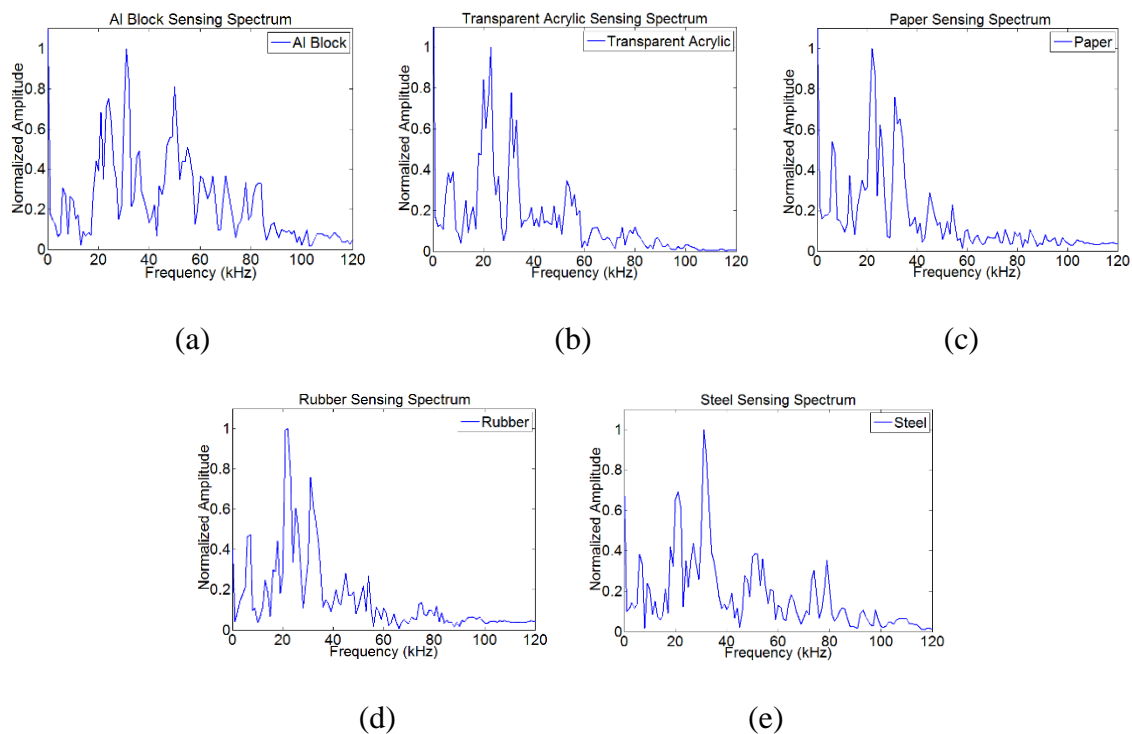
Fig. 3. 9. Representative DMDSM acoustic spectra from (a) aluminum block, (b) acrylic, (c) paper, (d) rubber, and (e) steel. Reprinted with permission from [25] © IEEE.

(a)   (b)   (c)   (d)

(e)   (f)   (g)
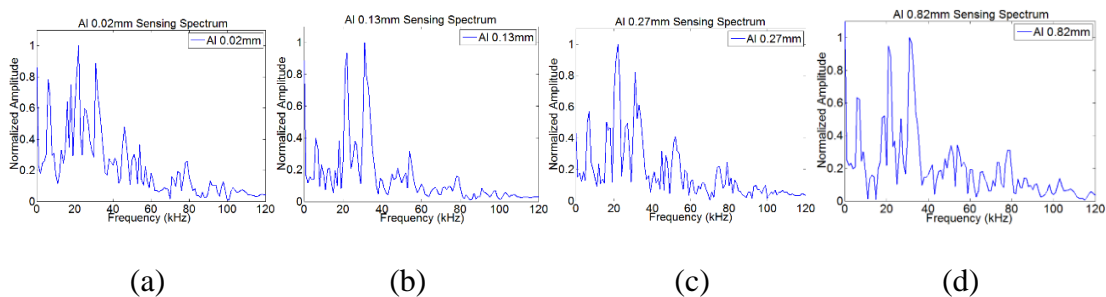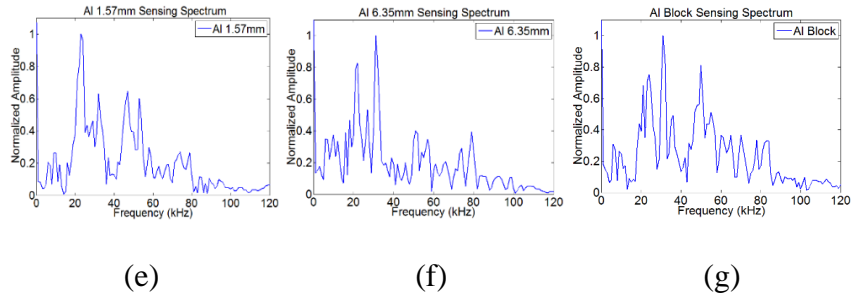
Fig. 3. 10. Representative DMDSM acoustic spectra from aluminum sheets with different thickness. Reprinted with permission from [25] © IEEE.

(a)   (b)
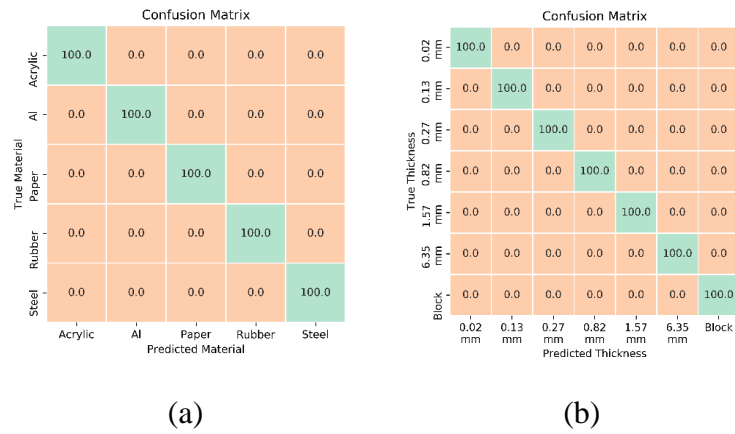
Fig. 3. 11. BOSS classifier averaged confusion matrix of (a) different materials and (b) aluminum sheets with different thickness. Reprinted with permission from [25] © IEEE.

3.5.3   Differentiation of Challenging Targets

To demonstrate the enhanced material sensing capabilities of the new DMDSM sensor, eight OACTs are tested (Fig. 3.12), including four optically-transparent targets of glass, acrylic, PET (polyethylene terephthalate), PDMS (polydimethylsiloxane) (Figs. 3.12(a)-(d)) with low optoacoustic generation efficiency, and four dark thin/porous targets of fabric, foam, paper, window tint film (Figs. 3.12(e)-(h)) with weak acoustic

33

reflection. To compensate the target thickness difference, the height of Z-axis stage is adjusted until the target top is at the focus of the parabolic mirror (Fig. 3.6). The representative DMDSM acoustic spectra from the eight targets are shown in Fig. 3.13. BOSS classifier gives the confusion matrix showing an 100% accuracy for all the targets (Fig. 3.14). This result demonstrates the capability of differentiating OACTs with the new DMDSM sensor.

| (a) | (b) | (c) | (d) |

| (e) | (f) | (g) | (h) |
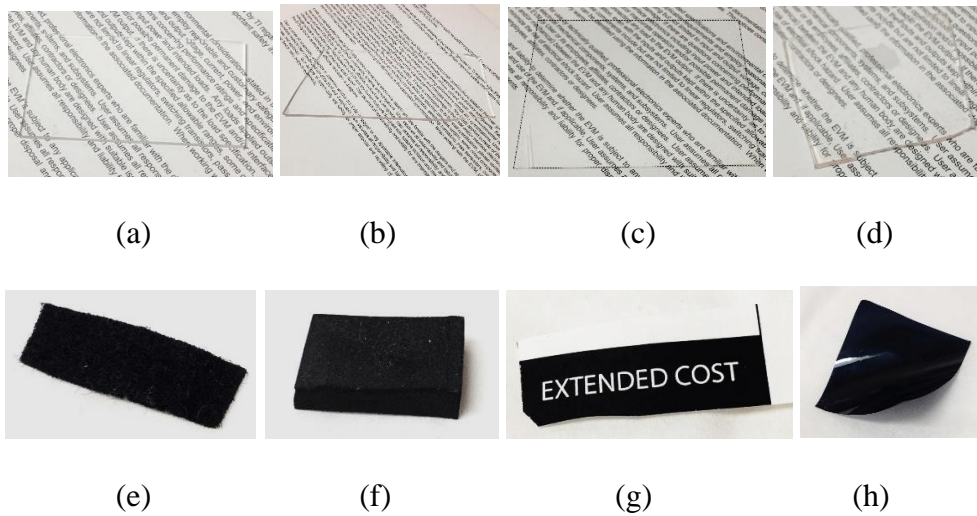
Fig. 3. 12. Photos of the eight OACTs: (a)−(d) optically-transparent targets of glass, acrylic, PET (with contour marked by dash line), PDMS with thicknesses around 1.0 mm, 1.6 mm, 0.11 mm, and 1.5 mm separately, and (e)−(h) dark thin/porous targets of fabric, foam, paper, window tint film with thicknesses around 2 mm, 8 mm, 0.1 mm, 0.06 mm separately. Reprinted with permission from [25] © IEEE.

(a)   (b)   (c)   (d)

(e)   (f)   (g)   (h)
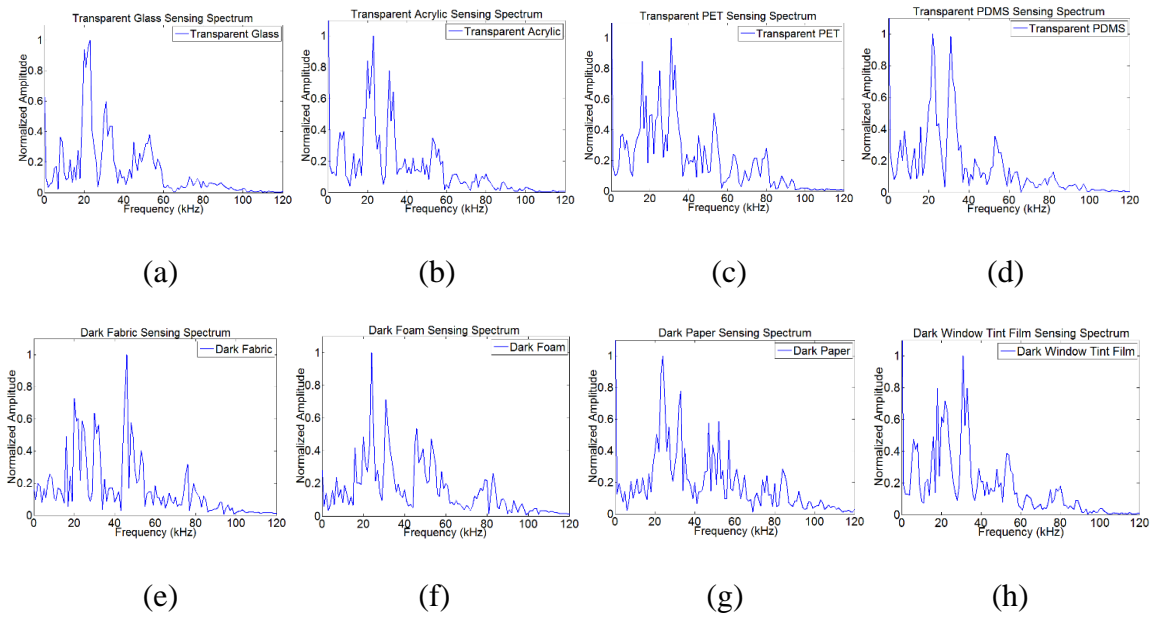
Fig. 3. 13. Representative DMDSM acoustic spectra from (a)−(d) optically-transparent targets and (e)−(h) dark thin/porous targets. Reprinted with permission from [25] © IEEE.

Fig. 3. 14. BOSS classifier averaged confusion matrix of the eight OACTs. Reprinted with permission from [25] © IEEE.

3.6 Summary

In this chapter, a DMDSM sensor for near-distance ranging and material/structure sensing for robotic grasping has been demonstrated. The experimental results have proved the initial success of the DMDSM sensor in distance ranging and material/structure differentiation upon conventional targets as well as OACTs with high accuracy.

4. SIMPLIFICATION OF DMDSM SENSOR CONFIGURATION*

4.1 Introduction

Although the DMDSM sensor [25] worked well as a prototype in the initial demonstration, it has a relatively complex configuration which makes its construction and operation complicated and thus limits its performance and functionalities in real grasping applications. As the flow chart in Fig. 4.1(a), the first-generation (G1) DMDSM sensor has to utilize two ultrasound transmitters and two ultrasound receivers for handling the low- and high-frequency US/OA signals for ranging and material/structure sensing. This is because the two transmitters and receivers have relatively narrow bandwidths without enough overlapping with each other. Another issue is that as the low-frequency acoustic receiver, the microphone has a wide reception angle and is sensitive to ambient noise in the surrounding environment. Although the environmental noise may be canceled by adding a second microphone, it will make the DMDSM sensor even more complex. In addition, the pulser-receiver generates high-voltage electric pulses, which could make the DMDSM sensor unsafe to work in flammable or explosive environments. Moreover, one pulser-receiver unit, which is bulky and expensive, can only interface with one DMDSM sensor, making it impractical to build and operate multiple sensors simultaneously on a robotic hand.

To address these issues, a second-generation (G2) DMDSM sensor has been developed as the flow chart in Fig. 4.1(b). Obviously, the configuration is much simplified, which is made possible by widening the acoustic bandwidth of the ultrasound

transmitter and receiver. As a result, with wider acoustic bandwidths, a single ultrasound transmitter and receiver are enough to handle both the low- and high-frequency US/OA signals for ranging and material/structure sensing. Besides, one laser pulse (delivered by optical fiber) could initiate both US and OA signals collection, which makes the system construction and operation much simpler and more straightforward. In addition, the new configuration makes the microphone and pulser-receiver unnecessary.

In this chapter, the G2 DMDSM sensor is demonstrated with its design, construction, and characterization. An object scanning system has been built with the G2 DMDSM sensor, and scanning experiments have been conducted on common household objects with different materials and shapes. The experimental results show that the new sensor can achieve good ranging and material/structure differentiating performances. In conclusion, the new DMDSM sensor provides a practical and powerful solution for ranging and material-type/interior-structure sensing to assist robotic grasping of unknown objects.

(a)   (b)
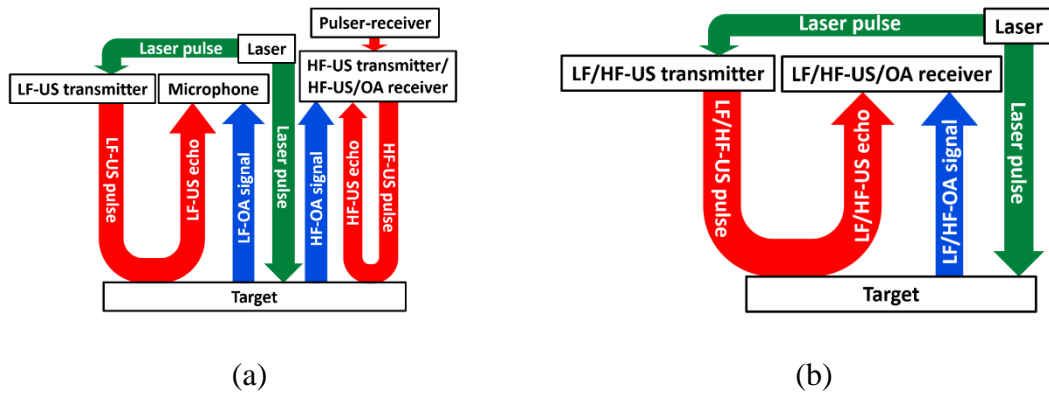
Fig. 4. 1. The flow charts showing the working principles of (a) G1 and (b) G2 DMDSM sensors. HF: high-frequency; LF: low-frequency; US: ultrasound; OA: optoacoustic. Best viewed in color. Reprinted with permission from [28] © IEEE.

4.2 Sensor Design, Construction, and Testing

The schematic design of the new DMDSM sensor is shown in Fig. 4.2, which consists of only one (optoacoustic) ultrasound transmitter and receiver in a co-centered and co-axial configuration. Driven by the laser pulses delivered through the optical fiber, the ultrasound transmitter sends both low- and high-frequency ultrasound pulses to the target, and the echo signals are collected by the ring-shaped transducer. US ranging and sensing are conducted based on the time delays and frequency spectra of the echo signals, respectively. For OA ranging and sensing, the inner part of the laser pulses passes through the center hole of the optoacoustic ultrasound transmitter onto the surface of target (after parabolic mirror reflection), and the induced OA signals are also collected by the ring-shaped transducer. Their time delays and frequency spectra are used for OA ranging and material/structure sensing, respectively. Therefore, the same laser pulse will trigger both US and OA signals collection by the same receiver, which makes the sensor operation and data acquisition simple and straightforward. Besides, the single triggering scheme does not mix US and OA signals. This is because the US signal goes through a round trip (transmitter-target-receiver) with a time delay twice that of the OA signal after a single trip (target-receiver), and their temporal difference is much longer than their durations.
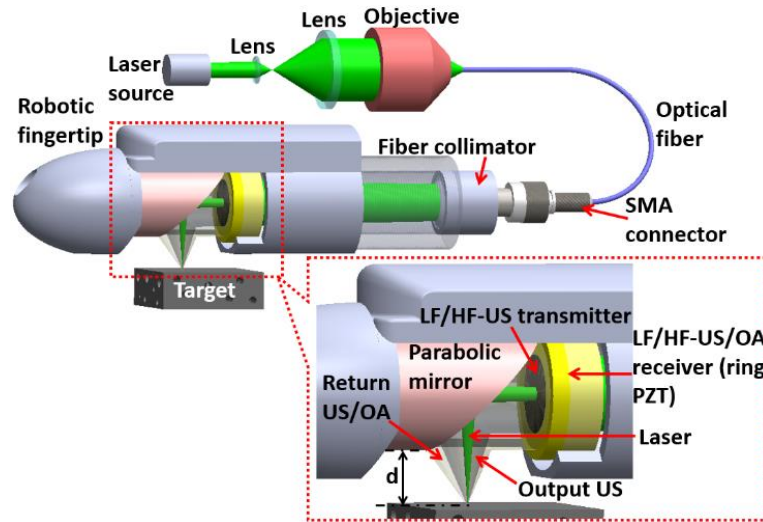
Fig. 4. 2. Schematic design of the new DMDSM sensor. HF: high-frequency; LF: low-frequency; US: ultrasound; OA: optoacoustic.

For the new DMDSM sensor, both low- and high-frequency ultrasound signals for US ranging and material/structure sensing have to be generated by the single optoacoustic ultrasound transmitter. To address this challenge, the optoacoustic ultrasound transmitter (Fig. 4.3) is designed by consisting of an optically-transparent acrylic as the supporting substrate and a layer of black vinyl electrical tape as the laser-absorption layer. Both acrylic and vinyl have low Young's modulus (~GPa) and high internal damping, which allows effective generation of wideband ultrasound signals from low-frequency (~kHz) flexural and high-frequency (~MHz) thickness modes. The acrylic substrate has a thickness of 1.6 mm and a diameter of 9 mm. A center hole with a diameter of 1.5 mm allows the laser pulses to pass through for OA ranging and material/structure sensing. Similarly, both low- and high-frequency US/OA signals for ranging and material/structure sensing have to be detected by the single ring PZT

40

transducer. To address this challenge, the ring PZT transducer (Fig. 4.3) is designed with a thick backing layer to damp the acoustic resonance, and a large inner diameter to induce multiple modes of vibration, e.g., radial (~kHz) and thickness (~MHz) modes. As a result, the bandwidth of the ring PZT transducer is wide enough to match that of the optoacoustic ultrasound transmitter.
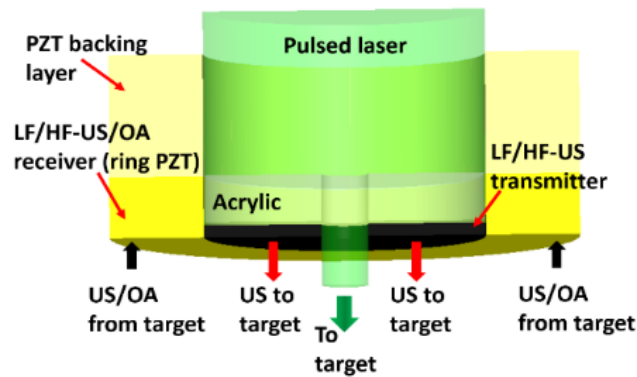
Fig. 4. 3. A zoom-in diagram of the cross-section of the designed optoacoustic ultrasound transmitter integrated with the ring PZT transducer under pulsed laser illumination, which form a co-centered and co-axial arrangement. HF: high-frequency; LF: low-frequency; US: ultrasound; OA: optoacoustic.

The collective bandwidth of the optoacoustic ultrasound transmitter and ring PZT transducer is characterized (Fig. 4.4(a)). A Q-switched 532-nm Nd:YAG pulsed laser is used as the light source with a repetition rate of 10 Hz, a pulse duration of 8 ns, and an average pulse energy of 20 mJ/pulse. With a neutral density filter covering the laser head, the laser pulse energy is reduced to around 2.5 mJ/pulse to protect the optoacoustic transmitter from being burnt. The laser beam from the pulsed laser is expanded by two lenses and then filtered by an iris. A photo detector is used to detect the laser pulse and

generate a trigger signal to synchronize the data acquisition. The received signals are amplified by a preamplifier and recorded by an oscilloscope. A representative waveform and its frequency spectrum [28] received by the ring PZT transducer are shown in Figs. 4.4(b) and 4.4(c), respectively. The time-domain waveform consists of two pulses due to multiple acoustic reflections between ultrasound transmitter and ring PZT transducer. The acoustic frequency spectrum indicates the collective bandwidth of the optoacoustic ultrasound transmitter and ring PZT transducer with center frequencies around 80 kHz, 532 kHz, and 728 kHz.

(a)

(b)

(c)
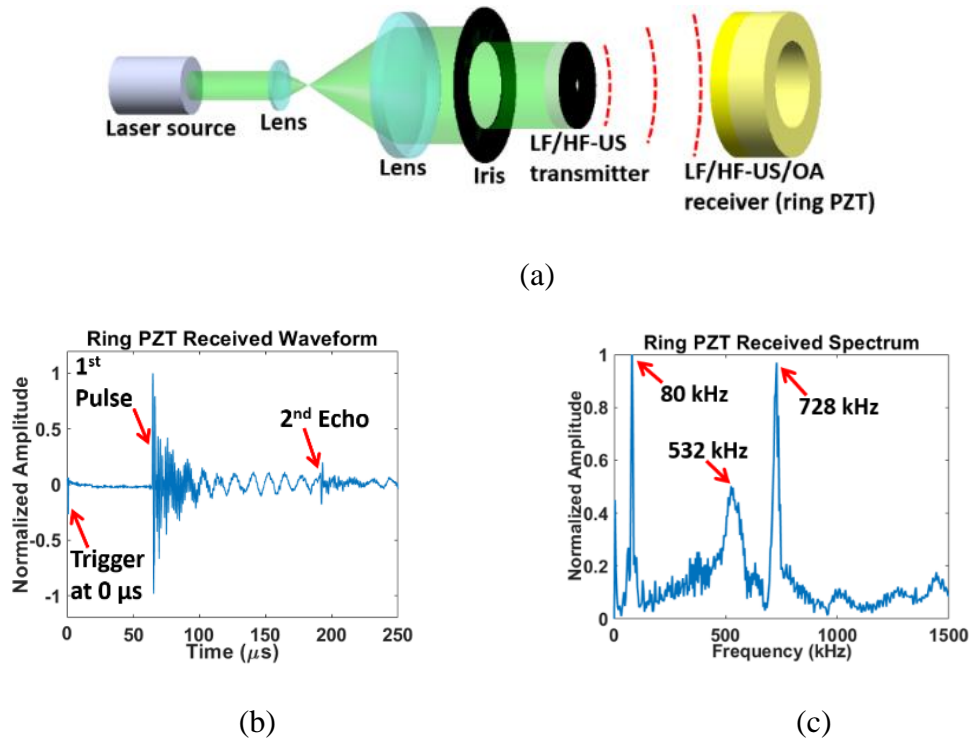
Fig. 4. 4. (a) Diagram of the setup in air to characterize the collective bandwidth of the optoacoustic ultrasound transmitter and ring PZT transducer in new DMDSM sensor. HF: high-frequency; LF: low-frequency; US: ultrasound; OA: optoacoustic.

Representative (b) waveform and (c) frequency spectrum of the received ultrasound signals. Reprinted with permission from [28] © IEEE.

Fig. 4.5(a) shows the fabricated prototype of the new DMDSM sensor, consisting of a 3D-printed housing, a 90-degree parabolic mirror, an (optoacoustic) ultrasound transmitter, a ring PZT transducer, a 3D-printed coupler, a fiber collimator, and an optical fiber. A testing setup is built (Fig. 4.2) to characterize its US and OA ranging and material/structure sensing performances. The same pulsed laser in Fig. 4.5(a) is used, and one laser pulse initiates simultaneous US and OA data acquisition (Fig. 4.5(b)). The time delays of the 1st OA signal, the US signal, and the 2nd OA signal (echo after a round trip) are around 77 µs, 154 µs, and 231 µs, respectively. Their temporal separations are long enough for isolating the US and OA signals from each other for ranging and sensing.

(a)   (b)
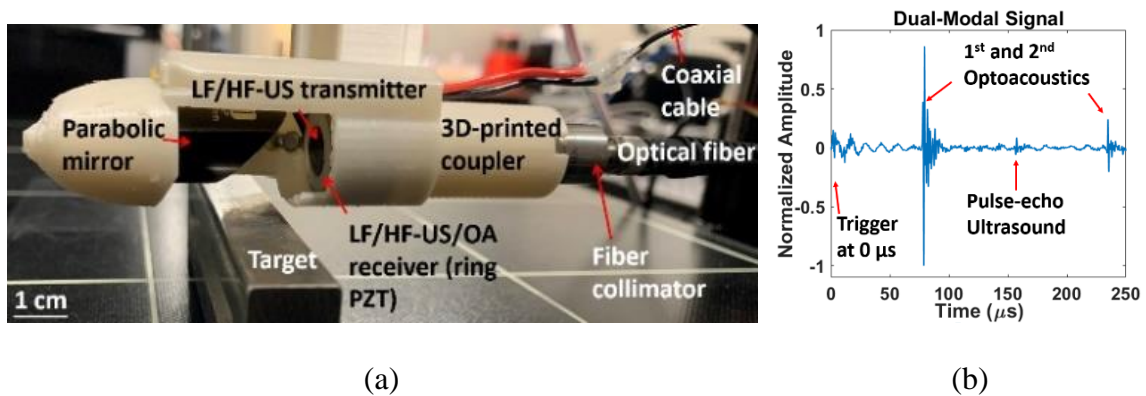
Fig. 4. 5. (a) A close-up photograph of a fabricated prototype of the new DMDSM sensor. HF: high-frequency; LF: low-frequency; US: ultrasound; OA: optoacoustic. (b)

Representative waveform including the received US and OA signals from an aluminum block target through air.

4.3 Ranging Experiments and Results

4.3.1   US Distance Ranging

The US ranging performance of the new DMDSM sensor is characterized by the setup (Fig. 4.2) using a piece of 1-mm-thickness glass slide as the target. The distance (d) between the parabolic mirror and the glass slide is decreased from 18.0 mm to 6.0 mm with a decrement of 0.5 mm. The measured distance vs. the real distance (d) and their deviations are shown in Figs. 4.6(a) and 4.6(b), respectively. With a second-order polynomial fitting and calibration, the deviation is less than 0.20 mm where d is from 6.0 mm to 18.0 mm. The same setup is used to quantify the lateral resolution of the pulse-echo ultrasound ranging, except that the glass slide target is replaced by a copper wire with a diameter around 0.7 mm. After repeating the lateral scans at different distance (d) from 6.0 mm to 18.0 mm, the ultrasound lateral resolution is determined by the minimal acoustic focal diameter (Fig. 4.6(c)), indicating the lateral resolution around 0.75 mm at the focal length $d = 10.0$ mm. The measured depth of focus (DOF) is around 4.5 mm where d changes from 8.0 mm to 12.5 mm.
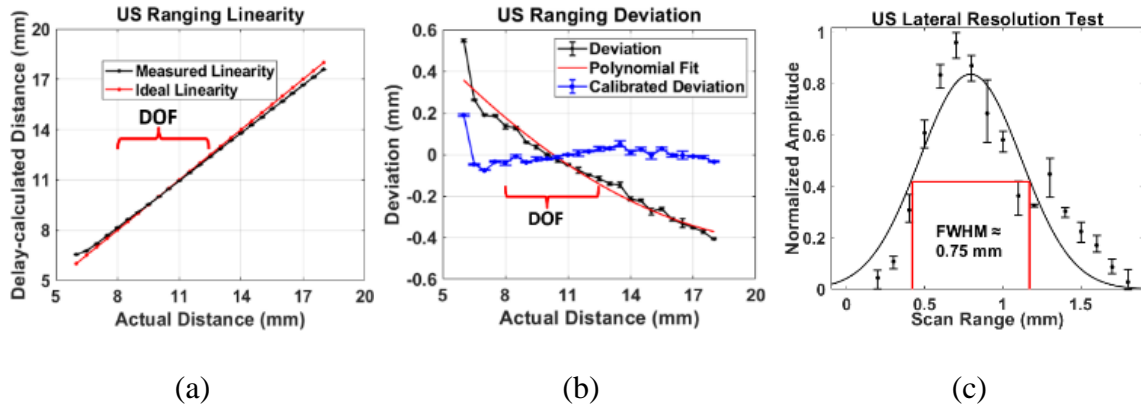
Fig. 4. 6. (a) Comparison between the US measured (in black) and actual (in red) distances. (b) Deviation of the US measured distance from the real distance. (c) US lateral resolution around 0.75 mm determined by the minimal acoustic focal diameter at d = 10.0 mm.

4.3.2 OA Distance Ranging

The OA ranging performance of the new DMDSM sensor is characterized by the similar setup (Fig. 4.2) using an aluminum block as the target. The distance (d) between the parabolic mirror and the aluminum block is decreased from 18.0 mm to 6.0 mm with a decrement of 0.5 mm. The measured distance vs. the real distance (d) and their deviations are shown in Figs. 4.7(a) and 4.7(b), respectively. Similarly, with a second-order polynomial fitting and calibration, the deviation is reduced to be less than 0.16 mm where d is from 6.0 mm to 18.0 mm. The same setup is used to quantify the OA lateral resolution, except that the aluminum block target is replaced by a tungsten wire with a diameter around 0.4 mm. After repeating the lateral scans at different distance (d) from 6.0 mm to 18.0 mm, the OA lateral resolution is determined by the minimal OA focal

45

diameter (Fig. 4.7(c)), indicating a lateral resolution ~392 μm at the focal length ($d = 9.5$ mm). The measured DOF is around 4.0 mm where d changes from 8.0 mm to 12.0 mm.

(a) (b) (c)
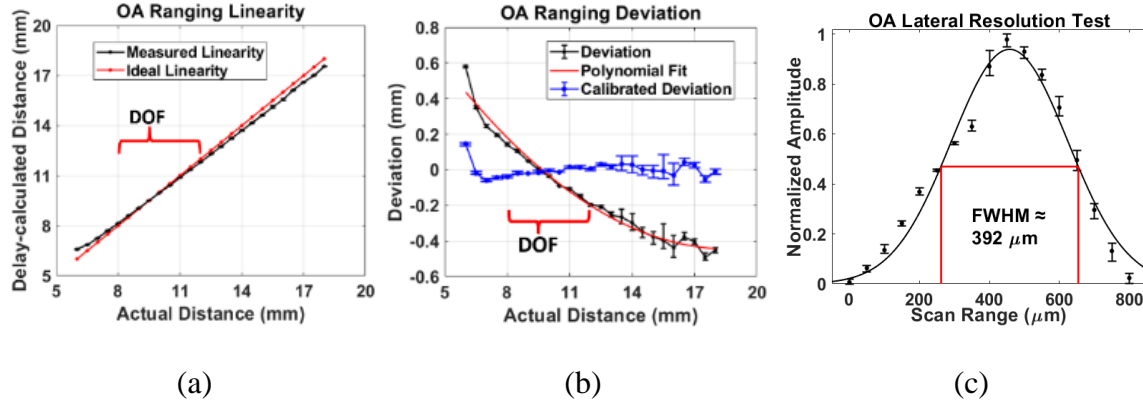
Fig. 4. 7. (a) Comparison between the OA measured (in black) and the real (in red) distances. (b) Deviation of the OA measured distance from the real distance. (c) OA lateral resolution of 392 μm determined by the minimal OA focal diameter at $d = 9.5$ mm.

4.3.3 US/OA Ranging vs. Surface Angle

The previous ranging characterizations are based on horizontal target surface with 0º. However, this is not always the case for an actual object to grasp. Therefore, the US/OA ranging deviations vs. target surface angle of the new DMDSM sensor is characterized with the setup in Figs. 4.8(a) and 4.8(b), by using a customized aluminum block with surfaces in different angles (±3º, ±6º, ±9º) as the target. The pillars on both ends are used as alignment markers to maintain the scanning path at different sensor-target distance. To boost up the OA amplitude, a thin layer of black paint is coated on the aluminum surface. The aluminum block is scanned in X and Y axes, and the

measured ranging deviation vs. angle at different distance are shown in Figs. 4.8(c)-(f), after second-order polynomial fitting and calibration. For distance from 6 mm to 18 mm, the maximum US/OA deviations are less than 0.2 mm, which indicates the robust tolerance of the DMDSM sensor upon different angle of the target surface.

(a)   (b)   (c)

(d)   (e)   (f)
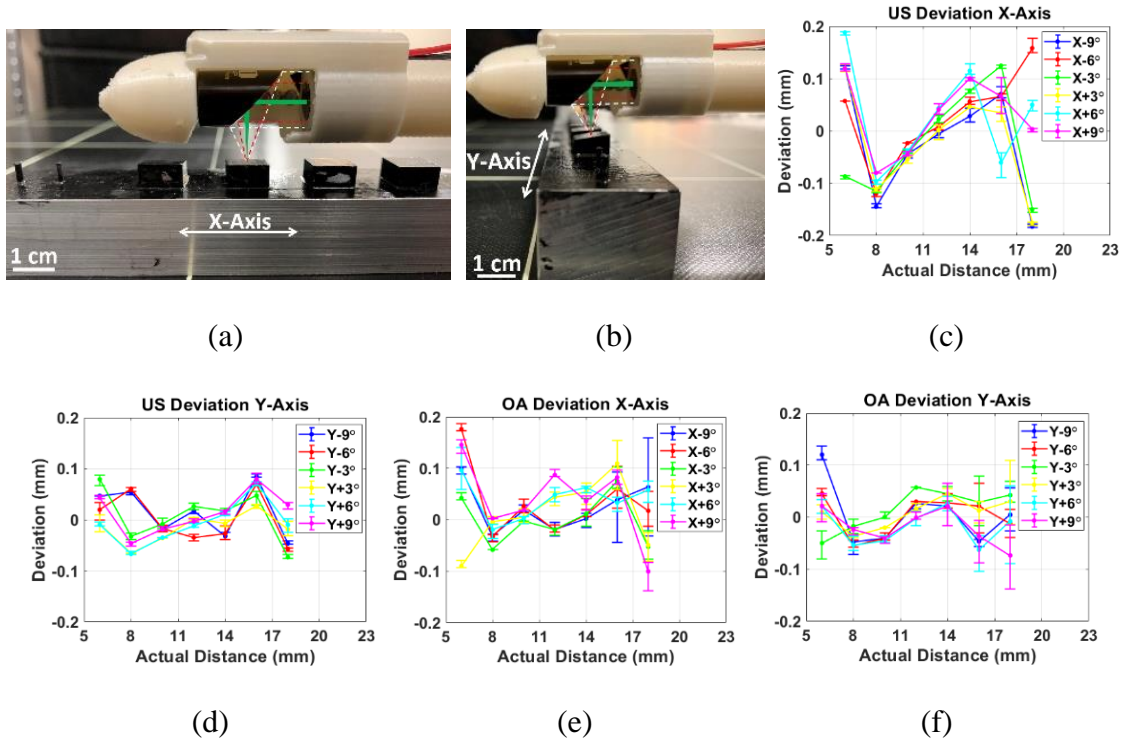
Fig. 4. 8. Photos of the Al block with surfaces of different angles scanned in (a) X and (b) Y axis, where the US transmission and US/OA reception are indicated by the red- and white-dashed lines, respectively. The pulsed laser beam is indicated by green color. US ranging deviations vs. surface angle at different distances in (c) X and (d) Y axis, respectively. OA ranging deviations vs. surface angle at different distances in (e) X and (f) Y axis, respectively.

4.4 Material Sensing Experiments and Results

4.4.1   Data Acquisition and Classification

Both the low- and high-frequency components of the US and OA signals received by the ring PZT transducer are used for material/sub-surface structure (especially the thickness) sensing. Depending on the optical and mechanical properties of the target, the received signals mainly consist of either target-induced OA signal, or target-reflected US signal, or both, which provide distinctive features for target material/structure sensing. The sensing has been performed with the Bag-of-SFA-Symbols (BOSS) classifier [45] [46]. The classifier is trained to identify the different material/structure, where the original data set is randomly divided into the training and testing data with 3:1 ratio without overlapping. The experimental data are transformed into BOSS histograms, serving as feature set for sensing. After 50 random trials, the BOSS classifier gives the confusion matrix to show the averaged sensing accuracy.

4.4.2   Material / Thickness Differentiation

To characterize the material/structure sensing performance of the new DMDSM sensor, normal daily targets, including 1.6-mm-thick acrylic, aluminum block, thick paper from white-color milk box, black rubber, steel, and aluminum sheets with different thickness are used as targets (Fig. 4.2) for material/sub-surface structure (thickness) differentiation. The acrylic and paper were coated with black ink to avoid the confusions with the challenging targets in the next section. The captured waveforms, including the US and/or OA signals, are similar as that in Fig. 4.5(b), which carry the distinctive

features of the targets. The representative DMDSM acoustic spectra are shown in Figs. 4.9 and 4.10. The confusion matrices given by BOSS classifier (Fig. 4.11) indicate ≥97% overall accuracy of the material differentiation and 100% overall accuracy of the thickness classification.

(a)   (b)   (c)

(d)   (e)
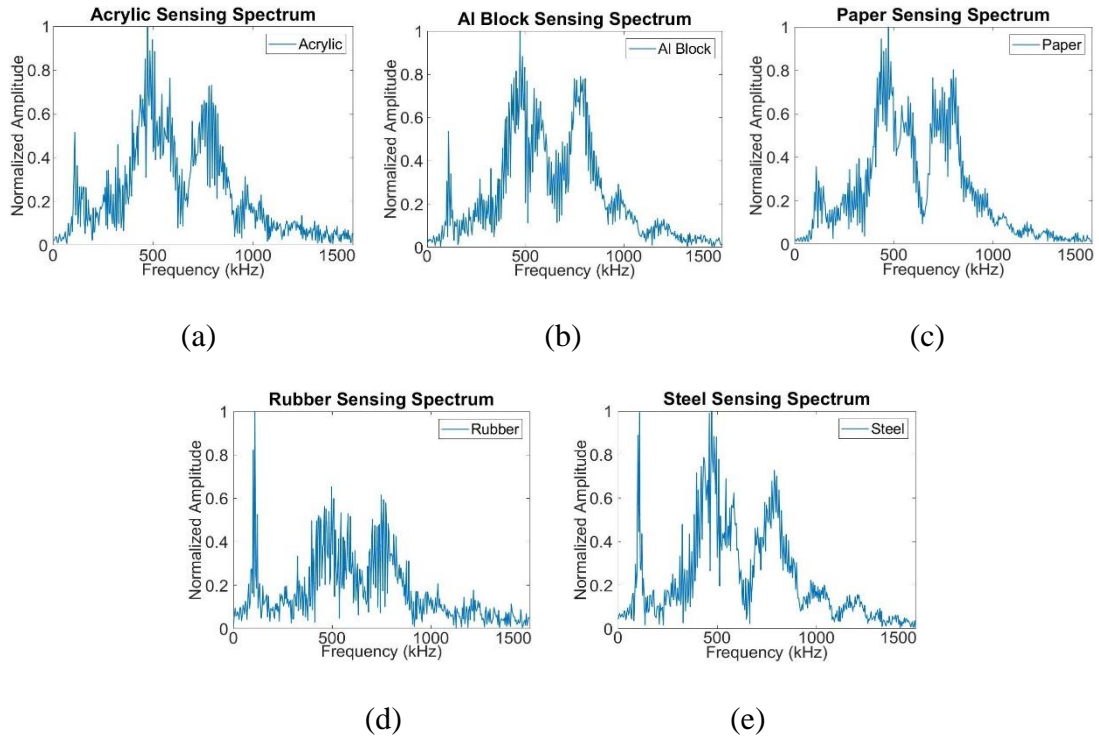
Fig. 4. 9. Representative DMDSM acoustic spectra from five normal daily targets of (a) acrylic, (b) aluminum block, (c) paper, (d) rubber, and (e) steel.

(a)   (b)   (c)   (d)

49

(e)   (f)   (g)
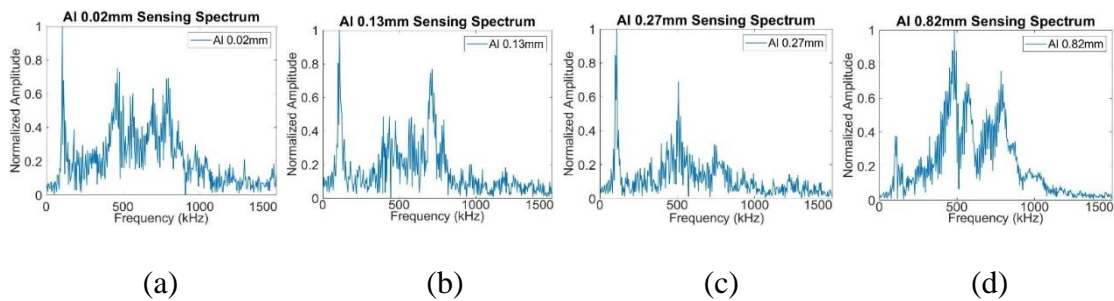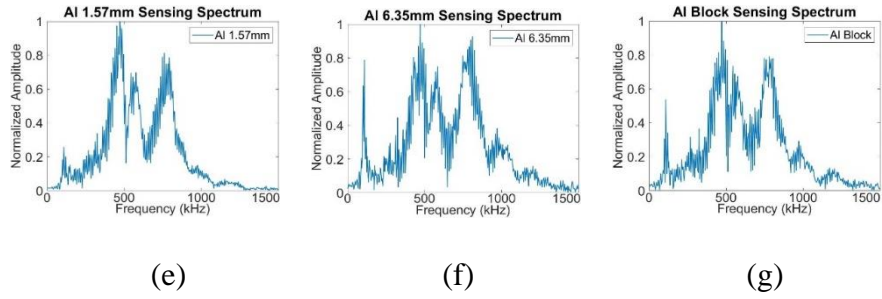
Fig. 4. 10. Representative DMDSM acoustic spectra from aluminum sheets with different thickness.

(a)   (b)
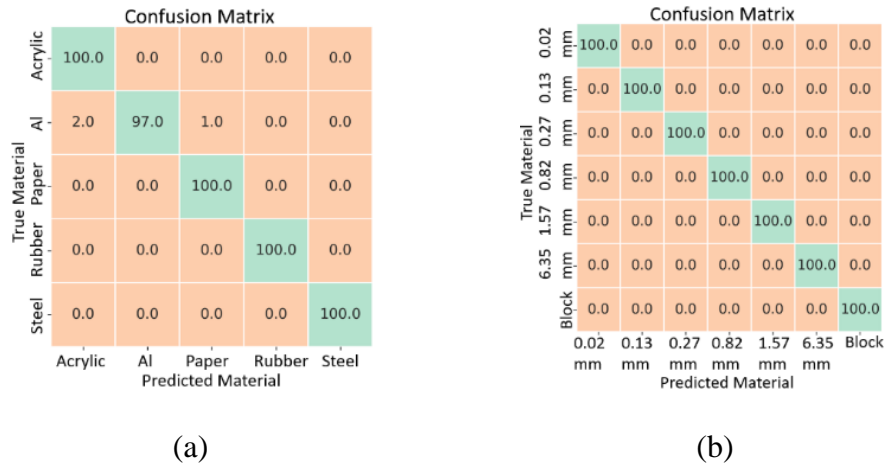
Fig. 4. 11. BOSS classifier averaged confusion matrix of (a) five normal daily targets and (b) aluminum sheets with different thickness.

4.4.3   Differentiation of Challenging Targets

To further investigate the sensing capabilities of the new DMDSM sensor, eight OACTs are tested (Fig. 4.12), including four optically-transparent targets of glass, acrylic, PET (polyethylene terephthalate), PDMS (polydimethylsiloxane) (Figs. 4.12(a)-(d)) with low optoacoustic generation efficiency, and four dark thin/porous targets of

50

fabric, foam, thin paper, 95%-transmittance window tint film (Figs. 4.12(e)-(h)) with weak acoustic reflection. To compensate the target thickness difference, the height of the target is adjusted until the target top is at the focus of the parabolic mirror (Fig. 4.2). BOSS classifier gives the confusion matrix showing a 100% overall accuracy for all the targets (Fig. 4.12(i)).

(a)

(b)

(c)

(d)

(e)

(f)

(g) (h)

Confusion Matrix

	Acrylic	Fabric	Foam	Glass	PDMS	PET	Paper	Tint
Acrylic	100.0	0.0	0.0	0.0	0.0	0.0	0.0	0.0
Fabric	0.0	100.0	0.0	0.0	0.0	0.0	0.0	0.0
Foam	0.0	0.0	100.0	0.0	0.0	0.0	0.0	0.0
Glass	0.0	0.0	0.0	100.0	0.0	0.0	0.0	0.0
PDMS	0.0	0.0	0.0	0.0	100.0	0.0	0.0	0.0
PET	0.0	0.0	0.0	0.0	0.0	100.0	0.0	0.0
Paper	0.0	0.0	0.0	0.0	0.0	0.0	100.0	0.0
Tint	0.0	0.0	0.0	0.0	0.0	0.0	0.0	100.0

True Material / Predicted Material
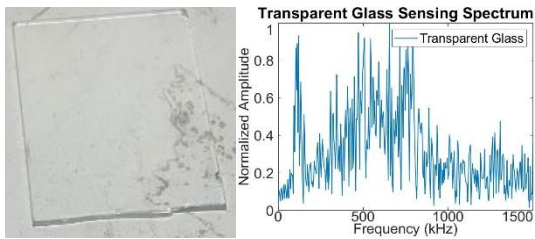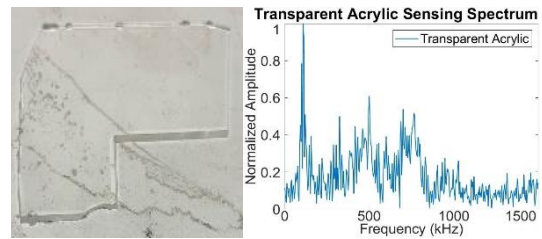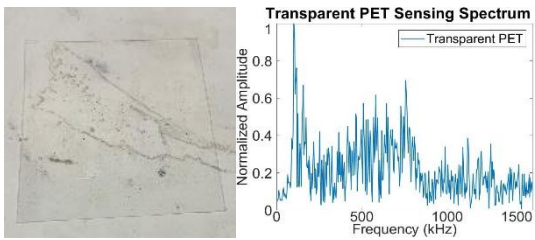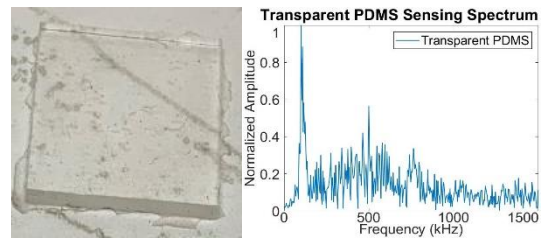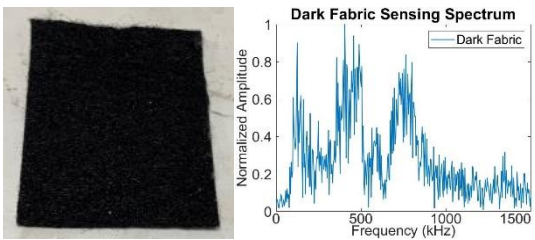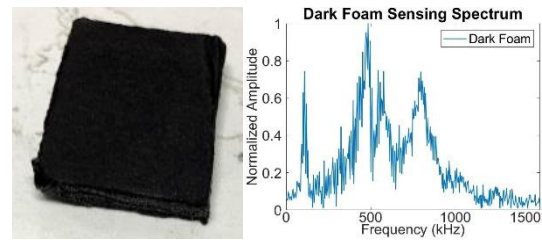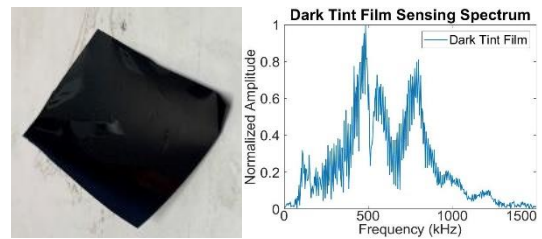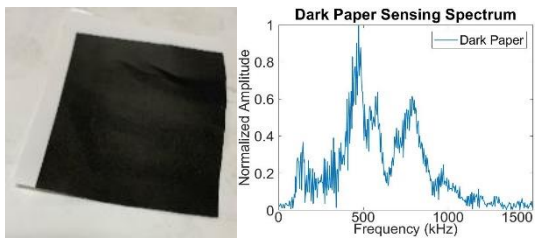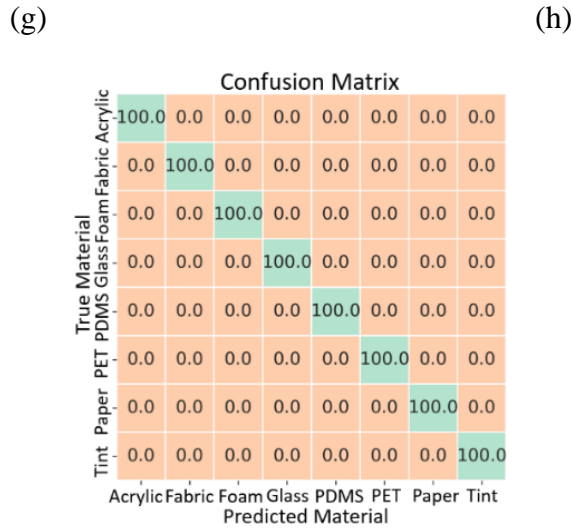
(i)

Fig. 4. 12. Photographs and representative DMDSM acoustic spectra of (a-d) optically-transparent targets of glass, acrylic, PET, PDMS with thicknesses around 1.0 mm, 1.6 mm, 0.11 mm, and 1.5 mm, respectively, and (e-h) dark thin/porous targets of fabric, foam, paper, window tint film with thicknesses around 2 mm, 8 mm, 0.1 mm, 0.06 mm, respectively. (i) BOSS classifier averaged confusion matrix of the eight OACTs.

4.5 Object Contour Scanning and Reconstruction

Based on the previously-characterized ranging and sensing performances, an automatic object scanning system has been built with the new DMDSM sensor to enable the wide deployment of the new sensor and establish an object/material database of common household items. The scanning system is constructed by a refitted 3D printer (Anycubic™ Chiron) with a motorized turntable (TBVECHI™ HT03RA100) mounted on its printing stage (Fig. 4.13(a)) [29]. The nozzle of the 3D printer is replaced by the

DMDSM sensor to perform 3D translation, and the object of interest is supported and rotated by the turntable for a full-body scan. The scanning system sensor controller (STM32™ NUCLEO-H743ZI) and actuator controller (Atmel™ ATmega2560) communicate with PC through the serial port to report the signals from the DMDSM sensor and adjust the nozzle position and turntable rotation. The scanning system is able to automatically scan and collect data for common household items with a size profile of less than $27 \times 27 \times 43$ cm^3. Before the deployment, the parameters of the installed scanning system and the DMDSM sensor are calibrated to assure high scanning accuracy. After the calibration, six common household objects, including steel & glass bottles, plastic & hard-paper boxes, an apple, and a piece of black foam, have been scanned. Their contours have been successfully reconstructed (Figs. 4.13(b)-(g)) based on the measured time-of-flight (ToF) of the US and/or OA signals and the actuator positional and angular readings from the 3D printer and turntable.
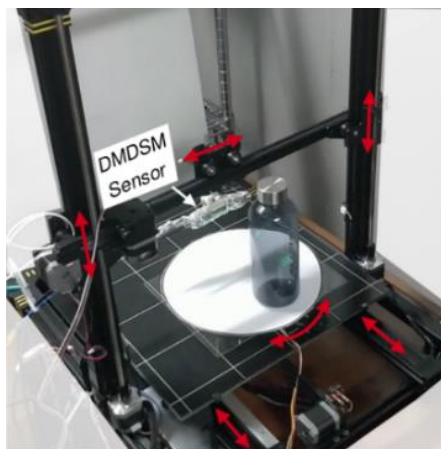
(a)
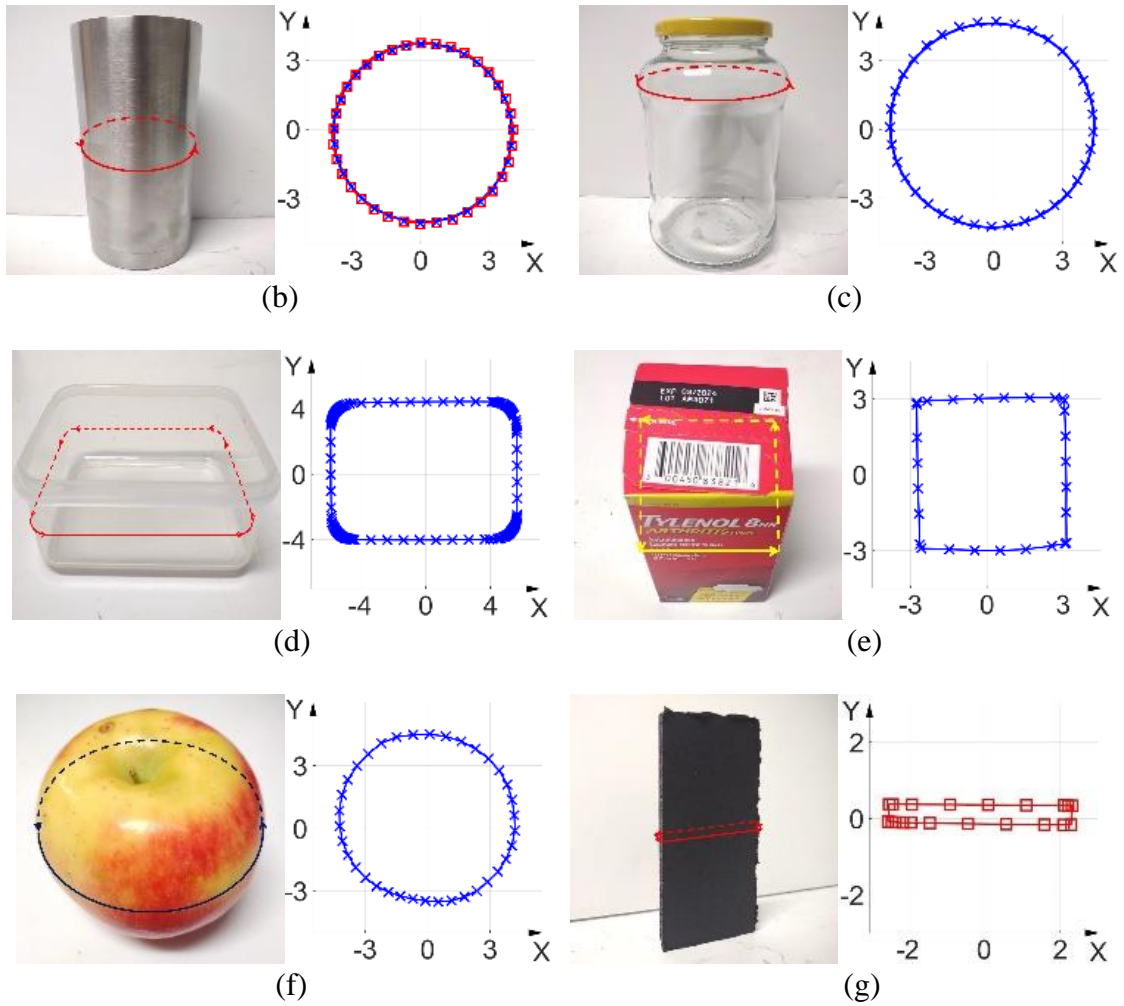
Fig. 4. 13. (a) A photograph of the scanning system with a bottle on the turntable. The freedoms of translation and rotation are indicated by the red lines with arrows. Photographs and the reconstructed contours of the six common household objects: (b) steel bottle (both US and OA), (c) glass bottle (US only), (d) plastic box (US only), (e) hard paper box (US only), (f) apple (US only), and (g) black foam (OA only). In photos, the scanning paths are indicated by lines with arrows. The contours are reconstructed based on the scanning data points, where the US and OA modalities are indicated by

54

blue-line '×' and red-line '□', respectively. The unit of XY coordinates is centimeter. Reprinted with permission from [29] © IEEE.

4.6 Summary

In summary, the G2 DMDSM sensor has been developed for near-distance ranging and material/structure sensing to provide perception assistance to robotic grasping. Both ranging and material/structure sensing can be achieved with the single wideband ultrasound transmitter and receiver, and both US and OA signals collection can be triggered by the same laser pulse, which makes the system construction and operation simple and straightforward. The prototype of the G2 DMDSM sensor has been fabricated and characterized. Moreover, an object scanning system with the new sensor has been built to scan common household objects with different shapes and materials. The experimental results show that the G2 DMDSM sensor has achieved satisfying ranging and sensing performances with simpler system configuration, which make it more capable and practical to assist the robotic grasping of unknown objects.

5. PERFORMANCE IMPROVEMENT OF DMDSM SENSOR

5.1 Introduction

Although the G2 DMDSM sensor has a simplified configuration, it is limited to single-point detection by the bulky parabolic mirror. As Fig. 5.1(a), the G2 sensor relies on the parabolic mirror to focus the planar laser and ultrasound beams. The relatively high numerical aperture (NA) of the parabolic mirror limits the working distance and makes it difficult to steer the laser and ultrasound beams over the target surface. Therefore, the G2 DMDSM sensor is difficult for fast object mapping and imaging, which otherwise would be very useful to perceive the detailed features of the object for facilitating the grasping.

To address this issue, a new (G3) DMDSM sensor is developed, where the US/OA transceiver is updated from the previous flat design to a self-focused one (Fig. 5.1(b)) so that the bulky parabolic mirror is not necessary. The relatively lower NA of the self-focused transceiver has improved the working distance, and the laser and ultrasound beams can be steered over the target by the flat 2D scanning mirror. Therefore, the G3 DMDSM sensor has expanded the sensing capabilities from single-point detection to fast areal mapping and imaging. In this chapter, the design and fabrication of the prototype G3 DMDSM sensor are demonstrated. Its ranging performances are also characterized and compared with those of the previous versions. Thin wire targets made of same or different materials at different locations are successfully scanned and imaged. The experimental results show that the G3 DMDSM

sensor provides improved performances of larger working distance as well as the fast mapping and imaging capabilities to enhance robotic grasping.
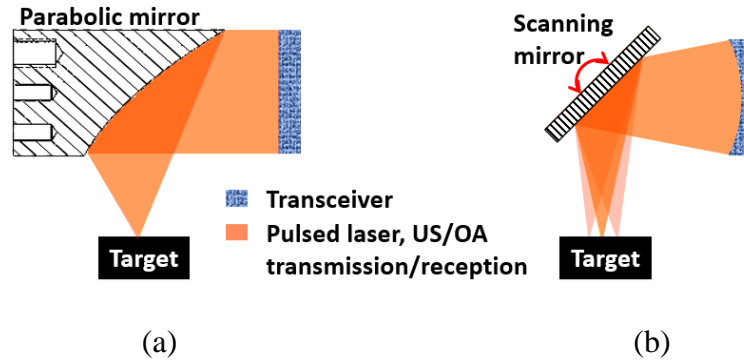
Fig. 5. 1. Digrams showing the different designs of (a) G2 and (b) G3 DMDSM sensors.

5.2 Design, Construction, and Testing

Fig. 5.2 illustrates the schematic design of the G3 DMDSM sensor. It consists of a focused US/OA transceiver in a co-centered and co-axial configuration. For US ranging and sensing, the (green) pulsed laser beam from the light source is expanded by two lenses to illuminate the spherically-shaped black tape layer. Upon its absorption, the pulsed laser beam generates a heat pulse and subsequent thermal expansion and contraction in the black tape layer, which transmit a focused (by the spherical shape) ultrasound pulse to the target (after being reflected by the flat scanning mirror). The echo signals travelling back along the reverse path are collected by the ring transducer with a focusing acoustic lens attached in front. For OA ranging and sensing, the inner part of the pulsed laser beam is focused by a small lens and passes through the center hole of the black tape layer onto the target (after being reflected by the flat scanning mirror). The excited optoacoustic signal travels along the reverse path and is collected by the same

ring transducer. One laser pulse triggers the collection of both US and OA signals without mixing with each other [28]. This is because the US signals arrive at the transducer after a round trip, while the OA signal only goes through a single trip, which results in a large difference in their time delays. With a 2D scanning mirror, the focused laser and US/OA beams can be reflected and scanned over the target with customized patterns. It is worth mentioning that the mirror-transceiver distance (d_1) can be adjusted to enable the ranging even when the sensor package (as the gray dashed line in Fig. 5.2) contacts the target.
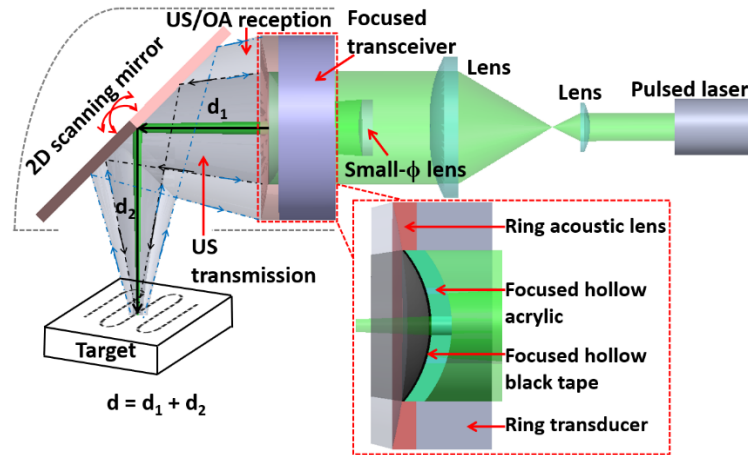
Fig. 5. 2. Schematic design of the G3 DMDSM sensor with a zoom-in cross-section view of the redesigned focused US/OA transceiver. d_1 and d_2 is the distance from the mirror reflection center point to the transceiver and the scanning point on target, respectively.

Fig. 5.3 shows the fabricated prototype of the G3 DMDSM sensor (weight ≈ 13.7 grams), which consists of a 3D-printed housing (length ~ 27 mm, ϕ ~ 26 mm), a small-ϕ glass lens (Fig. 5.3(c)), and a focused US/OA transceiver. The focused US transmitter

consists of a molded optically-transparent acrylic plate (1.6-mm thick) as the supporting substrate and a black vinyl electrical tape (0.1-mm thick) as the laser-absorption layer (Figs. 5.3(b) and 5.3(c)). Both acrylic and vinyl have low Young's modulus (several GPa) and high internal damping, which allows effective generation of wideband low-MHz ultrasound signals. The acrylic plate and black vinyl tape are molded by one pair of matched plano-convex and concave glass lenses with a diameter of 12 mm and spherical radius of 9.42 mm, which provides an acoustic numerical aperture (NA) around 0.64. A center hole with a 1.5-mm diameter is drilled on the acrylic plate and black vinyl tape to allow the pulsed laser to pass through, which is focused by the small-ϕ (6-mm) glass lens in advance (Fig. 5.2) . To better collect the US echoes and OA signals from the target, a ring-shaped epoxy acoustic lens (with a focal length around 4 cm) is added to the front of the flat ring-PZT (lead zirconate titanate) transducer (with a 19.6-mm outer diameter and 12-mm inner diameter). The epoxy lens also serves as the acoustic impedance matching layer to improve the acoustic coupling efficiency between air and PZT. In addition, soft PZT composite is used to fabricate the ring transducer, which provides a higher electromechanical coupling factor and wider acoustic bandwidth than the hard PZT previously used in the G2 sensor.
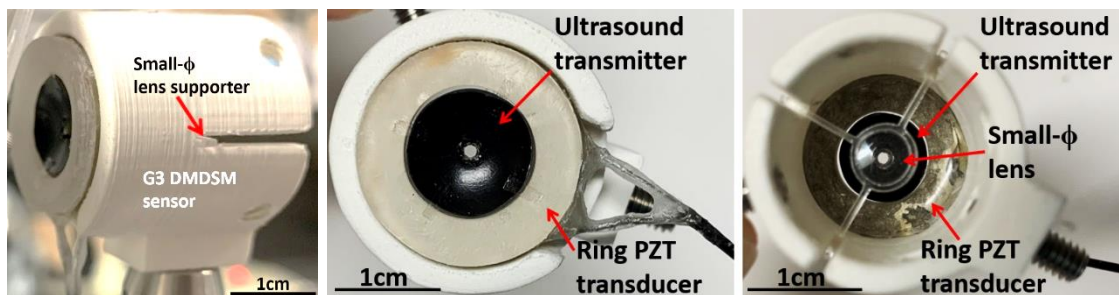
(a)   (b)   (c)

Fig. 5. 3. Photographs of the (a) side, (b) front, and (c) back view of the fabricated prototype of the G3 DMDSM sensor. The focused ultrasound transmitter is housed inside the inner hole of the ring PZT transducer.

Fig. 5.4(a) shows the setup for characterizing the US/OA performances of the G3 DMDSM sensor. A Q-switched 532nm Nd:YAG pulsed laser is used as the light source. It has a pulse repetition rate (PRR) of 10 Hz, a pulse duration of 8 ns, and an average pulse energy around 2.5 mJ/pulse. One laser pulse initiates simultaneous US and OA data acquisition. The US and OA signals are received by the focused ring transducer, amplified by a preamplifier, and then recorded by an oscilloscope. A photo detector is used to detect the laser pulse and generate a trigger signal to synchronize the data acquisition. Fig. 5.4(b) shows a representative US/OA signal from an aluminum block as the target. The time delays of the 1st OA signal, the US signal, and the 2nd OA signal (the reflection of the 1st OA signal after a round trip) are around 75 µs, 156 µs, and 221 µs, respectively.

To characterize the reception bandwidth of the focused ring transducer, a 0.4-mm pencil lead is used as the target. The distance (d) between the US/OA transceiver and pencil lead is around 3 cm. Upon illumination of focused laser pulses, the pencil lead generates short-pulse OA signals with a wide bandwidth. A representative OA waveform and its frequency spectrum received by the transducer are shown in Figs. 5.4(c) and 5.4(d), respectively, which indicates a wide bandwidth consisting of four frequency bands centered around four resonance frequencies of 52 kHz, 412 kHz, 748 kHz, and

1164 kHz. Next, the collective acoustic bandwidth of the US transceiver is characterized, which is determined by both the transmission from the black tape and also the reception of the transducer. A piece of flat 1-mm-thick glass slide serves as the target. Because it has very low optical absorption, the generation of OA signals is minimized. The distance (d) between the US/OA transceiver and glass slide is around 3 cm. A representative US waveform and its frequency spectrum received by the transducer are shown in Figs. 5.4(e) and 5.4(f), respectively, which indicates a narrower collective bandwidth consisting of three frequency bands centered around three resonance frequencies around 56 kHz, 272 kHz, and 428 kHz, which is due to the lower-frequency response of the US transmitter consisting of the molded acrylic plate and black tape.
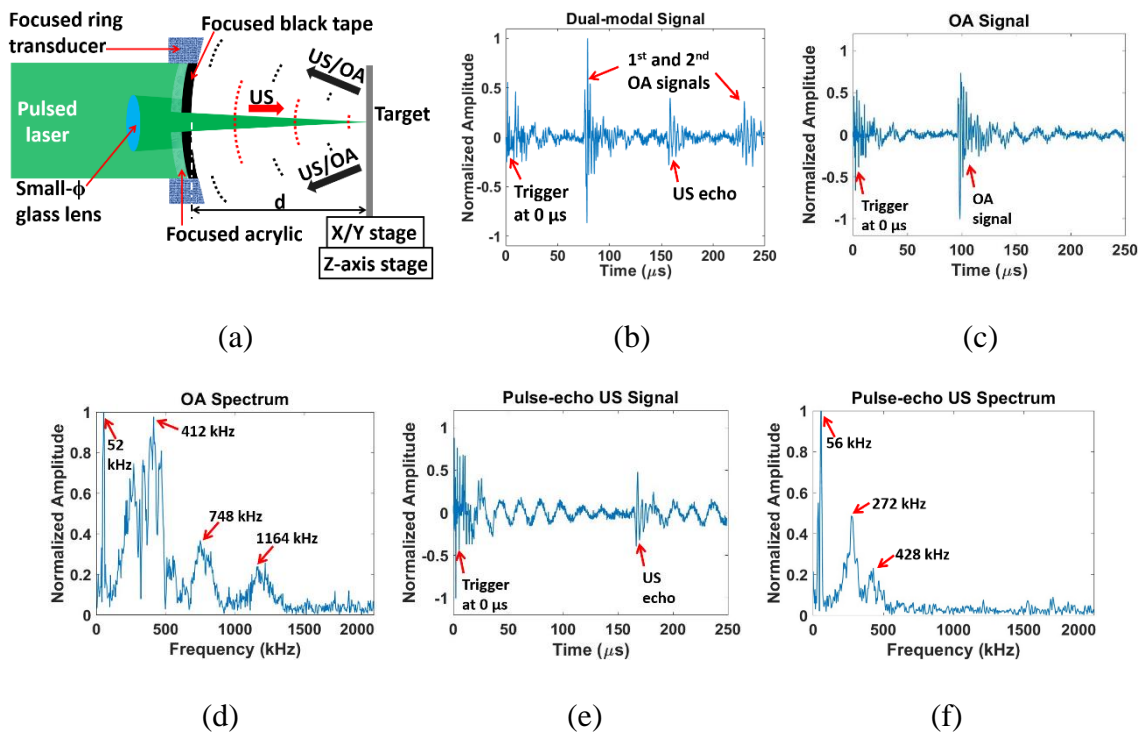
Fig. 5. 4. (a) Diagram of the setup to characterize the G3 DMDSM sensor. (b) Representative waveform of the received US and OA signals from an aluminum block

61

through air. Representative (c) OA waveform and (d) frequency spectrum from a 0.4-mm-ϕ pencil lead. Representative (e) US waveform and (f) frequency spectrum from a 1-mm-thick flat glass slide.

5.3 Ranging Experiments and Results

5.3.1 US Ranging

The same testing setup (Fig. 5.4(a)) is used to characterize the US and OA ranging performances of the G3 DMDSM sensor. For US ranging, a piece of 1-mm-thick flat glass slide is used as the target. The distance (d) between the US/OA transceiver and the glass slide is increased from 4.0 mm to 80.0 mm (the maximum distance range of the X/Y stage) with an increment of 2.0 mm. The measured (delay-calculated) distance vs. the actual distance (d) and their deviations are shown in Figs. 5.5(a) and 5.5(b), respectively. With a second-order polynomial fitting and calibration, the deviation is less than 0.24 mm where d increases from 4.0 mm to 78.0 mm. The ultrasound echo signal becomes undetectable at $d < 4.0$ mm, due to the limited reception angle of the focused ring transducer. Without the X/Y stage, the maximal ranging distance of pulse-echo ultrasound modality is roughly measured as ~156 mm (Fig. 5.5(c)). The same setup is used to quantify the lateral resolution of the US ranging, except that the glass slide target is replaced by an optically-transparent optical fiber with a diameter of 1.0 mm. After repeating the lateral scans at different distance (d) from 26.0 mm to 36.0 mm, the ultrasound lateral resolution is determined by the minimal acoustic focal diameter (Fig. 5.5(d)), indicating the lateral resolution around 1.04 mm at

the focal length $d = 31.0$ mm. The measured focal zone is around 10.0 mm where d is

from 26.0 mm to 36.0 mm, with maximum ranging deviation around 0.1 mm.
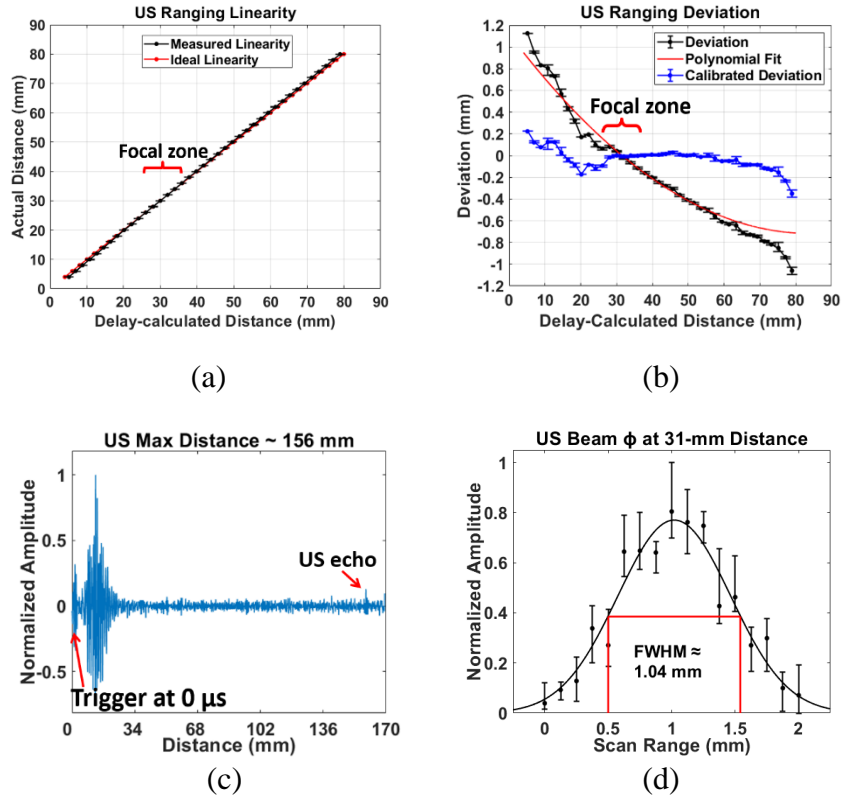
Fig. 5. 5. (a) Comparison between measured (in black) and actual (in red) distances. (b) Deviation of the measured distance from the actual distance. (c) Maximal pulse-echo ultrasound ranging distance ~ 156 mm. (d) US lateral resolution of 1.04 mm determined by the minimal acoustic focal diameter at d = 31 mm.

5.3.2   OA Ranging

The OA ranging performance of the G3 sensor is characterized by using a black-paint-coated box as the target (Fig. 5.4(a)). The distance (d) between the US/OA transceiver and the box is increased from 10.0 mm to 80.0 mm with an increment of 2.0

mm. The measured distance vs. real distance (d) and their deviations are shown in Figs. 5.6(a) and 5.6(b), respectively. With the polynomial fitting and calibration, the deviation is less than 0.2 mm where d is from 10.0 mm to 80.0 mm. OA signal becomes undetectable at distance < 10.0 mm, due to the limited reception angle of the focused ring transducer. After removing the X/Y stage, the maximal OA ranging distance is roughly measured as ~161 mm (Fig. 5.6(c)). The same setup is used to quantify the optoacoustic lateral resolution, except that the black box is replaced by a 0.4-mm-ϕ pencil lead. The pencil lead is laterally scanned at different distance (d) from 16.0 mm to 80.0 mm. The optoacoustic lateral resolution is determined by the minimal laser focal diameter (Fig. 5.6(d)), indicating a lateral resolution ~0.29 mm at the focal length ($d = 51.0$ mm). The lateral resolution of OA is much better than that of US (~1.04 mm), mainly because of a much smaller laser focal spot. The measured OA focal zone is around 50.0 mm where d is from 26.0 mm to 76.0 mm, with ranging deviation less than 0.13 mm. The focal zone of OA is much larger than that of US (~10 mm), mainly because of the smaller laser NA than US. Nevertheless, the two focal zones are overlapped at distance (d) from 26.0 mm to 36.0 mm, providing a 10-mm shared working range with optimal lateral resolutions of both modalities.
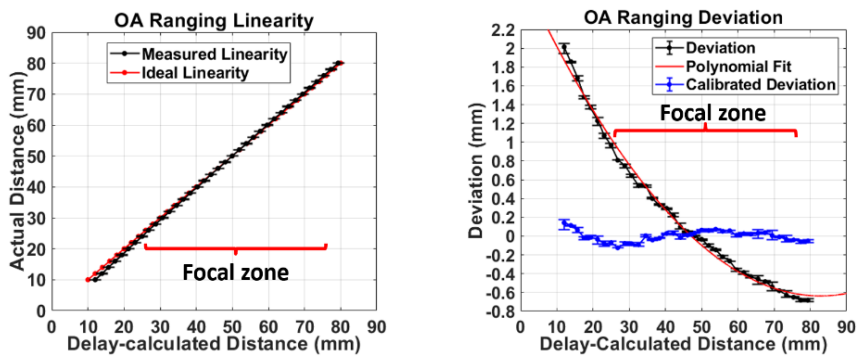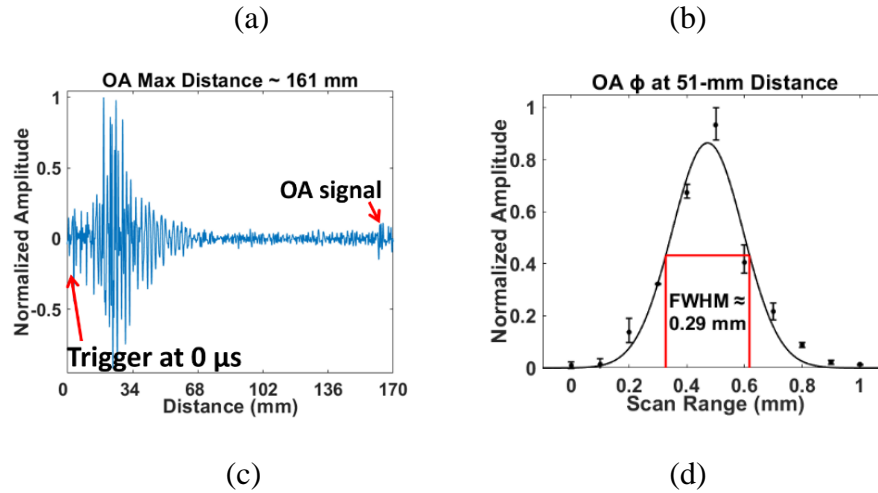
Fig. 5. 6. (a) Comparison between the measured (in black) and the real (in red) distances. (b) Deviation of the measured distance from the real distance. (c) Maximal OA ranging distance ~ 161 mm. (d) OA lateral resolution of 0.29 μm determined by the minimal OA focal diameter at d = 51.0 mm.

Table 5.1 lists the ranging performances of the G1, G2, G3 DMDSM sensors, with improvements marked in green. For both US and OA ranging of G3 sensor, the lateral resolution is deteriorated, but the focal zone and working distance are greatly enlarged, which provide a much larger overlapped range of US and OA modalities. This is because of the smaller NA of the focused transceiver than that of the parabolic mirror. Also, with the assistance of curve fitting and calibration, the ranging deviation of the G3 sensor is greatly reduced.

Table 5. 1. Comparison of the performance of the DMDSM sensors.

Ranging Performances	G1 Sensor [25]	G2 Sensor [28]	G3 Sensor
US DOF (mm)	2.0	3.0	**10**
US Max Deviation within DOF (mm)	0.24	0.29	**0.1**
US Lateral Resolution (mm)	1.04	0.60	1.04
US Working Distance (mm)	0-6.5	0.5-11	**4-156**
OA DOF (mm)	1.0	1.0	**50**
OA Max Deviation within DOF (mm)	0.12	0.20	**0.13**
OA Lateral Resolution (µm)	95.0	61.7	290
OA Working Distance (mm)	5-8	5-7	**10-161**
Overlap of US/OA DOF (mm)	0	1.0	**10**

5.4 Imaging Experiments

5.4.1   2D Scanning Mirror

To demonstrate the scanning and imaging with the G3 sensor, a two-axis flat scanning mirror is designed and fabricated to enable the steering of the co-centered and co-axial dual-modal beams. The scanning mirror consists of a reflective mirror plate mounted on a fixed-frame with four side torsion hinges and actuated by inductor coils to enable fully operation without any mechanical joints [47]. A piece of 20 mm × 20 mm double-side-polished silicon wafer with 200-µm thickness is used as the mirror plate for

optical and acoustic reflection. Limited by the low 10-Hz PRR of the pulse laser, the scanning mirror is driven by two DC bias voltages under the quasistatic condition. The DC bias is applied to the inductor coils to steer the mirror plate step-by-step along the two axes. In the imaging experiments, the two axes are tilted by around $\pm 16º$ under ± 3 V DC bias, and $\pm 4º$ under 0 - 2 V DC bias, respectively. The voltage step is 0.2 V for both axes, and the imaging area is around 8 mm (pan) $\times$ 2 mm (tilt).

5.4.2   2D Imaging of Different Thin Targets

An optically-transparent optical fiber, a black coaxial cable, and a black cotton wire placed at similar height are used as targets (Fig. 5.7(a)). Their diameters are all around 1 mm, and the lateral spacing is 2 mm, making the air gap between two adjacent targets around 1 mm (Fig. 5.7(a)). For each data, the US/OA signals are averaged by 128/16 times, respectively to improve the signal-to-noise ratio (SNR). The 2D US and OA images (Figs. 5.7(b) and 5.7(c)) are reconstructed based on the normalized signal amplitude at each location (pixel), which is indicated by the color bar. In the US image, the optical fiber appears wider than the black coaxial cable, and the soft cotton wire is hardly detected. This is because of their different acoustic impedance and thus different acoustic reflectivity (optical fiber > cable plastic jacket >> cotton wire). In the OA image, the black coaxial cable and black cotton wire are resolved clearly, and the transparent optical fiber could not be detected, due to their different optical absorptivity (cable plastic jacket $\approx$ cotton wire >> optical fiber). There exist some variations in the

signal strength across the image, which would be due to the slight height variations caused by different topographic features of the targets.
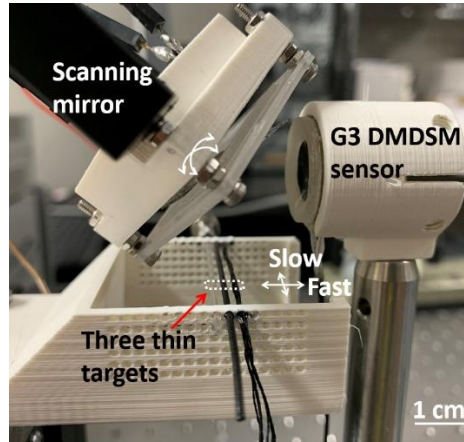
(a)
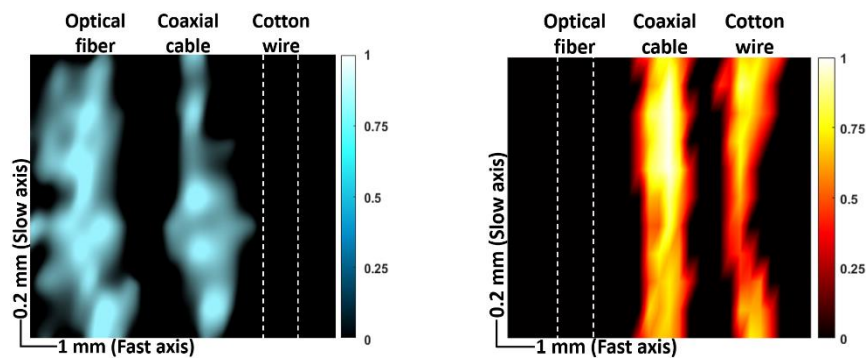
(b)   (c)

Fig. 5. 7. (a) Photo of the imaging setup with the G3 sensor, scanning mirror, and three different thin targets placed at similar height. The scanning area is marked by the white dashed region. The reconstructed 2D (b) US and (c) OA images of the three targets. The color bar represents the normalized signal amplitude.

5.4.3 3D Imaging of Thin Targets at Different Heights

The same setup (Fig. 5.7(a)) is used to further demonstrate the 3D imaging capability of the G3 sensor, except using three 1-mm-ϕ black coaxial cables at different heights as targets (Fig. 5.8(a)). The horizontal and vertical spacing is 2 mm and 4 mm, respectively, making the air gap between two adjacent cables around 1 mm (horizontal) and 3 mm (vertical). The same voltage range and step size are used to drive the scanning mirror, providing the same scanning area, as marked by the white-dashed region, with around 13 mm range in height. The 3D US and OA images (Fig. 5.8(b) and 5.8(c)) are reconstructed by stacking the B-scan images acquired at the 11 tilt steps. The normalized signal amplitude at each location (pixel) is indicated by the color bar. Each B-scan image is reconstructed by the 31 A-scan signals during one scan in pan. In both US and OA images, the three coaxial cables are resolved clearly.

(a)   (b)   (c)
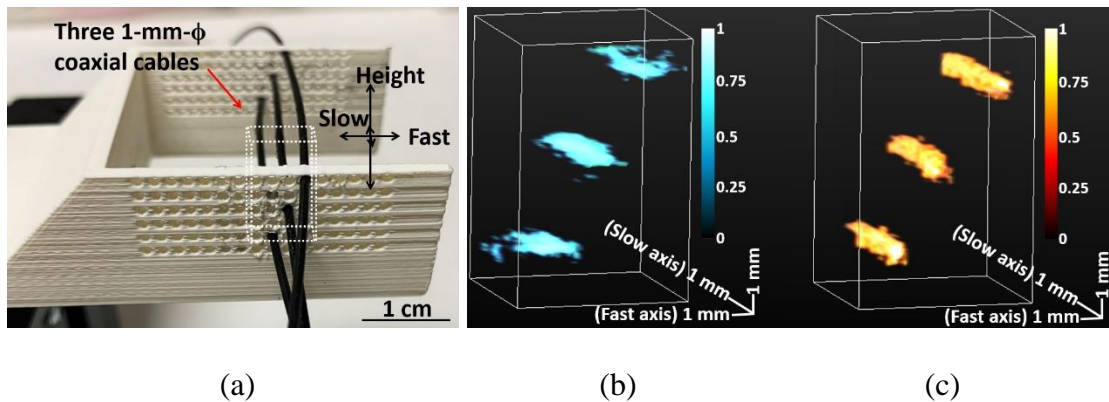
Fig. 5. 8. (a) Photo of the 3D imaging targets at different heights. The reconstructed 3D (b) US and (c) OA images of the three black coaxial cables. The color bar represents the normalized signal amplitude.

5.5 Summary

In summary, the new (G3) DMDSM sensor with improved performances have been demonstrated. Different from the previous sensors (Chapter 3 and 4) which rely on a bulky parabolic mirror for focusing, a self-focused wideband ultrasound transceiver is designed to generate focused laser and ultrasound beams without the parabolic mirror. As a result, the laser and ultrasound beams can be easily steered by a flat 2D scanning mirror for not only single-point ranging and detection but also areal mapping or imaging. Although the US/OA lateral resolutions are slightly deteriorated by the lower NA of focusing, they are still good enough for most grasping applications. On the other hand, the effective work distance has been significantly enlarged and two focal zones better overlap with each other. These features could better facilitate the grasping of targets with more complex shapes or surface features.

6. OPTICALLY-TRANSPARENT FOCUSED (OTF) TRANSDUCERS*

6.1 Introduction

Although the focused ring-shaped PZT transducer works well as a prototype in the G3 DMDSM sensor, it is difficult to be miniaturized while maintaining the detection sensitivity for a few reasons. First, a large hole has to be drilled at the center to integrate with the ultrasound transmitter in a co-centered and co-axial construction, which provides low acoustic reception efficiency, low NA, and thus relatively big acoustic focal spot. Second, the large center hole makes the total diameter even larger to maintain the acoustic detection sensitivity. Third, its construction is relatively complex, which needs the matching layer for acoustic impedance matching and focusing, as well as the backing layer to improve the acoustic reception bandwidth. At last, the acoustic lens is homemade with optical epoxy, whose spherical surface has a relatively low quality.

To further miniaturize the sensor to be mounted on a robotic finger for grasping, the optically-transparent focused (OTF) transducer could be a good choice with several unique advantages. First, the OTF transducer is optically transparent, so the center hole is not necessary to be drilled to pass the light through. Second, the complete transducer substrate provides a higher acoustic reception efficiency, and thus a higher NA and smaller acoustic focal spot. Therefore, the OTF transducers are helpful to miniaturize the DMDSM sensor while maintaining the sensitivity. Among the piezoelectric materials, polyvinylidene fluoride (PVDF) and its co-polymer are suitable for the fabrication of the OTF transducer, because of several advantages. First, they have adequate optical

transmittance. Second, they have good mechanical flexibility which can be directly laminated onto the spherical surface to achieve a high-NA and high-quality focusing. Another benefit of the mechanical flexibility is the wideband acoustic response, which makes the backing layer unnecessary. Third, their acoustic impedances are relatively low and close to that of water, so the impedance matching layer is not necessary.

In this chapter, two OTF ultrasound transducers are demonstrated, which are made of PVDF and its co-polymer. The OTF PVDF transducer is discussed first (Fig. 6.1), which is briefly compared with other OTF transducers in Table 6.1. An optoacoustic imaging (OAI) setup has been built with the OTF PVDF transducer and experiments have been conducted on a phantom target of a twisted black wire in water and chicken breast tissue, as well as an in-vivo target of the cross-section of a mouse tail. The imaging results show that high acoustic resolution and sensitivity can be achieved with a simple and compact setup.

72
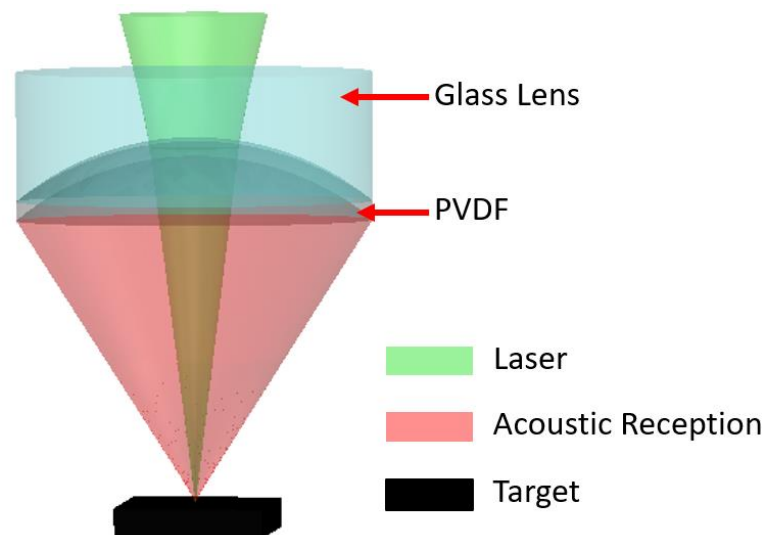
Fig. 6. 1. Simplified diagrams of the OTF PVDF transducer. Reprinted with permission from [31] © Optica Publishing Group.

Table 6. 1. Acoustic performance of comparable transducers. Reprinted with permission from [31] © Optica Publishing Group.

Transducer	Commercial Flat +Acoustic Lens		Homemade Focused with Acoustic Lens		Homemade Focused Hollow / Ring [48]	Previously Published [30]	OTF PVDF
	Ref [49]	Ref [50]	Ref [51]	Ref [52]			
OA Imaging Signal-to-Noise Ratio (dB)	30	14 (at 4.8mm depth)	NA	41	25.2	15.2	28.9
Frequency (MHz) / Bandwidth (MHz)	50 / 35	50 / NA	11.2 / 2.6	7.5, 31.5 / 13, 8	35 / 25	24 / 26	36 / 44
Pulse-echo Ultrasound Lateral (μm) / Axial Resolutions (μm)	45 / NA	44 / NA	141 / 148	102 / 81	80 / NA	130 / 32.5	37.8 / 17.7

Next, the second OTF transducer (Fig. 6.2) is demonstrated, which is made of P(VDF-TrFE)) (poly(vinylidene fluoride-co-trifluoroethylene), also called PVDF co-polymer). Table 6.2 roughly compares the parameters of PVDF and P(VDF-TrFE) that are closely related to the transducer performances. It can be concluded that P(VDF-TrFE) is generally a better material than PVDF, because of slightly higher piezoelectric coefficient, higher electromechanical coupling factor, and lower dielectric loss. Unfortunately, P(VDF-TrFE) has a much lower mechanical stretchability and flexibility than PVDF, so the OTF P(VDF-TrFE) transducer cannot be fabricated with the previous stretch-molding and transfer-bonding methods. Therefore, a new fabrication process based on pre-cutting and direct-lamination is investigated, which eliminates the need of

stretch-molding and therefore is compatible even with non-stretchable piezoelectric films, such as P(VDF-TrFE). With fewer steps, it is also possible to scale up for mass fabrication. Based on this approach, the OTF P(VDF-TrFE) transducer has been successfully fabricated and characterized, and an OA imaging setup has been built to carry imaging experiments on different targets. Based on the experimental results, it can be concluded that compared with the previous PVDF transducer, the OTF P(VDF-TrFE) transducer provides a higher sensitivity, a simpler fabrication process, and the feasibility to achieve high NA using more brittle piezoelectric films.
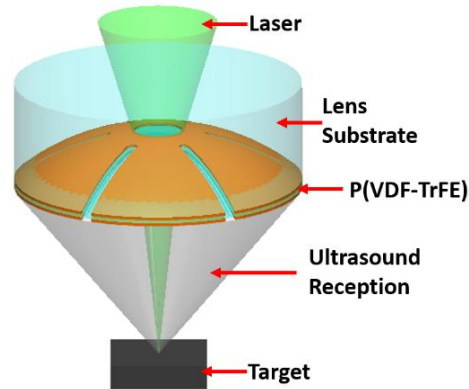
Fig. 6. 2. A schematic diagram of the OTF P(VDF-TrFE) transducer.

Table 6. 2. Relevant material properties of PVDF and P(VDF-TrFE).

	Young's Modulus Y (GPa) [53] [54]	Acoustic Impedance Z (MRayl) [55] [56]	Density ρ (kg/m^3) [55]	Piezoelectric Coefficient d_{33} (pC/N) [57] [58] [59] [60]	Electromechanical coupling factor k_{33} [55] [57]	Dielectric loss tanδ [55]
PVDF	2.7	3.9-4.2	1,780	15-33	0.14-0.2	0.25
P(VDF-TrFE)	1.5	4.5	1,880	17.8-36	0.23-0.3	0.15

74

6.2 OTF PVDF Transducer Design and Construction

Fig. 6.3 shows the schematic of the OTF PVDF transducer. The 9-μm-thick PVDF film is molded onto a concave glass lens with a diameter of 12.0 mm and an acoustic focal length of 9.4 mm, which corresponds to an acoustic NA of 0.64. The central transparent region (with a diameter of 3.0 mm) of the transducer is covered with ITO (indium-tin oxide) electrodes, while the remaining portion has chromium/copper electrodes to reduce the electrical resistance. The optical transmittance of the central transparent region is around 60% at 532 nm [30].
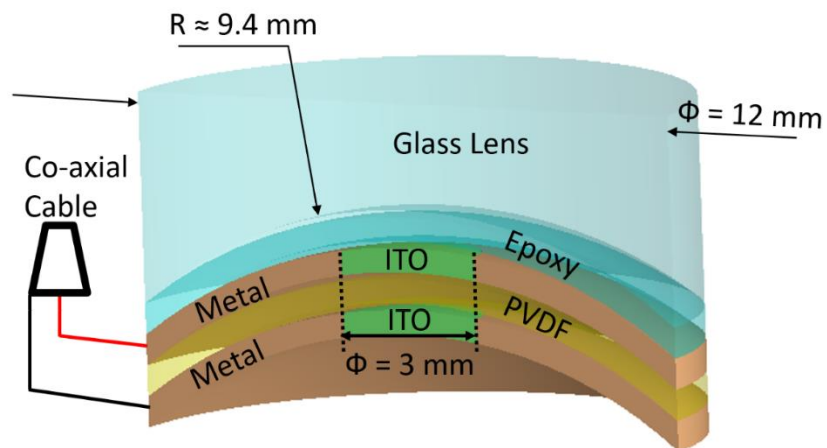
Fig. 6. 3. Schematic design of the OTF PVDF transducer. Reprinted with permission from [31] © Optica Publishing Group.

The detailed fabrication process flow of the OTF PVDF transducer is shown in Fig. 6.4. Firstly, a piece of flat 9-μm-thick PVDF film is trimmed with a film cutter (Fig. 6.4(a)). The PVDF film is compressed and stretched onto a mold consisting of a pair of convex and concave lenses with the same diameter and matched surface radius of

curvature (Fig. 6.4(b)). Secondly, with two shadow masks, an ITO (400 nm thick) layer (Fig. 6.4(c)) and a chrome (15 nm)/ copper (200 nm) layer (Fig. 6.4(d)) are deposited onto the convex side of the stretched PVDF film. Thirdly, the PVDF film is bonded onto the spherical surface of the concave glass (transmittance $\approx$ 90% over 350nm ~ 2000nm [61]) lens with an UV epoxy (transmittance > 90% over 400nm ~ 2000nm [62]) (Fig. 6.4(e)). Lastly, the electrode deposition process is repeated on the exposed side of the PVDF film (Fig. 6.4(f) and 6.4(g)). The surface of the PVDF film outside the transparent window at the center is coated with the chrome/copper layer, which serves as the ground electrode.

(a)   (b)   (c)   (d)

(e)   (f)   (g)
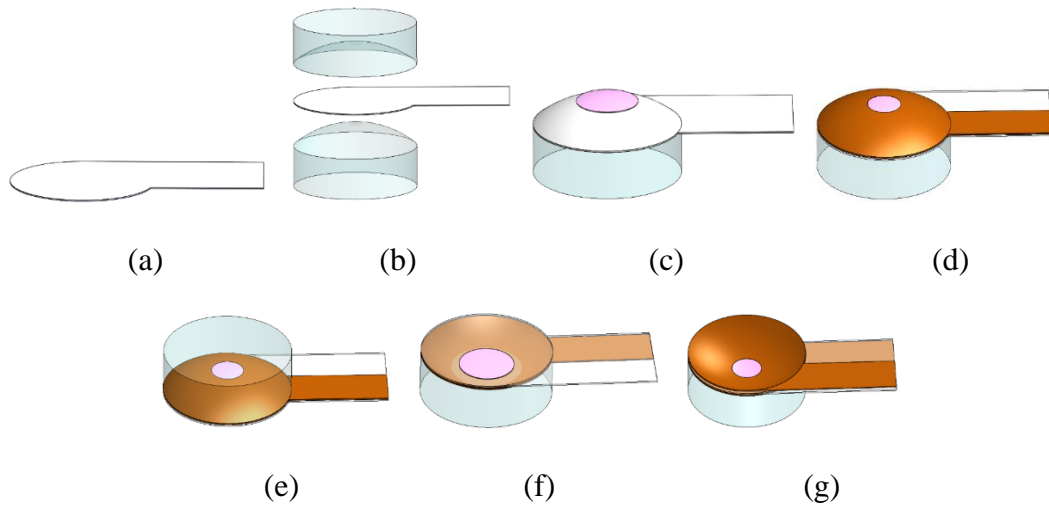
Fig. 6. 4. Schematic diagrams of the stretch-molding and transfer-bonding process of the OTF PVDF transducer: (a-b) Flat PVDF film molded and stretched by lenses. (c-d) ITO and Cr/Cu electrodes deposition on one side. (e) PVDF bonded with concave lens and convex lens released. (f-g) ITO and Cr/Cu electrodes deposition on the other side.

Fig. 6.5 shows a fabricated prototype of the OTF PVDF transducer [63]. A 50-ohm micro co-axial cable is connected to the Cr/Cu electrodes with conductive epoxy. The transducer is mounted onto a home-made plastic fixture to facilitate its attachment onto the microscope objective mount for testing.

(a)   (b)
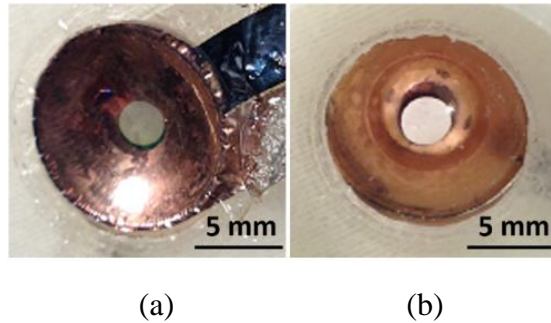
Fig. 6. 5. Photographs of the (a) front side (b) back side of the fabricated focused transparent transducer mounted on a 3D-printed fixture. Reprinted with permission from [63] © SPIE.

6.3 OTF PVDF Transducer Testing and Characterization

A combined US and OA testing setup was built to characterize the acoustic performance of the OTF PVDF transducer by using a razor blade in water (whose sharp tip was coated with black ink) as the target (Fig. 6.6). The front spherical surface of the transducer was immersed in water and the target was placed onto a computer-controlled two-axis motor stage and a manually-adjusted height stage. For OA testing, the light source is a 532-nm pulsed laser (Elforlight, UK) triggered by a function generator with a 1-kHz repetition. The output laser beam was expanded, passed through a beam splitter, reflected by a stationary mirror, and focused by a lens with 10-cm focal length. The

loosely focused laser beam propagated through the transducer and was incident onto the target. A CCD camera was used to monitor the excitation region through the reverse path of the optical illumination. Laser pulse energy after the transparent transducer was measured to be 35 μJ, and the laser spot diameter onto the top surface of the target was around 1 mm, which corresponds to a laser intensity of 4.5 mJ/cm^2, far below the ANSI limit of 20 mJ/cm^2.
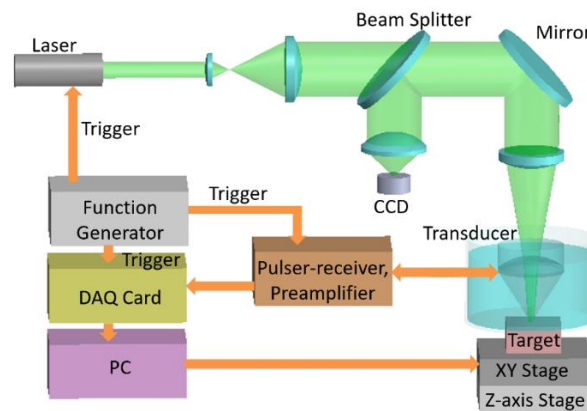
Fig. 6. 6. Schematic of the combined US and OA testing setup to characterize the OTF PVDF transducer. Reprinted with permission from [31] © Optica Publishing Group.

Fig. 6.7(a) shows the received and 39-dB amplified echo signal after the 2-μJ electrical pulse excitation and its frequency spectrum. The center frequency (f_c) and 3-dB bandwidth (BW) were determined to be 36-MHz and 44-MHz, respectively. The pulse-echo ultrasound axial resolution was quantified by the FWHM (full width at half maximum) of the signal envelope in the depth direction, which was calculated by the absolute Hilbert transformation (Fig. 6.7(b)). The axial resolution was determined to 17.7 μm, which is larger than the theoretical value of ~8.8 μm, possibly due to the non-

ideally equal phase of the ultrasound echo backscattered from the razor blade. To determine the acoustic focal spot and focal zone (depth of focus), the pulse-echo ultrasound testing was repeated by scanning the razor blade both horizontally with a 2-µm step and vertically with a 30-µm step around the nominal acoustic focal point. The FWHM value of the Gaussian-fitted amplitude profile was used to determine the corresponding acoustic beam diameter (Fig. 6.7(c)). The acoustic focal spot was characterized by the minimal FWHM, and the acoustic depth of focus was estimated by the height range where the on-axis peak amplitude dropped to half of its maximal value [64]. The acoustic focal spot size and focal depth of the OTF PVDF transducer were determined to be 37.8 μm and 210.0 μm, respectively. Fig. 6.7(d) shows the axial spread profile of the OA signal from the ink-coated razor blade and its envelope, indicating OA axial resolution around 39.1 μm. The optoacoustic testing was conducted to characterize the sensitivity of the OTF PVDF transducer. A needle hydrophone (Precision Acoustics, UK) with sensitivity or conversion factor (60 mV/MPa) served as the reference. The measured sensitivity of the OTF PVDF transducer was 3.06 µV/Pa, close to the 3 µV/Pa reported in [65]. The measured noise-equivalent-pressure (NEP) was 48.5 Pa, better than that (77 Pa) of commercial PZT-based (lead zirconate titanate) transducers [66].

(a)   (b)

(c)   (d)
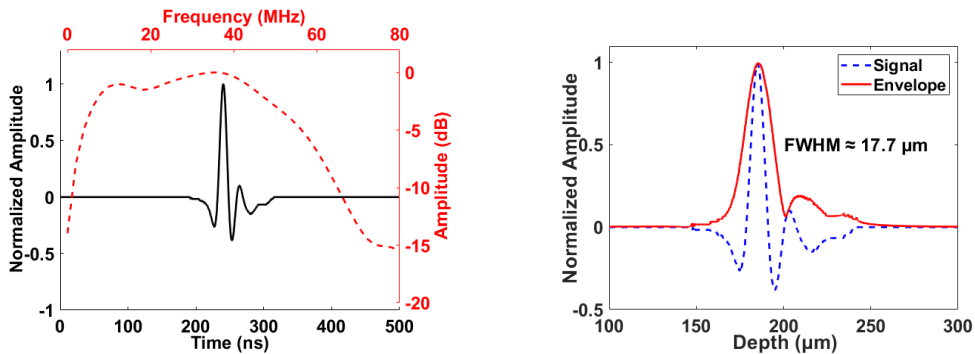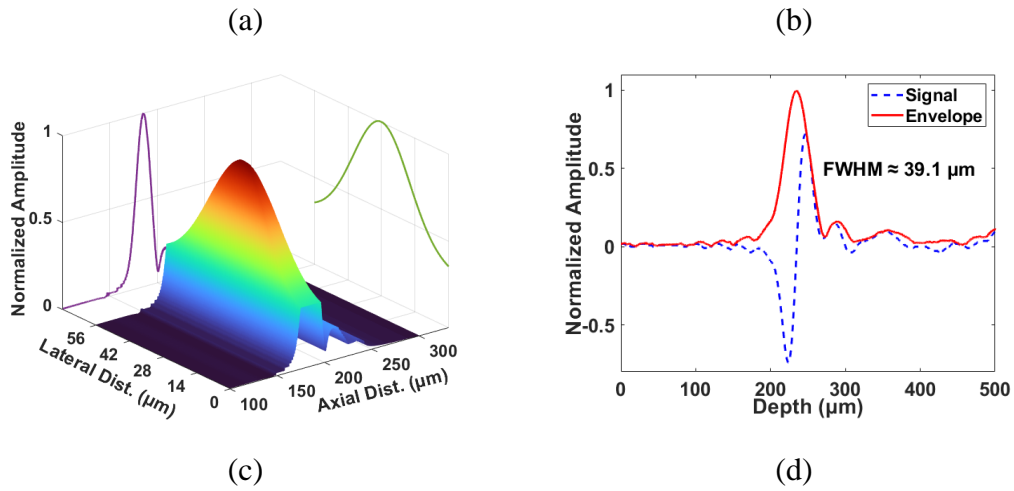
Fig. 6. 7. (a) A representative ultrasound echo signal (in solid black) and its frequency spectrum (in dashed red). (b) The axial spread profile of the ultrasound echo signal (in dashed blue) and its envelope (in solid red). (c) The measured axial and lateral ultrasound echo beam profiles, indicating the response at the axial-lateral cross-section. (d) The axial spread profile of the OA signal (in dashed blue) and its envelope (in solid red). Reprinted with permission from [31] © Optica Publishing Group.

6.4 OA Imaging and Results

6.4.1   Imaging Setup

The experimental setup (Fig. 6.6) was also used to demonstrate the OA imaging capability of the OTF PVDF transducer. The OTF PVDF transducer collected both OA and pulse-echo ultrasound signals from the target. The reconstructed ultrasound image served as a reference for evaluating the OA image. A pulser-receiver (Olympus NDT, USA) was synchronously triggered by the function generator to drive the transducer for sending ultrasound pulses to the target. One trigger from the function generator initiated

simultaneous OA and ultrasound data acquisition. The ultrasound and OA signals received by the transducer were amplified by the preamplifier embedded in the pulser-receiver and then recorded by a data-acquisition card (Alarzar Tech, Canada) (Fig. 6.8). It should be noted that the single triggering scheme will not cause the mixing of OA and ultrasound signals. Upon excitation, the ultrasound signal goes through a round trip (from the target to the transducer) and reaches the transducer, while the OA signal arrives after a single trip. The time delay of the ultrasound signal will be twice that of the OA signal (~6 µs) determined by the focal length (~9 mm) of the transducer and the acoustic velocity (~1500 m/s) in water. Because the difference in their time delay (~6 µs) is much longer than their durations (0.1~0.2 µs), both the OA and ultrasound signals are completely separated in time domain and therefore can be received without any mixing.
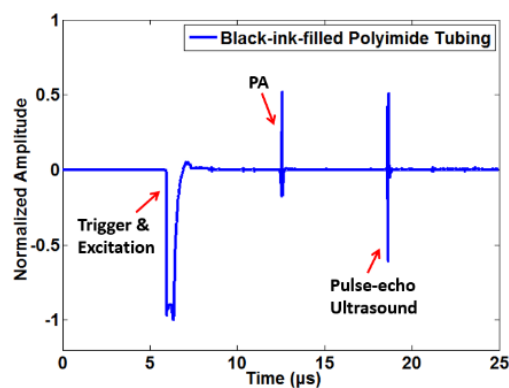
Fig. 6. 8. Representative waveform of received OA and pulse-echo ultrasound signals from a black-ink-filled polyimide tubing in water. Reprinted with permission from [31] © Optica Publishing Group.

A twisted metal wire with black plastic coating (total diameter $\phi \approx 0.5$ mm) was used as the imaging target, which was immersed in water and embedded inside chicken

breast tissue, respectively (Fig. 6.9). The depth of the wire ranged from 1 to 3 mm. A total area of 8×8 mm^2 (marked by the white dashed rectangle in Fig. 6.9) was scanned with a step size of 100 µm along the two orthogonal direction, and one scan takes around 0.5 hr. At each location, the data acquisition was repeated 40 times and the acquired OA & ultrasound signals were averaged to improve the signal-to-noise ratio (SNR). To improve the depth of view and reduce the imaging time, the OA and US data were acquired at five different depths (1.0, 1.5, 2.0, 2.5, and 3.0 mm), which covered the total depth range of the black wire within about 2.5 hrs.

(a)   (b)
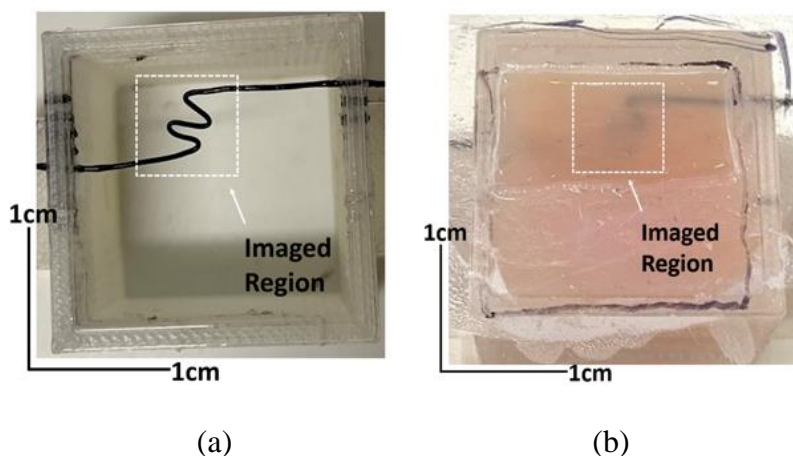
Fig. 6. 9. Photos of the black wire (top view) in (a) water, and (b) chicken breast tissue with the depth of 1 ~ 3 mm. The imaged regions are marked by the white dashed rectangles. Reprinted with permission from [31] © Optica Publishing Group.

6.4.2   Imaging Results

Fig. 6.10 shows the reconstructed 3D OA and US images of the black wire in water, which were merged from the data in focal zone at each scanning depth. The normalized signal amplitude of each pixel is indicated by the color bar. The contrast

ratio (CNR) of the OA and US images at the different scanning depth is 36 dB and 30 dB, respectively. The two CNRs remain almost constant, which is due to the weak optical & acoustic absorption and scattering of the water at a depth of a few mm. The slight variation of the CNR is mainly caused by the different tilting angles of the black wire section in the focal zone.
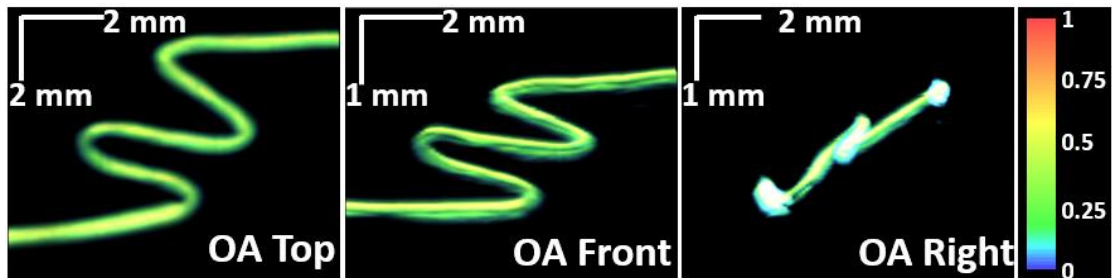
(a)
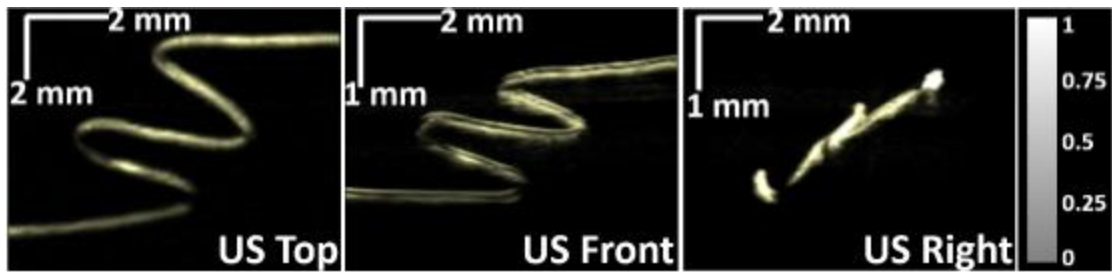
(b)

Fig. 6. 10. The reconstructed 3D (a) OA and (b) US images of the black wire in water from three different views. Reprinted with permission from [31] © Optica Publishing Group.

Fig. 6.11 shows the reconstructed 3D OA and US images of the black wire in chicken breast tissue. As shown in the OA images (Fig. 6.11(a)), the strength of the OA signals gradually drops at larger penetration depths due to increased optical absorption

and more importantly, the optical scattering in chicken breast tissue. The OA contrast ratio (CNR) decreases from 33.4 dB (when the top part is in focus) to 25.3 dB (when the bottom part is in focus). Nevertheless, the target at each scanning depth is resolved clearly, and the whole wire across the imaging depth could still be easily differentiated. In contrast, as shown in the US images, CNR remains around 20 dB at different imaging depths (Fig. 6.11(b)), which is lower than that in water. This can be explained by the low acoustic scattering but strong attenuation in the chicken breast tissue.
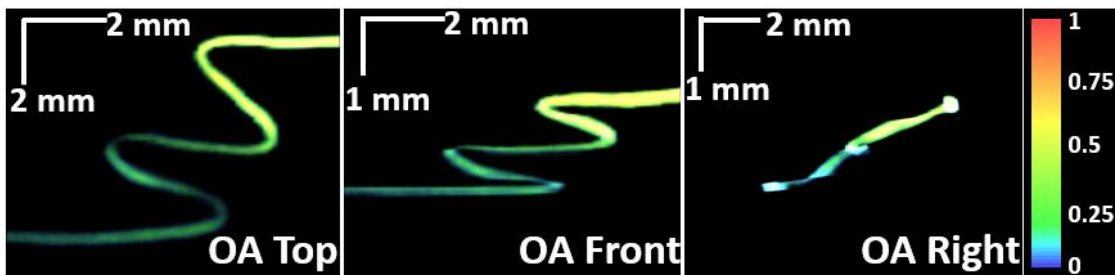
(a)
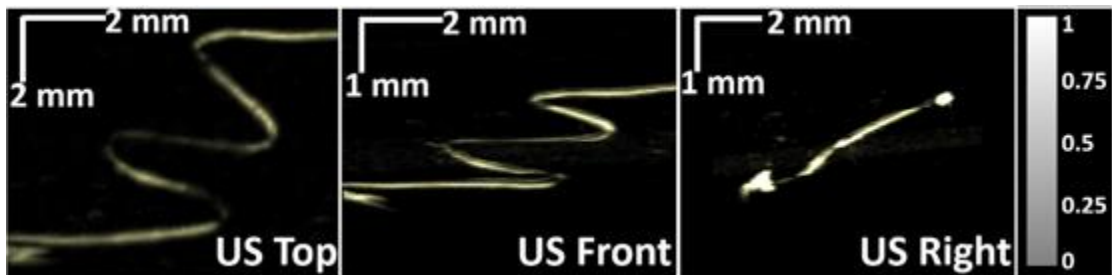
(b)

Fig. 6. 11. The reconstructed 3D (a) OA and (b) US images of the black wire in chicken breast tissue from three different views. A tiny air bubble appeared near the lower end of the wire in the US images, which is invisible in the OA images. The scale bar represents the normalized signal amplitude. Reprinted with permission from [31] © Optica Publishing Group.

For in-vivo imaging, a 4-mm-length cross section (B-scan) of a mouse tail (Fig. 6.12(a)) was imaged. The lab animal protocol for this work was approved by the University Laboratory Animal Care Committee of Texas A&M University. The tail hair was gently removed before the imaging. Sixteen scans with a lateral step size of 40 μm were repeated at the same cross section with 0.3-mm difference in depth, and the B-scan OA & US images were reconstructed by merging the data from the focal zone at each different depth. The OA image (Fig. 6.12(b), SNR ~ 28.9 dB) clearly shows the top skin & muscle as well as the dorsal & lateral veins of the mouse tail, while the skin surface pattern and inner structures of the mouse tail are revealed in the US image (Fig. 6.12(c), SNR ~ 26.8 dB). The combined OA and US image is shown in Fig. 6.12(d)).

(a)

(b)

<div align="center">(c)   (d)</div>
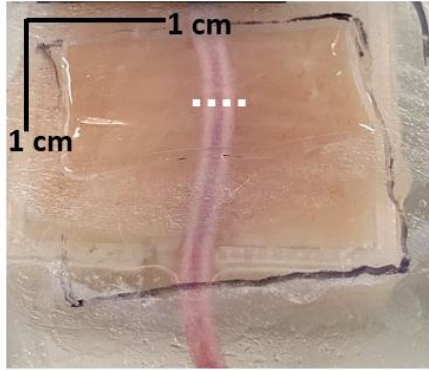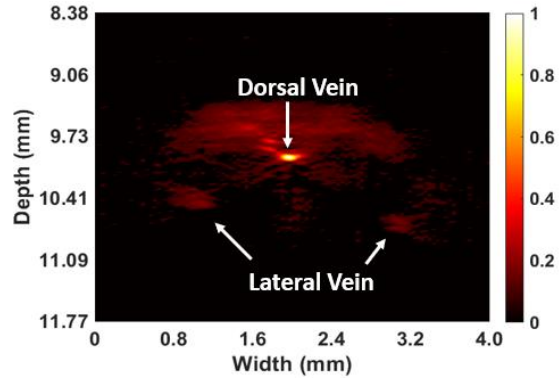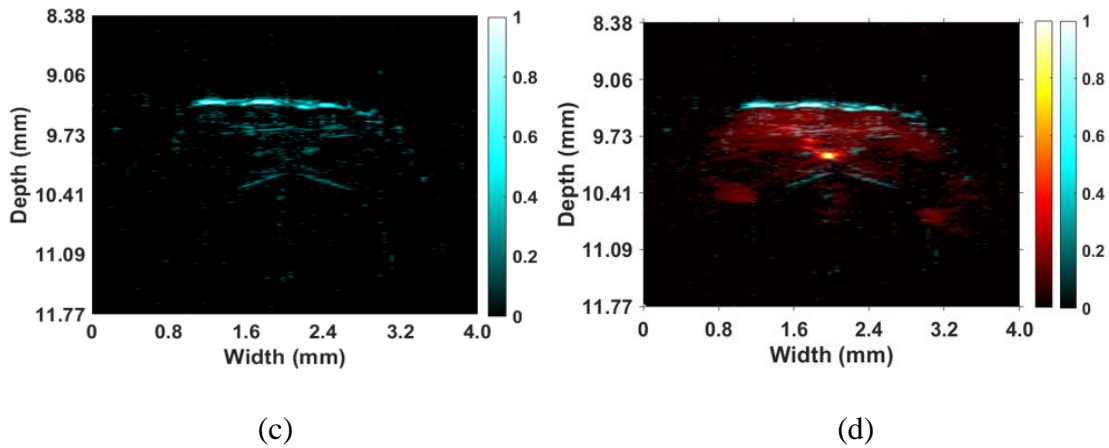
Fig. 6. 12. (a) The photo of the imaged mouse tail, where the imaged cross section is marked by the white dashed line. The reconstructed (b) OA, (c) US, and (d) combined B-scan images of the mouse tail. Reprinted with permission from [31] © Optica Publishing Group.

6.5 OTF P(VDF-TrFE) Transducer Design and Construction

Fig. 6.13 shows the schematic design of the new OTF P(VDF-TrFE) transducer. The 10-µm-thick P(VDF-TrFE) film (70/30 % mol, Piezotech, France) is pre-cut into a specific pattern and merged into a fitted spherical shape after directly laminating onto the curved surface of the concave glass lens (Edmund Optics, USA) with optical epoxy (Epotek 301, Epoxy Technology, USA). The concave glass lens has a diameter of 12.0 mm and spherical radius of 9.4 mm, corresponding to an acoustic focal length of 9.4 mm and numerical aperture (NA) of 0.64. The entire P(VDF-TrFE) film is coated with metal electrodes, except that a 2-mm-diameter window at the center is bare for the light to pass through. The P(VDF-TrFE) film at the window is kept for two main reasons. First, optical epoxy can be prevented from overflowing to bond the two lenses together, which

makes the convex lens releasing much easier. Second, with the P(VDF-TrFE) film left in the window, the entire P(VDF-TrFE) film becomes more robust to avoid tearing during the fabrication process.
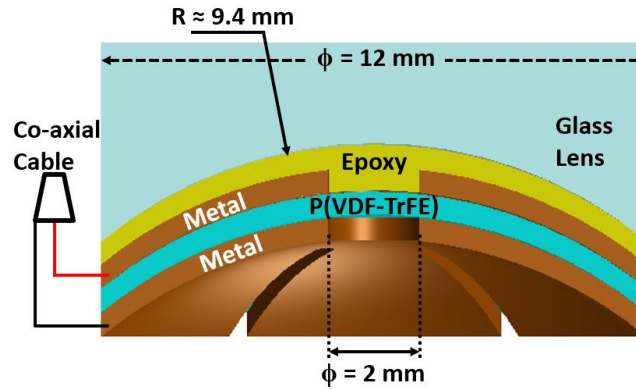
Fig. 6. 13. Schematic cross-section design of the OTF P(VDF-TrFE) transducer.

The specific fabrication flow of the new OTF P(VDF-TrFE) transducer is shown in Fig. 6.14. Firstly, the P(VDF-TrFE) film is trimmed into a specific pattern for fitting into a spherical surface by a mechanical cutter (Roland DGA, USA) (Fig. 6.14(a)). Secondly, with two shadow masks, chromium (15-nm thickness, 1 Å/s rate) and then copper (400-nm thickness, 2 Å/s rate) layers are e-beam evaporated onto both sides of the P(VDF-TrFE) film (Fig. 6.14(b)). The coverage area of the metal electrode around the pre-cut trenches is slightly smaller than the cut patterns to avoid electrical shorting of the two electrodes. ITO (indium-tin oxide) electrodes are not coated onto the central transparent window to maximize the optical transmittance and to further simplify the fabrication process. The transparent window has little influence on the vibration mode of P(VDF-TrFE) film (dominated by the thickness mode), because the film thickness (10 μm) is much smaller than its diameter (12 mm) and the film is firmly bonded onto the

concave lens so that other resonant modes are strongly damped. Its acoustic detection sensitivity is not significantly degraded because the transparent window is much smaller than the entire transducer. Thirdly, the metal-coated P(VDF-TrFE) film is merged into a spherical shape and bonded onto the concave surface of the glass lens (Fig. 6.14(c)) with optical epoxy (density $\rho = 1150$ kg/m^3, sound velocity c = 2650 m/s, acoustic impedance Z = 3.05 MRayls, Young's modulus Y = 5.8 GPa, and optical transmittance T > 99% @ 382-980 nm [67] [68] [69]). Lastly, the copper-coated tail of P(VDF-TrFE) film is flipped and both electrode tails are electroplated with 5-µm-thick Cu to facilitate the electrical connections with a coaxial cable. A piece of acrylic (1-mm thick) is attached to the glass lens to firmly support the electrodes of the transducer (Fig. 6.14(d)). A prototype of the fabricated OTF P(VDF-TrFE) transducer is shown in Fig. 6.15. The transducer is mounted onto a 3D-printed adapter for the installation onto a microscope objective lens during the testing.
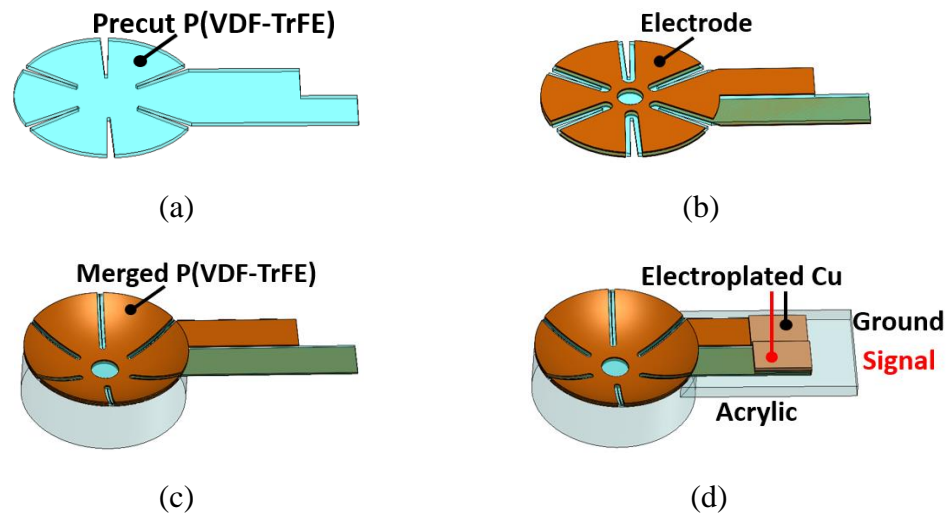
Fig. 6. 14. The fabrication process flow of the OTF P(VDF-TrFE) transducer: (a) P(VDF-TrFE) precut for fitting into a spherical surface; (b) Electrodes deposition on

88

both sides of P(VDF-TrFE); (c) P(VDF-TrFE) merged into a spherical shape and bonded onto the concave glass lens; (d) Long electrode tail flipping, Cu electroplating on both electrode tails for electrical connections, and acrylic attached for electrode support.

(a)   (b)
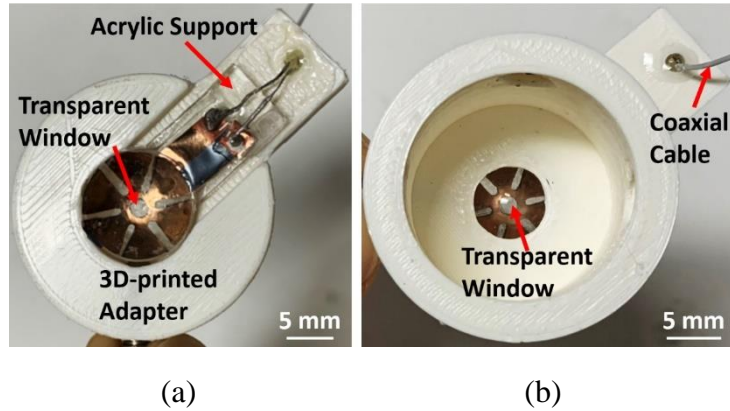
Fig. 6. 15. Photographs of the (a) front and (b) back side of the prototype OTF P(VDF-TrFE) transducer mounted on a 3D-printed adapter.

6.6 OTF P(VDF-TrFE) Transducer Testing and Characterization

A testing setup has been built for characterizing the optical, acoustic, and OA imaging performances of the OTF P(VDF-TrFE) transducer (Fig. 6.16). A function generator (Keysight Technologies, USA) triggers a Q-switched 532-nm Nd:YAG laser (Elforlight, UK) to generate nanosecond (< 1.8 ns) laser pulses at a pulse repetition rate (PRR) of 1 kHz. The pulsed laser beam is expanded by a pair of lenses (Thorlabs, USA) and filtered by a 50-μm pinhole (Thorlabs, USA) between them. The expanded laser beam is deflected by a fixed mirror and focused by a 10× optical objective lens (parfocal length = 45 mm, working distance = 6.56 mm) onto the target after passing through the OTF P(VDF-TrFE) transducer. The excitation region of the target is monitored by a

CCD camera in transmission mode. To achieve efficient acoustic coupling, the target and the front spherical surface of transducer are both submersed in water inside a petri dish. The petri dish is placed onto a transparent plate mounted on a XYZ stage, which consists of a computer-controlled X/Y motor stage (Physik Instrumente GmbH & Co. KG, Germany) and a manually-adjusted Z-axis stage (MPositioning, China). The signal received by the OTF P(VDF-TrFE) transducer is 39-dB amplified by a preamplifier embedded in the pulser-receiver (Olympus NDT, USA), and sampled by the oscilloscope (Tektronix Inc., USA) or data-acquisition (DAQ) card (Alarzar Tech, Canada), which is also triggered by the function generator.
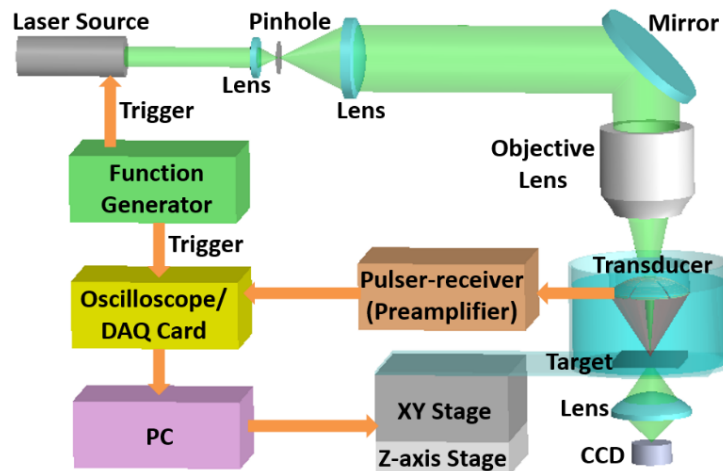
Fig. 6. 16. Experimental setup to characterize the optical, acoustic, and OA imaging performances of the OTF P(VDF-TrFE) transducer.

The optical transmittance of the OTF P(VDF-TrFE) transducer is characterized in air (with the target and petri dish removed). The average intensity of the laser pulses passing through the transducer is measured with an optical power meter (Thorlabs, USA).

The optical power passing through a bare concave glass lens is also measured to serve as the reference for determining the optical transmittance of the focused P(VDF-TrFE) transducer. Ultrasound pulse-echo testing is employed to characterize the acoustic properties of the OTF P(VDF-TrFE) transducer. A sharp razor blade in water is used as the target while pulsed laser is turned off. Driven by the pulser-receiver with a PRR of 200 Hz, acoustic pulses are transmitted from the focused P(VDF-TrFE) transducer and incident onto the sharp edge of the blade. The (echo) ultrasound signals scattered from the edge propagate along the inverse path and are detected by the focused P(VDF-TrFE) transducer, pre-amplified by the pulser receiver, and recorded by the oscilloscope. OAI on different targets is also conducted to investigate the OA imaging performance of the OTF P(VDF-TrFE) transducer, including lateral resolution, penetration depth and 2D mapping of more complex structures. The optical and acoustic foci are first aligned together by adjusting the installation of the transducer on the objective lens to maximize the acoustic detection sensitivity. During the imaging, the target is continuously moved by the X/Y stage, while the OA signals are collected by the DAQ card for image reconstruction.

The optical transmittance is calculated as the ratio of the average optical power after the OTF P(VDF-TrFE) transducer over that after a bare concave glass lens. Based on the measurement results, the optical transmittance of the OTF P(VDF-TrFE) transducer is determined to be 88.6% at 532-nm wavelength, which is significantly higher than that (~60%) of ITO-coated PVDF film [30] [31]. This is because the ITO coatings can increase the light reflection due to its high refractive index. The impact on

the laser focal spot from the transparent window of the focused P(VDF-TrFE) transducer is characterized with a calibration glass slide (AmScope, USA). After propagating through the objective lens and the OTF P(VDF-TrFE) transducer, the focal spot of the laser beam is measured to be around 6.5 µm in diameter (Fig. 6.17). For comparison, the diameter of the laser spot is around 6.0 µm after replacing the transducer with a bare concave glass lens. Therefore, the OTF P(VDF-TrFE) transducer causes little distortion to the propagation of laser pulses to excite OA signals.
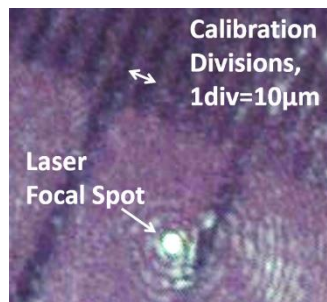
Fig. 6. 17. Laser focal spot size measurement with a calibration glass slide.

Fig. 6.18 shows the electrical impedance and phase angle spectra of the focused P(VDF-TrFE) transducer, which is measured by an electrical impedance spectroscopy (Sciospec Scientific Instruments GmbH, Germany). Based on the curve, the transducer resonant frequency (f_c) and electromechanical coupling factor (k_{33}) are estimated around 22 MHz and 0.27, respectively. Fig. 6.19 shows a representative ultrasound echo signal (solid black) and its frequency spectrum (dashed red) after Fast Fourier Transformation (FFT), which indicates a central frequency (f_c) and bandwidth (BW) of 24 MHz (close to that estimated from the electrical impedance curve) and 29 MHz, respectively. The measured f_c and BW of the focused P(VDF-TrFE) transducer are somewhat lower than

those of the previous molded PVDF transducer (f_c ~ 36 MHz and BW ~ 44 MHz) [31] (Table 6. 3), which is possibly due to the larger thickness of P(VDF-TrFE) film and also the epoxy layer used for bonding. In addition, the slightly reduced NA (caused by the uncoated transparent window at the center) and less perfect spherical shape of the merged P(VDF-TrFE) film may slightly deteriorate the synchronization of the ultrasound wavefront, which can also contribute to the lower f_c and BW. Based on the measured f_c, BW, and nominal acoustic NA (e.g., 0.64), the acoustic focal spot size, axial resolution, and depth of focus (DOF) of the OTF P(VDF-TrFE) transducer are estimated to be 122.9 μm, 13.3 μm, and 118.6 μm, respectively. The sensitivity of the P(VDF-TrFE) transducer is characterized by a needle hydrophone (Precision Acoustics, UK) with known sensitivity of 53 nV/Pa. The measured sensitivity of the P(VDF-TrFE) transducer is 6.84 μV/Pa, which is almost six times of that (1.19 μV/Pa) of the previous low-NA PVDF transducer [30]. Fig. 6.20 shows a representative OA signal (solid black) from a black tape layer as the target and its frequency spectrum (dashed red) after FFT excited by the 100-nJ laser pulse. The frequency spectrum indicates both the f_c and BW of the OA signal are around 10 MHz. The f_c is much lower than that (~24 MHz) of the pulse-echo ultrasound signal, which is mainly due to the soft black tape and relatively weak laser intensity, while the wide fractional BW (~100%) is typical for the OA signals from a soft target such as black tape. The performances of OTF PVDF and P(VDF-TrFE) transducers are roughly compared as Table 6.3.
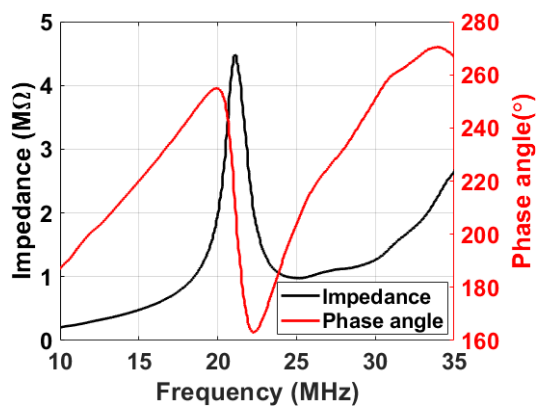
Fig. 6. 18. Measured electrical impedance (black line) and phase angle (red line) spectra of the OTF P(VDF-TrFE) transducer, indicating the resonance frequency around 22 MHz and electromechanical coupling factor (k_{33}) around 0.27.
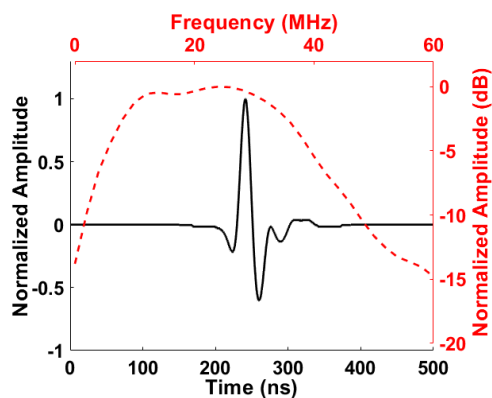
Fig. 6. 19. A representative echo ultrasound signal (in solid black) and its frequency spectrum (in dashed red) of the OTF P(VDF-TrFE) transducer.
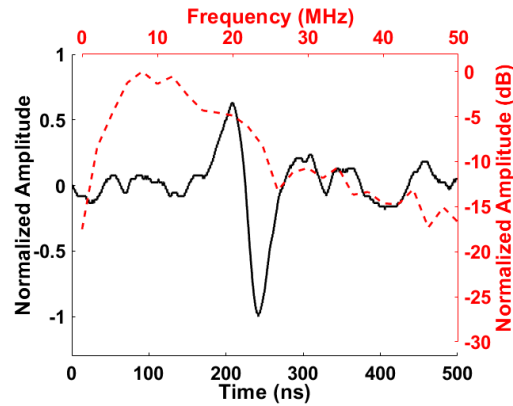
Fig. 6. 20. A representative OA signal (in solid black) from a black tape target and its frequency spectrum (in dashed red).

Table 6. 3. Comparison of the performance of the OTF PVDF and P(VDF-TrFE) transducers.

Transducer	OTF PVDF	OTF P(VDF-TrFE)
Center Frequency (f_c)	36 MHz	24 MHz
Bandwidth (BW)	44 MHz	29 MHz
Detection Sensitivity	3.06 µV/Pa	6.84 µV/Pa

6.7 OA Imaging and Results

6.7.1 Imaging Setup

For the OAI setup (Fig. 6.16) with the OTF P(VDF-TrFE) transducer, the target is continuously scanned in a straight line to characterize the lateral resolution and penetration depth, while the target is zigzag moved by the program-controlled XY stage

for 2D mapping. The time-domain (A-line) signals are acquired by the DAQ card with 250-MHz sample frequency. Then the raw A-line signals are processed by digital filters for noise reduction and Hilbert transformation for waveform unipolarization. The B-mode OA images are reconstructed by displaying the processed A-line signals in one line, and the OA amplitude profile and 2D mapping are projected by the maximum amplitude of the processed A-line signal at each location.

6.7.2 Imaging Results

The lateral resolution of the OAI setup with the OTF P(VDF-TrFE) transducer is characterized by scanning a square chromium pattern on a USAF (United States Air Force) resolution target (Thorlabs, USA). The OA amplitude profile across the edge of the chromium pattern is fitted by the edge spread function (ESF) to calculate the corresponding line spread function (LSF), which is the derivative of the ESF. The lateral resolution is indicated by the full width at half maximum (FWHM) of the corresponding LSF. As shown in Fig. 6.21(a), the OA lateral resolution is estimated as 6.6 μm, which is close to the measured laser spot size (Fig. 6.17). For verification, five groups of No. 6 line patterns on the USAF resolution target are also scanned (along the white dashed line in Fig. 6.21(b)). They can be clearly resolved based on the corresponding cross-sectional OA profile (Fig. 6.21(b)). The smallest group of line patterns has a spatial frequency of 114 line-pairs/mm (corresponding to an FWHM of 8.78 μm). This result verifies the 6.6-μm OA lateral resolution determined by the LSF of the edge of single chromium pattern.

(a)	(b)
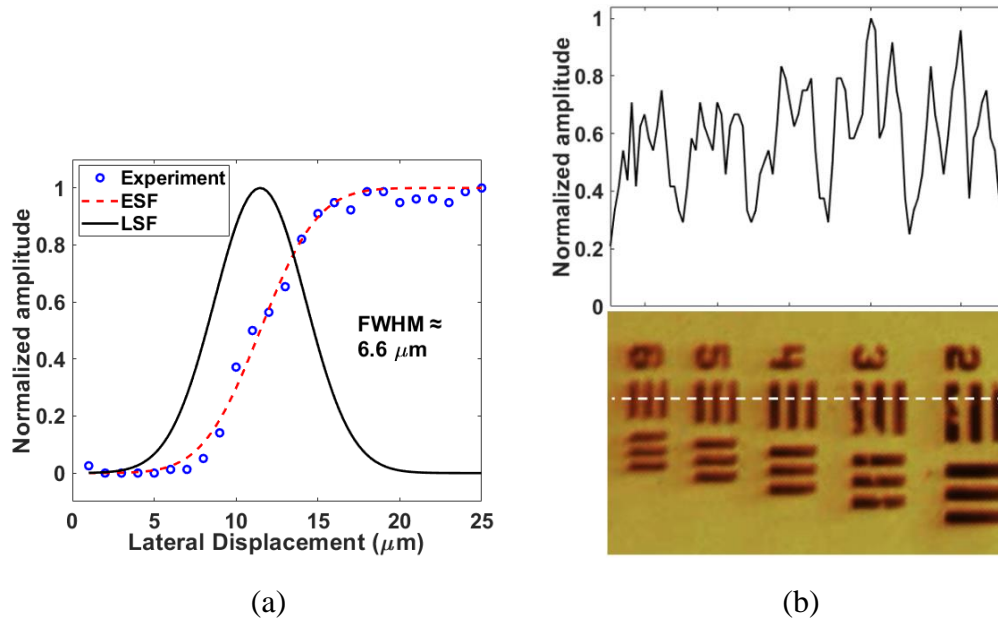
Fig. 6. 21. The FWHM of the LSF derived from the fitted ESF, indicating the OA lateral resolution around 6.6 µm. (b) The cross-sectional OA profile of the corresponding five groups of No. 6 elements on a resolution target (scanning path indicated by the white-dashed line). Reprinted with permission from [32] © SPIE.

The penetration depth of the OAI setup with the OTF P(VDF-TrFE) transducer is characterized with a 100-µm-diameter polyimide tubing filled with black ink as the target. Two optically scattering media are tested, including 1% agar (Sigma-Aldrich, USA) phantom and chicken breast tissue. The ink-filled tubing is inserted into the agar phantom and chicken breast tissue at an oblique angle. The OA excitation energy is set to be 200 nJ per pulse. The OAI setup is scanned along the ink-filled tubing for reconstructing a B-mode OA image to show the insertion of the tubing. As shown in Fig. 6.22(a), the OAI setup can clearly image the tubing down to around 2.1 mm beneath the

97

surface. In the chicken breast tissue, the OAI setup can clearly image the tubing down to around 0.5 mm beneath the surface (Fig. 6.22(b)). This shallower depth is mainly due to the stronger optical absorption and scattering in chicken breast tissue than the agar phantom. Some artifacts exist at lateral displacement around 0 – 1 mm (Fig. 6.22(b)), which is mainly due to the acoustic reflection inside the glass lens.

(a)   (b)
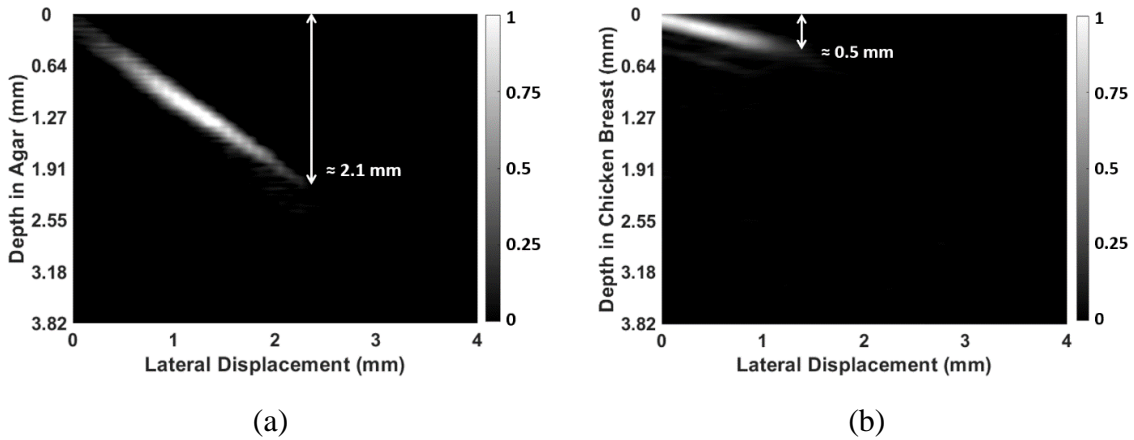
Fig. 6. 22. B-mode OA images of a 100-µm-diameter polyimide tubing filled with black ink obliquely inserted in (a) 1% agar phantom and (b) chicken breast tissue.

The two-dimensional (2D) OA imaging capability with the OTF P(VDF-TrFE) transducer is also explored. A black leaf skeleton with both course (hundreds of µm) and fine branches (several ~ tens of µm) is laminated on a glass substrate as the imaging target (Fig. 6.23(a)). The OA scanning is conducted within an 8 mm × 4 mm area and the scanning step size is 8 µm in both directions, which is close to the size of the optical focal spot. The OA excitation energy is set to be 200 nJ per pulse. At each scan point, the OA excitation and reception are repeated 16 times. The captured OA signals are averaged to improve the signal-to-noise ratio (SNR) up to 17.0 dB. The 2D OA image

(Fig. 6.23(b)) is reconstructed based on the signal amplitude at each location, which determines the grayscale value of each pixel. Most of the branches are clearly resolved except the finest ones. Further increasing the excitation pulse energy helps to reveal the finer branches, which however could increase the chance of structural damage. Due to the weaker signal strength at the edges of the branches, the width of the branches in the OA image appears somewhat smaller than that in the optical micrograph. There are some variations in the signal strength across the reconstructed OA image, which is caused by the topographic variations of different leaf skeleton branches.

(a)
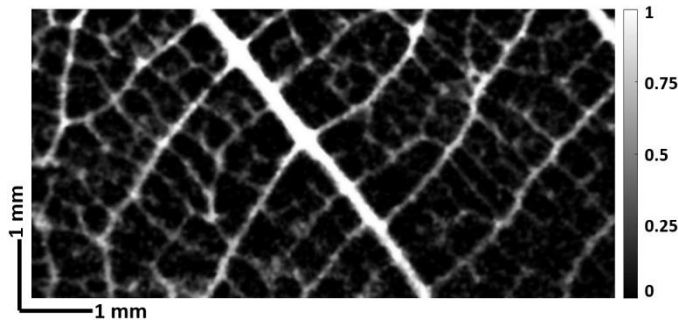
(b)

Fig. 6. 23. (a) The optical photograph and (b) the 2D OA image of the black leaf skeleton phantom with an area of 8 mm × 4 mm.

The *in-vivo* OAI with the OTF P(VDF-TrFE) transducer is demonstrated by imaging the mouse belly veins (Fig. 6.24(a)) with 1.0-1.4 mm depth beneath the skin. The lab animal protocol for this work was approved by the University Laboratory Animal Care Committee of Texas A&M University. The mouse belly hair is gently removed before the imaging. The OAI setup is slightly different from that in Fig. 6. 16, where the petri dish is above the mouse. The bottom of the petri dish is opened with a square hole and covered by plastic wrap film (thickness ~ 10 μm) to pass the light and OA signals with little attenuation. Ultrasound gel is pasted between the plastic wrap and mouse belly to improve the coupling and remove air bubbles. The OA scanning (500 nJ/pulse) is conducted across an 8 mm × 8 mm area with a 20-μm scanning step in both directions. As the pulsed laser is focused at 1.2 mm beneath the skin, the surface light fluence is estimated around 0.88 mJ/cm^2, which is far below the ANSI safety limit (20 mJ/cm^2). 40 scans are repeated at each point to improve the signal-to-noise ratio (SNR) up to 12.3 dB. The OA image (Fig. 6.24(b)) shows the veins in the mouse belly. Similarly, some variation in the signal strength is caused by the topographic non-uniformity of the mouse skin and the various vein depths beneath the skin.

(a)   (b)
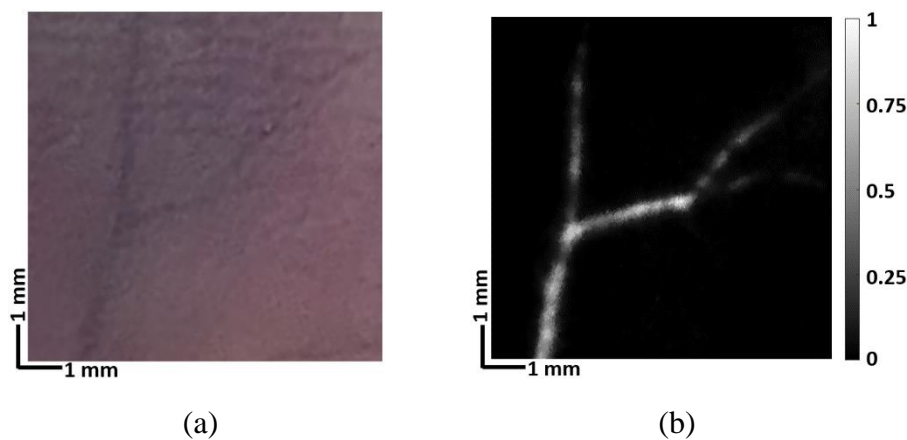
Fig. 6. 24. (a) The optical photograph and (b) the 2D OA image of the blood vessels in mouse belly with an area of 8 mm × 8 mm.

6.8 Summary

In summary, the OTF PVDF and P(VDF-TrFE) transducers for OAI have been successfully demonstrated. With the adequate optical transmittance, wide acoustic bandwidth, and low acoustic impedance, the two OTF transducers can provide small acoustic focal spots without light blockage, thereby are helpful to enable a miniaturized DMDSM sensor with improved resolution and sensitivity.

7. CONCLUSIONS AND FUTURE WORK

As a conclusion, the DMDSM near-distance sensors for robotic ranging and material/structure differentiation have been successfully demonstrated. Compared with existing sensors, the DMDSM sensors provide optimal solutions by combining the US and OA modalities to deal with conventional objects as well as OACTs with good lateral resolutions. Besides, based on the configuration simplification of G2 sensor and the performance improvement of G3 sensor, the DMDSM sensors provide not only a practical and powerful perception solution, but also new and better pretouch mapping and imaging capabilities to assist robotic grasping of unknown objects. Moreover, the development of OTF transducers can be useful for further miniaturization of the DMDSM sensor while enhancing their performances.

In the future, first, the DMDSM sensors will be further miniaturized while improving their performances. Second, a new multi-wavelength pulsed light source with high PRR will be explored to expand the varieties of OA-detectable targets, boost up the scanning speed, and reduce the imaging time. Third, quick mapping and imaging capabilities will be developed to make the DMDSM sensors more practical to be mounted on a robotic hand for real grasping operations.

REFERENCES

[1]   M. T. Mason, Mechanics of Robotic Manipulation, MIT press, 2001.

[2]   M. Ciocarlie, K. Hsiao, E.G. Jones, S. Chitta, R.B. Rusu and I.A. Şucan, "Towards reliable grasping and manipulation in household environments," *Experimental Robotics,* pp. 241-252, Springer, Berlin, Heidelberg, 2014.

[3]   K. Y. Goldberg, "Orienting Polygonal Parts Without Sensors," *Algorithmica,* vol. 10, no. 2-4, pp. 201-225, 1993.

[4]   M. A. Erdmann and M. T. Mason, "An exploration of sensorless manipulation," *IEEE Journal on Robotics and Automation,* vol. 4, no. 4, pp. 369-379, 1988.

[5]   R. D. Howe, "Tactile sensing and control of robotic manipulation," *Advanced Robotics,* vol. 8, no. 3, pp. 245-261, 1993.

[6]   J. M. Romano, K. Hsiao, G. Niemeyer, S. Chitta and K. J. Kuchenbecker, "Human-Inspired Robotic Grasp Control With Tactile Sensing," *IEEE Transactions on Robotics,* vol. 27, no. 6, pp. 1067-1079, 2011.

[7]   Q. Xu, "Design and Development of a Novel Compliant Gripper With Integrated Position and Grasping/Interaction Force Sensing," *IEEE Transactions on Automation Science and Engineering,* vol. 14, no. 3, pp. 1415 - 1428, 2015.

[8]   C. E. Smith and N. P. Papanikolopoulos, "Vision-guided robotic grasping: Issues and experiments," *In Proceedings of IEEE International Conference on Robotics and Automation,* vol. 4, pp. 3203-3208, 1996.

[9]   A. Wehr and U. Lohr, "Airborne laser scanning—an introduction and overview," *ISPRS Journal of photogrammetry and remote sensing,* vol. 54, no. 2-3, pp. 68-82, 1999.

[10] Y. Lu, J. Lee, S.-H. Yeh, H.-M. Cheng, B. Chen and D. Song, "Sharing Heterogeneous Spatial Knowledge: Map Fusion between Asynchronous Monocular Vision and Lidar or Other Prior Inputs," in *International Symposium on Robotics Research (ISRR)*, Puerto Varas, Chile,, 2017.

[11] M.-C. Amann, T. M. Bosch, M. Lescure, R. A. Myllylae and M. Rioux, "Laser ranging: a critical review of unusual techniques for distance measurement," *Optical engineering,* vol. 40, no. 1, pp. 10-20, 2001.

[12] A. Stelzer, M. Jahn and S. Scheiblhofer, "Precise distance measurement with cooperative FMCW radar units," *In 2008 IEEE Radio and Wireless Symposium,* pp. 771-774, 2008.

[13] J. R. Smith, E. Garcia, R. Wistort and G. Krishnamoorthy, "Electric field imaging pretouch for robotic graspers," *2007 IEEE/RSJ International Conference on Intelligent Robots and Systems,* pp. 676-683, 2007.

[14] R. Wistort and J. R. Smith, "Electric field servoing for robotic manipulation," *In 2008 IEEE/RSJ International Conference on Intelligent Robots and Systems,* pp. 494-499, 2008, September.

[15] B. Mayton, L. LeGrand and J. R. Smith, "An electric field pretouch system for grasping and co-manipulation," *2010 IEEE International Conference on Robotics*

and Automation, pp. 831-838, 2010.

[16] B. Mayton, E. Garcia, L. LeGrand and J. R. Smith, "Electric field pretouch: Towards mobile manipulation," *In RSS Workshop on Mobile Manipulation in Human Environments,* 2009, June.

[17] K. Hsiao, P. Nangeroni, M. Huber, A. Saxena and A. Y. Ng, "Reactive grasping using optical proximity sensors," *2009 IEEE International Conference on Robotics and Automation,* pp. 2098-2105, 2009.

[18] B. Yang, P. Lancaster and J. R. Smith, "Pre-touch sensing for sequential manipulation," *In 2017 IEEE International Conference on Robotics and Automation (ICRA),* pp. 5088-5095, 2017.

[19] H. Hasegawa, Y. Mizoguchi, K. Tadakuma, A. Ming, M. Ishikawa and M. Shimojo, "Development of intelligent robot hand using proximity, contact and slip sensing," *In 2010 IEEE International Conference on Robotics and Automation,* pp. 777-784, 2010, May.

[20] A. Maldonado, H. Alvarez and M. Beetz, "Improving robot manipulation through fingertip perception," *In 2012 IEEE/RSJ International Conference on Intelligent Robots and Systems,* pp. 2947-2954, 2012.

[21] L. Jiang and J. R. Smith, "A unified framework for grasping and shape acquisition via pretouch sensing," *In 2013 IEEE International Conference on Robotics and Automation,* pp. 999-1005, 2013, May.

[22] E. Guglielmelli, V. Genovese, P. Dario and G. Morana, "Avoiding obstacles by

using a proximity us/ir sensitive skin," *In Proceedings of 1993 IEEE/RSJ International Conference on Intelligent Robots and Systems (IROS'93),* vol. 3, pp. 2207-2214, 1993, July.

[23] L. Jiang and J. R. Smith, "Seashell effect pretouch sensing for robotic grasping," *In 2012 IEEE International Conference on Robotics and Automation,* pp. 2851-2858, 2012, May.

[24] L. T. Jiang and J. R. Smith, "Pretouch sensing for manipulation," *In Robotics: Science and Systems (RSS) Workshop: Alternative Sensing Techniques for Robotic Perception,* 2012, July.

[25] C. Fang, D. Wang, D. Song and J. Zou, "Fingertip Pulse-Echo Ultrasound and Optoacoustic Dual-Modal and Dual Sensing Mechanisms Near-Distance Sensor for Ranging and Material Sensing in Robotic Grasping," *IEEE International Conference on Robotics and Automation (ICRA),* pp. 14105-14111, 2021.

[26] C. Fang, D. Wang, D. Song and J. Zou, "Fingertip Non-Contact Optoacoustic Sensor for Near-Distance Ranging and Thickness Differentiation for Robotic Grasping," *2020 IEEE International Conference on Robotics and Automation (Accepted),* 2020.

[27] C. Fang, D. Wang, D. Song and J. Zou, "Toward Fingertip Non-Contact Material Recognition and Near-Distance Ranging for Robotic Grasping," *2019 IEEE International Conference on Robotics and Automation (ICRA),* pp. 4967-4974, 2019.

[28] C. Fang, D. Wang, D. Song and J. Zou, "The Second Generation (G2) Fingertip Sensor for Near-Distance Ranging and Material Sensing in Robotic Grasping," *In IEEE 2022 International Conference on Robotics and Automation (ICRA),* pp. 1506-1512, 2022, May.

[29] D. Wang, F. Guo, C. Fang, J. Zou and D. Song, "Design of an Object Scanning System and a Calibration Method for a Fingertip-Mounted Dual-Modal and Dual Sensing Mechanisms (DMDSM)-based Pretouch Sensor for Grasping," *In 2022 IEEE 18th International Conference on Automation Science and Engineering (CASE),* pp. 341-347, 2022, August.

[30] C. Fang, H. Hu and J. Zou, "A focused optically transparent PVDF transducer for photoacoustic microscopy," *IEEE Sensors Journal,* vol. 20, no. 5, pp. 2313-2319, 2019.

[31] C. Fang and J. Zou, "Acoustic Resolution Photoacoustic Microscopy (AR-PAM) Based on an Optically Transparent Focused Transducer with a High Numerical Aperture," *Optics Letters,* vol. 46, no. 13, pp. 3280-3283, 2021.

[32] C. Fang, Z. Zhao, J. Fang and J. Zou, "An Optically-Transparent Focused P(VDF-TrFE) Transducer for Photoacoustic Microscopy (PAM) ," *In Photons Plus Ultrasound: Imaging and Sensing 2023,* vol. 12379, pp. 300-306, SPIE, 2023.

[33] R. D. Howe, "Tactile sensing and control of robotic manipulation," *Advanced Robotics,* vol. 8, no. 3, pp. 245-261, 1993.

[34] J. M. Romano, K. Hsiao, G. Niemeyer, S. Chitta and J. K. Kuchenbecker, "Human-

Inspired Robotic Grasp Control With Tactile Sensing," *IEEE Transactions on Robotics,* vol. 27, no. 6, pp. 1067-1079, 2011.

[35] Y. Lu, J. Lee, S. H. Yeh, H. M. Cheng, B. Chen and D. Song, "Sharing Heterogeneous Spatial Knowledge: Map Fusion between Asynchronous Monocular Vision and Lidar or Other Prior Inputs," *Robotics Research,* pp. 727-741, Springer, Cham, 2020.

[36] M. C. Amann, T. M. Bosch , M. Lescure, R. A. Myllylae and M. Rioux, "Laser ranging: a critical review of unusual techniques for distance measurement," *Optical engineering ,* vol. 40, pp. 10-19, 2001.

[37] Y. Wang, G. L. Zhang, H. Lang, B. Zuo and C. W. De Silva, "A modified image-based visual servo controller with hybrid camera configuration for robust robotic grasping," *Robotics and Autonomous Systems,* vol. 62, no. 10, pp. 1398-1407, 2014.

[38] B. Yamauchi, "All-weather perception for man-portable robots using ultra-wideband radar," *In 2010 IEEE International Conference on Robotics and Automation,* pp. 3610-3615, 2010 May.

[39] M. Vossiek, L. Wiebking, P. Gulden, J. Wieghardt, C. Hoffmann and P. Heide, "Wireless local positioning," *IEEE microwave magazine,* vol. 4, no. 4, pp. 77-86, 2003.

[40] L. T. Jiang and J. R. Smith, "Seashell effect pretouch sensing for robotic grasping," *In 2012 IEEE International Conference on Robotics and Automation,* pp. 2851-2858, 2012, May.

[41] I. P. Dunn and W. A. Davern, "Calculation of acoustic impedance of multi-layer absorbers," *Applied acoustics,* vol. 19, no. 5, pp. 321-334, 1986.

[42] M. E. Delany and E. N. Bazley, "Acoustical Properties of Fibrous Absorbent Materials," *Applied acoustics= Acoustique appliqu = Angewandte Akustik,* vol. 3, no. 2, pp. 105-116, 1970.

[43] M. I. Khan and G. J. Diebold, "The photoacoustic effect generated by laser irradiation of an isotropic solid cylinder," *Ultrasonics,* vol. 34, no. 1, pp. 19-24, 1996.

[44] R. D. Mindlin and H. Deresiewicz, "Thickness-shear and flexural vibrations of a circular disk," *Journal of applied physics,* vol. 25, no. 10, pp. 1329-1332, 1954.

[45] P. Schäfer, "The BOSS is concerned with time series classification in the presence of noise," *Data Mining and Knowledge Discovery,* vol. 29, no. 6, pp. 1505-1530, 2015.

[46] A. Bagnall, J. Lines, A. Bostrom, J. Large and E. Keogh, "The great time series classification bake off: a review and experimental evaluation of recent algorithmic advances," *Data Mining and Knowledge Discovery,* vol. 31, no. 3, pp. 606-660, 2017.

[47] X. Duan, D. Wang, D. Song and J. Zou, "Device Design and System Integration of a Two-Axis Water-immersible Micro Scanning Mirror (WIMSM) to Enable Dual-modal Optical and Acoustic Communication and Ranging for Underwater Vehicles," *IEEE International Conference on Robotics and Automation (ICRA),* pp.

13114-13119, 2021, May.

[48] L. Li, C. Yeh, S. Hu, L. Wang, B.T. Soetikno, R. Chen, Q. Zhou, K.K. Shung, K.I. Maslov and L.V. Wang, "Fully motorized optical-resolution photoacoustic microscopy," *Optics letters,* vol. 39, no. 7, pp. 2117-2120, 2014.

[49] K. Maslov, G. Stoica and L. V. Wang, "In vivo dark-field reflection-mode photoacoustic microscopy," *Optics letters,* vol. 30, no. 6, pp. 625-627, 2005.

[50] L. Wang, K. I. Maslov, W. Xing, A. Garcia-Uribe and L. V. Wang, "Video-rate functional photoacoustic microscopy at depths," *Journal of biomedical optics,* vol. 17, no. 10, p. 106007, 2012.

[51] S. Park, S. Kang and J. H. Chang, "Optically transparent focused transducers for combined photoacoustic and ultrasound microscopy," *Journal of Medical and Biological Engineering,* vol. 40, pp. 707-718, 2020.

[52] J. Park, B. Park, T. Y. Kim, S. Jung, W. J. Choi, J. Ahn , D.H. Yoon, J. Kim, S. Jeon, D. Lee, U. Yong and C. Kim, "Quadruple ultrasound, photoacoustic, optical coherence, and fluorescence fusion imaging with a transparent ultrasound transducer," *Proceedings of the National Academy of Sciences,* vol. 118, no. 11, 2021.

[53] Y. Y. Choi, T. G. Yun, N. Qaiser, H. Paik, H.S. Roh, J. Hong, S. Hong, S. M. Han and K. No, "Vertically aligned P (VDF-TrFE) core-shell structures on flexible pillar arrays," *Scientific Reports,* vol. 5, no. 1, p. 10728, 2015.

[54] A. Vinogradov and F. Holloway, "Electro-mechanical properties of the

piezoelectric polymer PVDF," *Ferroelectrics,* vol. 226, no. 1, pp. 169-181, 1999.

[55] H. Ohigashi, K. Koga, M. Suzuki, T. Nakanishi, K. Kimura and N. Hashimoto, "Piezoelectric and ferroelectric properties of P (VDF-TrFE) copolymers and their application to ultrasonic transducers," *Ferroelectrics,* vol. 60, no. 1, pp. 263-276, 1984.

[56] F. S. Foster, K. A. Harasiewicz and M. D. Sherar, "A history of medical and biological imaging with polyvinylidene fluoride (PVDF) transducers," *IEEE transactions on ultrasonics, ferroelectrics, and frequency control,* vol. 47, no. 6, pp. 1363-1371, 2000.

[57] Z. Y. Cheng, H. Xu, T. X. Mai, T. M. Chung, Q. M. Zhang and R. Y. Ting, "P (VDF-TrFE)-based electrostrictive co/ter-polymers and their device performance," *In Smart structures and materials 2001: electroactive polymer actuators and devices,* vol. 4329, pp. 106-116, SPIE, 2001.

[58] W. H. Liew, M. S. Mirshekarloo, S. Chen, K. Yao and F. E. H. Tay, "Nanoconfinement induced crystal orientation and large piezoelectric coefficient in vertically aligned P (VDF-TrFE) nanotube array," *Scientific Reports,* vol. 5, no. 1, pp. 1-7, 2015.

[59] K. K. Shung, J. M. Cannata and Q. F. Zhou, "Piezoelectric materials for high frequency medical imaging applications: A review," *Journal of Electroceramics,* vol. 19, pp. 141-147, 2007.

[60] H. L. Chan, Z. Zhao, K. W. Kwok, C. L. Choy, C. Alquié, C. Boué and J. Lewiner,

"Polarization of thick polyvinylidene fluoride/trifluoroethylene copolymer films," *Journal of applied physics,* vol. 80, no. 7, pp. 3982-3991, 1996.

[61] [Online]. Available:

https://www.thorlabs.com/newgrouppage9.cfm?objectgroup_id=2087&pn=LC1054 #2089.

[62] [Online]. Available: https://www.norlandprod.com/literature/81tds.pdf.

[63] C. Fang and J. Zou , "An optically-transparent transducer with a high-NA and wide-bandwidth for photoacoustic microscopy (PAM)," *In Photons Plus Ultrasound: Imaging and Sensing SPIE 2021,* vol. 11642, pp. 135-141, 2021.

[64] [Online]. Available: https://mbi-ctac.sites.medinfo.ufl.edu/files/2017/02/ultrasound-basics.pdf.

[65] A. M. Winkler, K. I. Maslov and L. V. Wang, "Noise-equivalent sensitivity of photoacoustics," *Journal of biomedical optics,* vol. 18, no. 9, p. 097003, 2013.

[66] J. Yao and L. V. Wang, "Sensitivity of photoacoustic microscopy," *Photoacoustics,* vol. 2, no. 87-101, p. 2, 2014.

[67] J. Yu and A. Kidane, "Acoustic properties of composites containing multiple heterogeneities: micromechanics modelling," *International Journal of Theoretical and Applied Multiscale Mechanics,* vol. 2, no. 4, pp. 271-286, 2013.

[68] M. Osman, K. Creamer, H. Chen, J. Minotto, J. Liu, S. Agrawal and S. R. Kothapalli, "A novel translucent ultrasound transducer approach for dual-modality ultrasound and photoacosutic imaging," *In Photons Plus Ultrasound: Imaging and*

Sensing SPIE 2022, vol. 11960, pp. 331-337, 2022.

[69] Epoxy Technology, Inc., "Epotek 301 Technical Data Sheet," Epoxy Technology,

[Online]. Available: https://www.epotek.com/docs/en/Datasheet/301.pdf.